Semi-Analytical Uncertainty Propagation and Conjunction Assessment

by

Yashica Khatri

B.S., Aerospace Engineering, Embry-Riddle Aeronautical University, 2018

M.S., Aerospace Engineering Sciences - Astrodynamics and Satellite Navigation, University of Colorado Boulder, 2020

A thesis submitted to the

Faculty of the Graduate School of the

University of Colorado in partial fulfillment

of the requirements for the degree of

Doctor of Philosophy

Department of Aerospace Engineering

2023

Committee Members:

Daniel J. Scheeres, Chair

Nisar Ahmed

K. Terry Alfriend

Marcus Holzinger

Jay McMahon

Khatri, Yashica (Ph.D., Aerospace Engineering Sciences - Astrodynamics and Satellite Navigation)

Semi-Analytical Uncertainty Propagation and Conjunction Assessment

Thesis directed by Dr. Daniel J. Scheeres

With an increase in space traffic in near-Earth and cislunar regimes, it is important to concentrate new research on development of accurate and efficient Space Situational Awareness (SSA) tools. One of the most significant discussions in SSA today is in accurate state uncertainty representation and propagation, with a direct application in understanding conjunction possibilities. Several analytical and semi-analytical methods have been developed that aim to efficiently achieve an accurate capture of this uncertainty over long periods of time to achieve realistic future locations without recurrent observations so as to alleviate the stress on observation resources.

This study presents a new method of nonlinear uncertainty propagation that combines several existing and complex mathematical tools to capture the non-Gaussian evolution of the distribution. An initial distribution is split into a Gaussian Mixture Model (GMM) to map the distribution piece-wise. This mapping is performed using higher order State Transition Tensors (STTs) that have the ability to capture higher order perturbations of the system dynamics. The STTs used to map the GMM components are calculated using complex dynamical systems that allow realism in the uncertainty propagation. For near-Earth applications, this is achieved using a Simplified Dynamical System (SDS) that incorporates perturbations from J_2 dynamics and Solar Radiation Pressure (SRP). In cislunar space, the Circular Restricted Three-Body Problem (CR3BP) is used in combination with these STTs to achieve the GMM component mapping. The combined mapped GMM components result in a final non-Gaussian distribution.

The GMM-STT uncertainty mapping is combined with analytical conjunction formulas to achieve a system collision probability. The cumulative probability of collision is achieved by combining collision probabilities associated with a GMM component-by-component comparison for the objects in conjunction. The final collision probability is compared to that from a Monte Carlo

analysis to confirm validity. The new methods of uncertainty propagation and conjunction assessment presented in this dissertation provide fast, accurate, and realistic results for short and long duration conjunctions in near-Earth and cislunar domains.

Dedication

To my mom and dad, thank you for your never ending love and support.

Acknowledgements

This has been a journey of a lifetime. First and foremost, I would like to thank my advisor Dr. Daniel Scheeres for his guidance throughout this academic journey. I am truly grateful to have you as a mentor and I will forever be thankful to have had this opportunity to explore this research with you as a guiding light. I would like to thank all my committee members, Dr. Nisar Ahmed, Dr. Terry Alfriend, Dr. Marcus Holzinger, and Dr. Jay McMahon for their invaluable feedback that significantly enriched the depth and quality of this research.

The last few years have challenged me in more ways than I can count. To all my current and past CSML labmates, thank you for the numerous thoughtful discussions and lots of fun times. To my dearest friends - Gavin, Jayce, Kristen, Bruce, Nina, and so many others - thank you for your unwavering support during the highs and (many) lows, belief in my abilities, and unconditional love. I love having you in my life. To my mother and father, I would not be who I am today without you. You have supported me all my life, taught me to be strong, have independent thought, and pursue all my dreams, without ever considering that my dreams will send me so far away from you. A big thanks to my brother, Droan, who I have had endless conversations with on everything in life including our shared love for space. To Komal masi and Sudhir mosaji who have been like second parents to me since I moved to the US, thank you for always being there for me. And lastly, to my loving fiance, Shubham, thank you for always believing in me and being my touchstone to reality. I can't wait to marry you. Thank you to all my family and friends for being an integral part of my life.

Contents

Chapter

1 Introduction **1**

1.1 Challenges in Space Situational Awareness in Near-Earth and Cislunar Regimes . . . 1

1.2 Review of Literature . . . 2

1.3 Research Contributions . . . 4

1.4 Chapter Organization . . . 7

2 Mapping of Nonlinear System Dynamics **10**

2.1 Near-Earth Regime . . . 11

2.1.1 Two-Body Problem . . . 11

2.1.2 2BP + J_2 Secular Dynamics . . . 12

2.1.3 Simplified Dynamical System . . . 12

2.2 Cislunar Regime: The Circular Restricted Three-Body Problem . . . 24

2.3 State Transition Tensors . . . 26

2.3.1 Mathematical Formulation . . . 26

2.3.2 Nonlinear Mapping of Moments with State Transition Tensors . . . 28

2.3.3 State Transition Tensors for Near-Earth and Cislunar Regions . . . 29

2.4 Conclusion . . . 31

3 Semi-Analytical Propagation of Uncertainty **32**

3.1 Gaussian Mixture Models . . . 33

3.2 Gaussian Mixture Model Splitting Methods . . . 34
3.2.1 Near-Earth Region . . . 34
3.2.2 Cislunar Region . . . 37
3.3 Combining Gaussian Mixture Models and State Transition Tensors . . . 40
3.4 Uncertainty Propagation using Gaussian Mixture Models and State Transition Tensors 42
3.4.1 Near-Earth Case . . . 42
3.4.2 Cislunar Case . . . 44
3.5 Conclusion . . . 48

4 Probability of Collision **49**
4.1 Uncertainty Propagation in Conjunction Analysis . . . 50
4.2 Conjunction Models . . . 51
4.2.1 Short-Term Conjunctions . . . 51
4.2.2 Long-Term Conjunctions . . . 53
4.3 Monte Carlo Method . . . 54
4.3.1 Test Case for Monte Carlo with the Simplified Dynamical System . . . 56
4.4 The Hybrid Method of Uncertainty Propagation and Conjunction Analysis . . . 57
4.4.1 Coppola's Conjunction Analysis Formula . . . 59
4.4.2 Combining General Conjunction Formula with GMMs . . . 61
4.4.3 New Approach to Improve Speed . . . 63
4.5 Conclusion . . . 65

5 Conjunction Assessment Test Cases **67**
5.1 Near-Earth Region . . . 68
5.1.1 Two-Body Dynamics Test Case . . . 68
5.1.2 2BP Repeating Conjunction Study . . . 69
5.1.3 2BP + J_2 Secular Dynamics Test Case . . . 72
5.1.4 Simplified Dynamical System Test Case . . . 73

5.2 Cislunar Region 80
5.2.1 Lyapunov Orbit Test Case 80
5.2.2 Halo Orbit Test Case 82
5.2.3 NRHO Test Case 86
5.3 Discussion 89

6 Near-Earth GitHub-Accessible Toolkits **90**
6.1 Semi-Analytical Uncertainty Propagation and Probability of Collision Calculation Implementation 91
6.1.1 Gaussian Mixture Model Splitting 92
6.1.2 Simplified Dynamical System 93
6.1.3 State Transition Tensors 93
6.1.4 Time of Closest Approach Finder 94
6.1.5 Probability of Collision Calculations 95
6.2 Monte Carlo Method 96
6.3 Code Initialization 97
6.4 Test Case 99
6.4.1 Example Setup 99
6.4.2 Results 101
6.5 Conclusion 101

7 Conclusions and Future Work **103**
7.1 Conclusions 103
7.2 Future Work 105

Bibliography **107**

Appendix

A Transformations of State and Uncertainty Coordinates **113**

B Simplified Dynamical System: Mean Dynamics Equations **116**

Tables

Table

2.1 Orbital Elements at epoch for the SDS propagation example. 23

3.1 Orbital Elements at epoch for the near-Earth GMM-STT propagation test. 42

3.2 Univariate split library for near-Earth test case. 43

3.3 State at epoch for cislunar GMM-STT propagation test. 44

3.4 Univariate split library for cislunar test case. 45

3.5 Directions and nonlinear parameter values from Eq. (3.7). 45

4.1 Orbital Elements for the SDS Monte Carlo example. 56

4.2 Probability of collision for the Monte Carlo method with different dynamics. 57

5.1 Orbital Elements for the 2BP example. 68

5.2 Orbital Elements for the Repeating Conjunctions example. 70

5.3 Orbital Elements for the J_2 Secular example. 72

5.4 Orbital Elements for the SDS example. [50] 74

5.5 Runtimes of different methods. [50] 76

5.6 Orbital Elements for the example. 76

5.7 Runtimes of different methods. [50] 79

5.8 Orbital Elements for the first test case. Object 1 is in an L1 Lyapunov orbit. 80

5.9 Time comparison of the semi-analytical uncertainty propagation method vs the Monte Carlo method for probability of collision computation. 82

5.10 Orbital Elements for the first test case. Object 1 is in an L1 Halo orbit. 82

5.11 Orbital Elements for the second Halo test case. Object 1 is in an L1 Halo orbit. . . . 85

5.12 Orbital Elements for the NRHO test case. Object 1 is in an L2 NRHO orbit. 86

A.1 Caption 114

Figures

Figure

2.1 The secular, short-period, and long-period variations in the evolution of an orbital element. [77] 13

2.2 The initial osculating state is converted to the mean state for propagation with the SDS. At the final time, the final mean state is converted back to an osculating state to get an accurate final state. [50] 23

2.3 A comparison of Delaunay elements propagated with full dynamics (blue solid line) vs SDS (pink dashed line) with short-period variations added at the last orbit. . . . 24

2.4 The difference between the Delaunay elements propagated with full dynamics vs SDS with short-period variations added at the last orbit. 24

2.5 Earth, Moon, and a third body in the CR3BP rotating frame. 25

3.1 These figures show the initial and final distributions constituting the GMM components. 34

3.2 The distribution of weights relative to the means of GMM components. [49] 35

3.3 Propagation of uncertainty using the GMM-STT method. [49] 40

3.4 The final $\delta \boldsymbol{m}_f$ added to the nominal final state gives the final averaged GMM component mean. To improve accuracy, this final SDS mean state is converted to its corresponding osculating state to get the final GMM component mean [50]. 41

3.5 GMM-STT propagated example. Here, the 1000 yellow dots represent the MC propagated points, the black plus symbols represent the propagated GMM component means and the blue ellipses represent the propagated component covariances. 43

3.6 GMM-STT propagated example in cislunar space using the lowest ϕ or the smallest nonlinearity growth direction mapped with the non-nominal STTs. Here, the 500 yellow dots represent the MC propagated points, the black plus symbols represent the propagated GMM component means and the blue ellipses represent the propagated component covariances. 46

3.7 GMM-STT propagated example in cislunar space using the highest ϕ or the largest nonlinearity growth direction mapped with the non-nominal STTs. Here, the 500 yellow dots represent the MC propagated points, the black plus symbols represent the propagated GMM component means and the blue ellipses represent the propagated component covariances. 47

3.8 GMM-STT propagated example in cislunar space using the highest ϕ or the largest nonlinearity growth direction mapped with the nominal STTs. Here, the 500 yellow dots represent the MC propagated points, the black plus symbols represent the propagated GMM component means and the blue ellipses represent the propagated component covariances. 47

4.1 Uncertainty overlap at a future time. The initially Gaussian uncertainty distributions loose their Gaussianity when propagated using nonlinear dynamics. A conjunction can occur when there is an overlap in object uncertainties. [50] 50

4.2 Short-term conjunction example. (a): The blue ellipse is the trajectory of object 1, whereas the yellow is the trajectory of object 2. The black point is the initial location of object 1, and the red is the initial location of object 2. The violet star is the nominal conjunction point of the two objects. (b): Relative distance between the two objects over 3 days. 52

4.3 Long-term conjunction example. (a): Orbits, initial locations, and nominal conjunction points of the two objects. The blue ellipse is the trajectory of object 1, whereas the yellow is the trajectory of object 2. The black point is the initial location of object 1, and the red is the initial location of object 2. The violet star is the nominal conjunction point of the two objects. The black stars show the beginning and end of the conjunction. (b): Relative distance between the two objects over 3 days. Red dashed line represents an arbitrary line of the distance below which the objects are considered to be in a conjunction. 53

4.4 In the Monte Carlo method, (from left to right) points from initial distribution of each object are propagated to the final time, where their distance of closest approach informs the collision probability in a one-on-one analysis. 55

4.5 Uncertainty propagation and conjunction assessment toolkit process summary. . . . 59

4.6 The total probability of collision in the GMM-STT method is an all-on-all analysis between propagated GMM components of objects 1 (blue) and 2 (yellow). $P_{c,ij}$ is a comparison between i^{th} and j^{th} GMM components from objects 1 and 2 respectively. The highlighted GMM components are the ones being compared for the probability of collision calculations.[50] 65

5.1 Subfig. (a) Orbits and initial locations of the two objects in the 2BP example. The blue ellipse is the trajectory of object 1, whereas the yellow is the trajectory of object 2. The black point is the initial location of object 1 and the red is the initial location of object 2. Subfig. (b) Uncertainty distribution of the two objects in the 2BP example at their nominal TCA. The blue and yellow points represent the Monte Carlo propagated points from the initial uncertainties of objects 1 and 2 respectively. 68

5.2 Subfig. (a) shows the GMM-STT collision probability vs Monte Carlo results for the 2BP example, whereas Subfig. (b) shows the relative error in the GMM-STT results wrt the Monte Carlo ones. The solid blue line represents the Monte Carlo probability of collision, the dashed blue lines represent the 95% confidence bounds, and the yellow diamonds represent the GMM-STT probability of collisions at different number of GMM mixture components. 69

5.3 Orbits and initial locations of the two objects in the Repeating Conjunction example. The blue ellipse is the trajectory of object 1, whereas the yellow is the trajectory of object 2. The black point is the initial location of object 1 and the red is the initial location of object 2. 70

5.4 Subfig. (a), (b), and (c) show the uncertainty distribution in the Repeating Conjunction example. The blue and yellow points represent the Monte Carlo propagated points from the initial uncertainties of objects 1 and 2 respectively.

Subfig. (d), (e), and (f) show the GMM-STT collision probability vs Monte Carlo probability for the Repeating Conjunction example. The solid blue line represents the Monte Carlo probability of collision, the dashed blue lines represent the 95% confidence bounds, and the yellow diamonds represent the GMM-STT probability of collisions at different numbers of Gaussian mixture components. 71

5.5 Subfig. (a) Orbits and initial locations of the two objects in the J_2 Secular example. The blue ellipse is the trajectory of object 1, whereas the yellow is the trajectory of object 2. The black point is the initial location of object 1 and the red is the initial location of object 2. Subfig. (b) Uncertainty distribution of the two objects in the J_2 Secular example at the nominal TCA. The blue and yellow points represent the Monte Carlo propagated points from the initial uncertainties of objects 1 and 2, respectively. 73

5.6 Subfig. (a) shows the GMM-STT collision probability vs Monte Carlo probability for the J_2 Secular example, whereas Subfig. (b) shows the relative error between the two. The solid blue line represents the Monte Carlo probability of collision, the dashed blue lines represent the 95% confidence bounds, and the yellow diamonds represent the GMM-STT probability of collisions at different number of GMM mixture components. 73

5.7 (a): Orbits, epoch locations, and the conjunction point of the two objects. Object 1 trajectory is represented in blue and object 2 trajectory is represented in yellow. The black point denotes the initial location of object 1, and the red point denotes that of object 2. The purple star is the conjunction point of the two objects. (b): Uncertainty distribution of the two objects. The blue and yellow points represent the Monte Carlo propagated points of objects 1 and 2 respectively. [50] 75

5.8 Subfig. (a) shows the GMM-STT results and the SDS Monte Carlo results vs the full dynamics Monte Carlo probability of collision, whereas Subfig. (b) shows the relative error in the GMM-STT probability of collision wrt the full dynamics Monte Carlo probability of collision. The solid blue line shows the full dynamics Monte Carlo probability of collision, the dashed blue lines represent the 95% confidence bounds, the red dashed line represents the SDS Monte Carlo probability of collision, and the pink diamonds represent the GMM-STT probability of collisions at different numbers of GMM mixture components each. [50] 76

5.9 (a): The blue ellipse and yellow ellipses are the trajectories of objects 1 and 2, respectively. The black and red points are the initial locations of object 1 and 2, respectively. The purple star is the nominal conjunction point of the two objects. The black stars show the beginning and end of the conjunction period. (b): The blue line represents the relative orbit. The purple star is the conjunction point of the two objects. The black stars show the duration of the conjunction period. (c) The blue line shows the relative distance between objects and the red dashed line shows an arbitrary threshold below which distance the objects are considered to be in a conjunction. (d) The blue and yellow points represent the Monte Carlo propagated points associated with objects 1 and 2, respectively, at the nominal TCA. 78

5.10 High uncertainty case: (a) and (b): The solid blue line represents the SDS dynamics Monte Carlo probability of collision, the dashed blue lines represent the 95% confidence bounds, and the pink diamonds represent the semi-analytical probability of collisions at different numbers of GMM mixture components. 79

5.11 Low uncertainty case: (a) and (b): The solid blue line represents the SDS dynamics Monte Carlo probability of collision, the dashed blue lines represent the 95% confidence bounds, and the pink diamonds represent the semi-analytical probability of collisions at different numbers of GMM mixture components. 79

5.12 Lyapunov test case: (a) and (b) show the trajectories on the two objects in conjunction in 2D and 3D views, respectively. The blue orbit is the Lyapunov orbit and the yellow trajectory represents the second object in conjunction. (c) shows the propagated uncertainty of the two objects at the nominal TCA. 81

5.13 Lyapunov test case: These plots show the comparison of the probability of collision from the semi-analytical method developed in this paper to the Monte Carlo probability of collision. The solid blue line shows the Monte Carlo probability of collision, the dashed blue lines show the 99% error threshold, and the pink diamonds show the probability of collision computed using the semi-analytical uncertainty propagation. 82

5.14 Halo test case 1: (a) and (b) show the trajectories on the two objects in conjunction in 2D and 3D views, respectively. The blue and yellow trajectories refer to the Halo orbit and the secondary object orbit, respectively. (c) shows the propagated uncertainty of the two objects at the nominal TCA. 83

5.15 Halo test case 1: These plots show the comparison of the probability of collision from the semi-analytical method developed in this paper to the Monte Carlo probability of collision. The solid blue line shows the Monte Carlo probability of collision, the dashed blue lines show the 99% error threshold, and the pink diamonds show the probability of collision computed using the semi-analytical uncertainty propagation. 84

5.16 Halo test case 2: (a) and (b) show the trajectories on the two objects in conjunction in 2D and 3D views, respectively. The blue and yellow trajectories refer to the Halo orbit and the secondary object orbit, respectively. (c) shows the propagated uncertainty of the two objects at the nominal TCA. 85

5.17 Halo test case 2: These plots show the comparison of the probability of collision from the semi-analytical method developed in this paper to the Monte Carlo probability of collision. The solid blue line shows the Monte Carlo probability of collision, the dashed blue lines show the 95% error threshold, and the pink diamonds show the probability of collision computed using the semi-analytical uncertainty propagation. 86

5.18 NRHO test case: (a) and (b) show the trajectories on the two objects in conjunction in 2D and 3D views, respectively. The blue and yellow trajectories refer to the NRHO orbit and the secondary object orbit, respectively. (c) shows the propagated uncertainty of the two objects at the nominal TCA. 87

5.19 NRHO test case with "bad" GMM splitting: These plots show the comparison of the probability of collision from the semi-analytical method developed in this paper to the Monte Carlo probability of collision. The solid blue line shows the Monte Carlo probability of collision, the dashed blue lines show the 95% error threshold, and the pink diamonds show the probability of collision computed using the semi-analytical uncertainty propagation. 88

5.20 NRHO test case with "good" GMM splitting: These plots show the comparison of the probability of collision from the semi-analytical method developed in this paper to the Monte Carlo probability of collision. The solid blue line shows the Monte Carlo probability of collision, the dashed blue lines show the 95% error threshold, and the pink diamonds show the probability of collision computed using the semi-analytical uncertainty propagation. 89

6.1 A summary of the semi-analytical uncertainty propagation and conjunction analysis method. [51] 91

6.2 The initial GMM component mean is a deviation from the nominal mean state. This GMM mean is mapped to the final time using STTs and it is converted back to the osculating state. [51] 95

6.3 Each GMM component from object 1 is compared to that from object 2 to compute the cumulative probability of collision. [50] 96

6.4 The initial state is converted to a mean state and is mapped to the final time using STTs, where it is converted back to the osculating state. [51] 97

6.5 (a) Blue and yellow trajectories show the nominal trajectories of objects 1 and 2, respectively. The black dot and red dot denote the initial locations of objects 1 and 2, respectively. Purple star denotes the conjunction point. (b) The blue points and yellow points show the uncertainty distributions at the nominal TCA of objects 1 and 2, respectively. 99

6.6 (a) The solid blue line refers to the Monte Carlo probability of collision and the dashed blue lines are the confidence intervals around this result. The pink diamonds show the semi-analytical approach probability of collision at different number of GMM components. (b) The dashed line shows the binomial normal approximation 95% confidence interval line. The pink diamonds show the semi-analytical approach results for the probability of collision. 101

Chapter 1

Introduction

1.1 Challenges in Space Situational Awareness in Near-Earth and Cislunar Regimes

The journey from Sputnik I's launch to the hundreds of thousands of man-made objects currently in space has been one of an exponential rate [72]. As a result, the near-Earth space region has become increasingly crowded leading to a higher risk of collisions. Such collisions can lead to hurdles in mission success, or even fragmentation [59], adding to a vicious cycle of debris growth [57]. In addition to this congestion in near-Earth space, the cislunar domain is of increasing interest in new space missions [33]. Space objects larger than 10 cm in diameter are tracked routinely by the Space Surveillance Network, whereas smaller objects are generally detected by ground-based radars, as needed. Such observation resources are limited in capacity leading to intermittent observations of tracked objects. This is excessively prohibitive in cislunar space because of an additional lack of the Global Positioning System (GPS) [63]. This means that in both, near-Earth and cislunar regions, specific objects are not constantly monitored resulting in limited current state and associated uncertainty information. This limited information requires gap-bridging of the data or long-term consistent predictions of future locations of such objects. The nonlinear nature of the space environment makes such long-term predictions of the state and uncertainty of these objects nontrivial. This prediction of state and uncertainty is one of the most significant technical discussions in Space Situational Awareness (SSA) [39, 28, 43, 64, 34, 35] today.

Uncertainty distributions lose their traditional Gaussian nature when propagated with dy-

namics that exhibit nonlinear behaviour. Many linearized mapping methods, like State Transition Matrices (STM) [70], assume a Gaussian nature and evolution of the distribution, which is inconsistent with the real world evolution with highly nonlinear space dynamics [44]. It is essential to capture this nonlinear behaviour in a computationally efficient manner with the increasing need for the development of accurate SSA tools. A major application of accurate and efficient uncertainty representation and evolution is in conjunction analysis to avoid the involuntary growth of space objects in the form of debris and to protect mission safety.

1.2 Review of Literature

Traditionally, computationally expensive numerical Monte Carlo methods have been used to nonlinearly propagate a large ensemble of sample points. With enough sample points, these methods can be used to estimate probability moments. Alternative options to such expensive methods aim to reduce the number of sample points needed for the accurate capture of the nonlinear evolution of the distribution. Many analytical and semi-analytical mathematical representations and expressions of nonlinear uncertainty and its propagation have been presented in the SSA domain, such as Gaussian sums using Gaussian Mixture Models (GMMs) [74, 39, 79, 78], higher order Taylor series solutions using State Transition Tensors (STTs) [66, 73, 8, 30], Polynomial Chaos Expansions (PCEs) [42, 43], and methods that use a combination of these techniques [81, 34]. Such analytical and semi-analytical methods aim to reduce computational cost by minimizing the points in the propagation and providing efficient propagation methods while maintaining statistical accuracy.

Using GMMs, a judicious selection of grouped distributions can be used to minimise cost [74]. Work by Terejanu et al. [74] adopts the GMM splitting to propagate the system probability density function (PDF) to capture nonlinear behaviour. Horwood et al. [39] introduces multi-directional splitting methods and a combination of GMMs with filtering approaches. Sorenson and Alspach [6, 71] introduced a GMM approach to the Bayesian estimation problem that allows distribution modelling using a GMM sum. Vittaldev and Russell [79] extends multi-directional splitting in non-Gaussian uncertainty propagation. Work by DeMars et al. [24] introduce adaptive methods

of GMM splits in uncertainty propagation. A similar approach is also applied to object tracking in space in DeMars et al. [27].

STTs provide accurate and efficient moment mapping through a higher order capture of advanced dynamical models. Park [66] introduced a method to use STTs for nonlinear mapping of statistics. Elgohary and Turner [30] presents an analytical continuation to encompass Earth oblateness effects in STT computations. Younes [8] extends this model to higher orders of the STT. Park and Scheeres [65] illustrates a direct moment mapping using STTs combined with an advanced dynamical system. PCEs allow a representation of the uncertainty using orthogonal polynomials [42, 81]. Several combinations of these models have also been studied, such as GMMs and PCEs [81]; and GMMs and STTs [34].

Several analytical [13, 53, 38] and semi-analytical [16, 23, 31, 62, 55, 7] solutions have been previously developed to describe the motion of orbiting objects about a central body that take into account additional perturbations such as Earth oblateness, Solar Radiation Pressure (SRP), gravitational attraction due to additional bodies, and atmospheric drag. Park and Scheeres [65] introduces such a semi-analytical method that goes one step further from the classical analytical theory to achieve a combination of speed and accuracy in propagation using the Lie transformation method defined by Deprit [29] to get separate representations of the secular, long-period, and short-period variations from the perturbed dynamics. The Simplified Dynamical System (SDS) introduced by Park and Scheeres reduces the nonlinearity of the dynamical system by eliminating short-period variations in propagation, allowing efficiency in propagation.

Similar to the uncertainty evolution methods, the field of conjunction analysis generally uses simple Monte Carlo methods [4] in collision probability computations. Point clouds from the objects in conjunction are propagated to their times of closest approach to achieve the probability associated with two objects colliding. Such methods are the most reliable and accurate with enough sample points, leading to a concerning computation cost when the number of the sample points increases. Several previous publications have introduced alternate analytical and semi-analytical collision probability methods. These methods include those from Foster [32], Chan [19, 18, 17],

DeMars [25, 26], Vittaldev [80], Brown [15], Coppola [21, 22], Jones [42], and many others. Many of these assume a Gaussian distribution for uncertainty at the time of conjunction leading to restrictive applications, whereas others combine methods such as GMMs [26] and PCEs [42] with conjunction analysis methods. It is essential to understand the assumptions associated with each of these methods to understand their applications.

Short and long duration conjunctions have been of interest in near-Earth space for a long time due to the increased congestion caused by space objects [72]. In recent times, cislunar SSA is also gaining importance due to a growing number of space missions in that region. Some recent research in this emerging field has indicated a need for new and accurate SSA tools in uncertainty propagation and conjunction analysis. Frueh et al. [33] presents the challenges in cislunar SSA and draws parallels to known issues in the near-Earth realm.

1.3 Research Contributions

The work in this dissertation focuses on developing analytical and semi-analytical accurate and efficient models of uncertainty propagation in the near-Earth and cislunar realm, along with their applications in conjunction assessment. The primary contributions of this dissertation are the development new techniques that use mathematical tools in combination with complex dynamical models for realistic and fast propagation of uncertainty to compute statistically accurate collision probability of two objects in conjunction. These new methods of conjunction assessment are shown to perform well with significant improvements in computation speed and very high accuracy when compared to the standard Monte Carlo methods.

This work leverages a spacial solution to the Fokker-Planck equations to map the moments of the system PDF using higher order Taylor series expansions of the solution through STTs. These STTs are leveraged to account for higher order perturbations from the chosen dynamical models, starting with the two-body problem, and adding in J_2 secular effects. To introduce dynamical realism in the near-Earth propagation, a complex model from Park and Scheeres [65] is implemented for a semi-analytical computation of these STTs to incorporate perturbations from Earth oblate-

ness and SRP. This combination of the SDS and STTs allows for accurate, realistic, and efficient nonlinear mapping of the moments of the system PDF. The SDS also opens the possibility of incorporating other higher order perturbations into this solution in the future, such as the gravitational attraction due to additional objects.

GMMs are used to split the initial distributions into smaller distributions to allow: 1) reduced nonlinearity in individual component propagation, and 2) easy extension using a higher number of components for accuracy. The GMM split is achieved by extending a univariate library over a multi-dimensional split in the equinoctial frame in near-Earth space. This Gaussian sum is combined with the high order STTs for accurate nonlinear evolution of individual GMM components through individual mean and covariance mapping. The propagated Gaussian mixture components give the final non-Gaussian distribution through a weighted sum. This technique to combine the GMMs, STTs, and the high fidelity SDS for accurate and efficient distribution mapping is one of the key contributions from this dissertation. In near-Earth applications, the STTs about the nominal trajectory are used for GMM component mapping, meaning that the number of GMMs can be easily increased without a significant increase in computational load.

Although several alternative formulations of dynamical systems exist that allow the reduction of nonlinearity in the uncertainty during propagation, such as work by Aristoff et al. [7], it is important to note that the aim of the propagation methods developed in this dissertation is to serve as an application in conjunction assessment. This means that even if the nonlinearity in the selected coordinate system reduces further, the eventual comparison for conjunction analysis will be performed in Cartesian coordinates. Therefore, GMMs will still be necessary to provide a split nonlinear capture of the distribution. Additionally, the distributions will also intermediately be converted to the Delaunay frame for the SDS propagation because the dynamics equations are defined in this frame [55, 64, 65]. This means that the actual propagation occurs in the Delaunay frame. All these different tools are defined in much more details in the following chapters of this dissertation.

The GMM-STT propagated uncertainty is combined with an analytical formula of collision

probability to achieve the cumulative probability of collision of the system. This cumulative probability is achieved using a double weighted sum of individual collision probabilities from an all-on-all component-by-component comparison of the two objects in conjunction. In addition to improving computation time, the individual GMM comparison can now be performed using analytical formulas that assume a Gaussian uncertainty because each GMM component remains nearly Gaussian after propagation. Long duration conjunctions are complex to evaluate due to the lack of simplifying assumptions, leading to a nontrivial triple integral over space and time that is cumbersome to evaluate. An important realisation from the implementation of this GMM-STT propagation is that when using enough GMM components in this analysis, such that each GMM component is "small enough", each component interaction behaves like a short duration conjunction which leads to a simplification of the complex problem. This key result leads to a simplification of the complex collision probability method within the double weighted sum to evaluate the system probability of collision, which can now be applied to both short and long duration conjunctions.

The application of these tools in the cislunar space is another important contribution of this work to support the growing efforts in cislunar SSA. A similar GMM-STT approach is applied using modifications in cislunar space to evaluate conjunctions. The same method of GMM-STT propagation is combined with the Circular Restricted Three-Body Problem (CR3BP) dynamics. The GMM split is performed in the Cartesian frame and the STTs are computed using the CR3BP dynamics.

The thesis statement is as follows:

Semi-analytical fast and accurate nonlinear uncertainty propagation can lead to a significant improvement in tools used for conjunction assessment and orbit determination. Fast and accurate nonlinear uncertainty propagation can be achieved by splitting the uncertainty distribution into smaller components and propagating these components with State Transition Tensors. Incorporating higher order dynamics in these tools allows for accurate real-world applications.

The contributions from this dissertation are listed below:

(1) Novel combinations of GMM-STT propagation with advanced dynamical systems for accurate, efficient, and realistic uncertainty propagation.

(2) Application of the higher accuracy GMM-STT uncertainty mapping in short-term conjunction analysis to dramatically reduce computation time while maintaining statistical accuracy.

(3) Extension of the GMM-STT uncertainty mapping in long-term conjunction work using short-term conjunction methods, greatly improving efficiency.

(4) An online GitHub-accessible toolkit for near-Earth short-term and long-term conjunctions.

(5) Applications of this new GMM-STT uncertainty propagation method in cislunar conjunction assessment using modified GMM splitting techniques in the Cartesian frame for accurate and fast collision probability results.

1.4 Chapter Organization

Chapter 2 presents a variety of modeled dynamics that are used throughout the following chapters. One of the key dynamical systems, the SDS, is crucial to real world applications of the methods and provides a fast and accurate propagation technique. This SDS is achieved by applying a Lie series transformation to the system Hamiltonian to separate the averaged dynamics and analytical short-period variation equations. This allows a fast propagation with the averaged dynamics and an addition of short-period variations using analytical equations at relevant times. In addition to this, it also presents a solution to the Fokker-Planck equations that can be used to propagate the PDF using direct moment mapping with STTs. A mathematical background of STTs is presented, along with the analytical and semi-analytical methods of STT propagation.

Chapter 3 defines GMMs and lists the splitting methods used to achieve the splits in near-Earth and cislunar space. In near-Earth space, this split is performed by extending a univariate

library into a multi-directional split in the equinoctial frame to allow the nonlinearity to be focused in one dimension. A similar method is used in the cislunar application of GMMs, just in the cartesian space. This adds more complexity in the choice of the splitting direction because nonlinearity grows freely in all dimensions. Then, a method is proposed to propagate these GMMs using STTs to capture the full nonlinear behaviour associated with propagating the distribution with nonlinear orbit dynamics. This is the key hybrid method used for propagation to achieve a final non-Gaussian distribution. Test cases are presented at the end in near-Earth and cislunar domains to confirm the capture of nonlinear evolution of uncertainty.

Chapter 4 details the importance of uncertainty propagation in conjunction analysis methods. The categorization of conjunctions into short-term and long-term encounters is defined. Then, the numerical Monte Carlo method of uncertainty propagation is presented, which can be used as baseline truth to compare other methods against. The most important section of this chapter presents a hybrid method that combines the GMM-STT uncertainty propagation techniques developed in the previous chapter with an analytical probability of collision calculation formula. This method combines the collision probabilities from individual comparisons of GMM components of the objects in conjunction to achieve a cumulative system probability of collision. This probability of collision formula with the GMMs is converted to a reduced formula using simplifications that arise from small individual GMM component interactions.

Chapter 5 presents the analysis and performance comparison of the hybrid method of uncertainty propagation and conjunction analysis developed using mathematical tools throughout the previous chapters, relative to a numerical Monte Carlo analysis. The performance analysis is run with a variety of test cases in the near-Earth and cislunar regimes to demonstrate the statistical accuracy and wide applicability of the hybrid method. These examples use the hybrid method in combination with a variety of dynamical system formulations. A time comparison between the Monte Carlo and hybrid methods is also presented in some test cases to demonstrate the significance of this contribution.

Chapter 6 presents a code toolkit built using the hybrid method of uncertainty propagation

and conjunction analysis developed and analyzed in the previous chapters. This toolkit is accessible to the public through GitHub links provided in references [48, 47]. Some of the MATLAB tools used to develop the hybrid method are defined, along with snippets of code development. Code initialization parameters are defined and the setup of a test case is presented with the expected outputs.

The contributions and results are summarised and the future directions of this research are presented in Chapter 7.

Chapter 2

Mapping of Nonlinear System Dynamics

The evolution of uncertainty can be captured by propagating the underlying state probability density function (PDF), which is governed by a system of partial differential equations called the Fokker-Planck equations (FPEs). In Monte Carlo methods, the propagation of a collection of points from the initial distribution mimics the FPE numerical solution for propagation of the system PDF. One method to employ the FPEs in space is to implement a special solution to the FPE for deterministic dynamical systems. This can be done by considering a direct moment evolution using higher order solutions to the system dynamics [65, 67]. The moments of a distribution can be propagated using a Taylor series expansion of the system dynamics to an arbitrary order using State Transition Tensors (STTs) [66, 73, 8]. The dynamics used for the STT calculations are essential to realistic applications of this approach. The dynamical environment of an object greatly effects its motion in space. Depending on the region in space, different types of forces impact the motion. To achieve accuracy, all high-impact forces are incorporated for accurate propagation. Several systems of dynamical equations have been formulated for near-Earth and cislunar regimes.

In this chapter, a variety of dynamical systems are first introduced that will be later used in combination with the STTs, which include the Two-Body Problem (2BP) dynamics, J_2 secular dynamics, an advanced Simplified Dynamical System (SDS), and the Circular Restricted Three-Body Problem (CR3BP). Then, a mathematical background is provided for the Taylor series expansion of the system dynamics. The analytical and semi-analytical results for the STTs are presented for the 2BP, J_2 Secular dynamics, the SDS and the CR3BP.

2.1 Near-Earth Regime

For the region near Earth, the primary forces that impact an object include the gravitational force of the Earth, the gravitational potential forces due to the shape of the Earth, Solar Radiation Pressure (SRP), atmospheric drag, etc. In this section we discuss the dynamical systems used in near-Earth space in the order of their complexity and realistic applicability: 2BP, J_2 secular dynamics, and SDS.

2.1.1 Two-Body Problem

The simplest model for near-Earth dynamics is the Two-Body dynamics which makes the following simplifying assumptions: there are only two bodies in the system, gravity is the only force acting on each boy, the bodies are modeled as point and constant masses. In this simple Keplerian motion, only the true anomaly (M) evolves over time, whereas the other orbital elements remain constant. For a 2BP, the Equinoctial element set is defined using the classical orbital elements (a, e, i, Ω, ω, M) as follows:

$$\begin{aligned} a &= a & h &= e\sin(\omega+\Omega) & k &= e\cos(\omega+\Omega) \\ p &= \frac{\sin(i)\sin(\Omega)}{1+\cos(i)} & q &= \frac{\sin(i)\cos(\Omega)}{1+\cos(i)} & \lambda &= M+\omega+\Omega \end{aligned} \tag{2.1}$$

The solution flow for an Equinoctial element set can now be defined using:

$$\begin{aligned} a(t) &= a^o & h(t) &= h^o & k(t) &= k^o \\ p(t) &= p^o & q(t) &= q^o & \lambda(t) &= \lambda^o + \mathrm{n}\Delta\mathrm{t} = \lambda^o + \sqrt{\frac{\mu}{a^{o3}}}(\mathrm{t}-\mathrm{t}^o) \end{aligned} \tag{2.2}$$

Here, the superscript ^{0} represents each element at time, t_0.

2.1.2 2BP + J_2 Secular Dynamics

Earth's oblateness has a large impact on the motion of an object near Earth. In the second dynamical system, the secular effects due to Earth J_2 are considered in addition to the 2BP dynamics to propagate the information, and to compute the STTs. In this case, the classical orbital elements: argument of periapsis (ω) and right ascension of ascending node (Ω) evolve over time using constant quantities of $\dot{\omega}$ (Eq. 2.3) and $\dot{\Omega}$ (Eq. 2.4) respectively.

$$\dot{\omega} = \left[-\frac{3}{2}\frac{\sqrt{\mu}J_2R^2}{(1-e^2)a^{7/2}}\right]\left(\frac{5}{2}\sin^2(i) - 2\right) \tag{2.3}$$

$$\dot{\Omega} = \left[-\frac{3}{2}\frac{\sqrt{\mu}J_2R^2}{(1-e^2)a^{7/2}}\right]\cos(i) \tag{2.4}$$

This secular change in ω and Ω implies that the Equinoctial elements: h, k, p, q, and λ all change over time.

2.1.3 Simplified Dynamical System

Non-Keplerian perturbations play a crucial role in near-Earth propagation. This means that the dynamical system of choice makes a great difference in achieving the desired propagation. To account for perturbations from non-Keplerian dynamics due to SRP and full J_2, an advanced dynamical system is introduced. The state ($\boldsymbol{x}_{\text{del}}$) and the SDS equations of motion (EOMs: $\boldsymbol{f}_{\text{del}}$) of the objects are defined using a Delaunay element set: [L; G; H; l; g; h] in terms of classical orbital elements ([a; e; i; Ω; ω; M]):

$$\begin{array}{lll} L = \sqrt{\mu a} & G = L\sqrt{1-e^2} & H = G\cos(i) \\ l = M & g = \omega & h = \Omega \end{array} \tag{2.5}$$

The state and EOMs are represented as follows:

$$\boldsymbol{x}_{\text{del}} = [l,\ g,\ h,\ L,\ G,\ H]$$
$$\boldsymbol{f}_{\text{del}} = [\dot{l},\ \dot{g},\ \dot{h},\ \dot{L},\ \dot{G},\ \dot{H}] \tag{2.6}$$

The following subsections define the SDS from Park and Scheeres [65]. The solution flow of a system can be presented as:

$$\boldsymbol{x} = \boldsymbol{x}_0 + \boldsymbol{x}_{secular} + \boldsymbol{x}_{long} + \boldsymbol{x}_{short} \tag{2.7}$$

where, the initial state is propagated using three components of the dynamics: the secular variations, the long-period variations, and the short-period variations. The short-period and long-period terms are periodic, whereas the secular variations are not. The short-period variations add the largest amount of computation time due to the large variability. These typically repeat on the order of the satellite's period or less [77]. Figure 2.1 from Vallado [77] shows the different variations in the evolution of an orbital element.

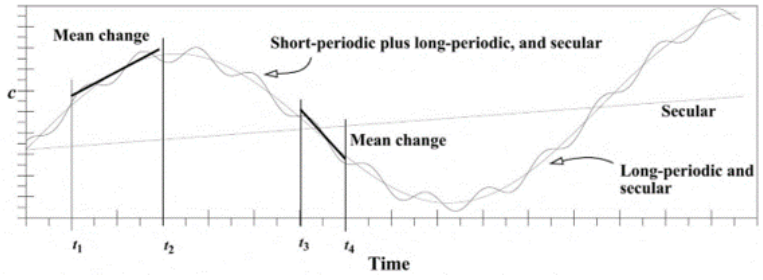

Figure 2.1: The secular, short-period, and long-period variations in the evolution of an orbital element. [77]

The SDS aims to separate the short-period variations from the secular and long-period variations to allow faster propagation with averaged dynamics. The SDS uses Lie transformation (defined by Deprit [29]) of the system Hamiltonian to achieve the mean Hamiltonian by averaging over the mean anomaly, which is the fast variable in the orbit elements. The mean system dynamics

EOMs ($\boldsymbol{f}_{\text{del}}$) are derived using the partial derivatives of the mean Hamiltonian with respect to state components. The new solution flow looks like:

$$\boldsymbol{x} = \boldsymbol{x}_0 + \boldsymbol{x}_{secular} + \boldsymbol{x}_{long} + \overline{\boldsymbol{x}_{short}} \tag{2.8}$$

where, the $\boldsymbol{x}_{short}$ term gets replaced by a constant term, $\overline{\boldsymbol{x}_{short}}$.

The Lie operator applied to the difference in the full system Hamiltonian and the mean Hamiltonian produces the generating functions, which can be used to achieve the time dependent analytical short-term variation offset equations that allow transformations between the mean and osculating states of the object. For propagation, the osculating object state is first converted to the mean state using the short-term variation equations to allow propagation using Deprit-Lie averaged dynamical flow (Eq. (2.8)). At the end time, the mean state can be converted back to the osculating state using the same time-dependent offset equations evaluated in the other direction. The following subsections defined this process in detail.

2.1.3.1 System Hamiltonian

The Hamiltonian of a system specifies the total energy of the system based on the dynamical flow. The analytical Hamiltonian function can be defined using the Delaunay state elements ($[\boldsymbol{q};\boldsymbol{p}]$), about a small parameter ϵ as follows:

$$\mathcal{H}(\boldsymbol{q},\boldsymbol{p};\epsilon) = \sum_{n\geq 0}^{\infty} \frac{\epsilon^n}{n!}\mathcal{H}_n(\boldsymbol{q},\boldsymbol{p}) = \sum_{n\geq 0}^{\infty} \frac{\epsilon^n}{n!}\mathcal{H}_{n,0}(\boldsymbol{q},\boldsymbol{p}) \tag{2.9}$$

Due to the time dependency of sun's ascending node ($h_\odot$), the total Hamiltonian needs to be *augmented* [65] to recover autonomy. A new conjugate variable pair ($k_\odot$,$K_\odot$) is introduced, which gives us an augmented Hamiltonian ($\widehat{\mathcal{H}}$) [65]. The new generalized coordinate and conjugate moment are: $k_\odot$ and $K_\odot$, respectively. These new variables are defined in Eq. (2.10).

$$k_\odot = \nu t + \text{constant} \tag{2.10a}$$

$$\dot{k}_\odot = \frac{\partial \widehat{\mathcal{H}}}{\partial K_\odot}, \quad \dot{K}_\odot = \frac{\partial \widehat{\mathcal{H}}}{\partial k_\odot} \tag{2.10b}$$

The state and EOMs are modified to accommodate the new generalised coordinates to become:

$$\boldsymbol{x}_{\text{del}} = [l,\ g,\ h,\ k_\odot, L,\ G,\ H,\ K_\odot] \tag{2.11a}$$

$$\boldsymbol{f}_{\text{del}} = [\dot{l},\ \dot{g},\ \dot{h},\ \dot{k}_\odot,\ \dot{L},\ \dot{G},\ \dot{H},\ \dot{K}_\odot] \tag{2.11b}$$

The analytical augmented Hamiltonian can then be represented as:

$$\widehat{\mathcal{H}} = \nu K_\odot + \mathcal{H} \tag{2.12}$$

This augmented Hamiltonian can be expanded as follows:

$$\widehat{\mathcal{H}} = \mathcal{H}_0 + \epsilon\mathcal{H}_1 + \frac{\epsilon^2}{2!}\mathcal{H}_2 + \frac{\epsilon^3}{3!}\mathcal{H}_3 + \frac{\epsilon^4}{4!}\mathcal{H}_4 + \frac{\epsilon^5}{5!}\mathcal{H}_5 \tag{2.13}$$

Each Hamiltonian component in the expression in Eq. (2.13) is associated with a corresponding chosen dynamics [64, 55] as defined in Eq. (2.19). $\mathcal{H}_0$, $\mathcal{H}_3$, and $\mathcal{H}_5$ are the Hamiltonians associated with the Keplerian motion, J_2, and SRP, respectively. $\mathcal{H}_2$ appears due to the augmentation to make the system autonomous.

$$\mathcal{H}_0 = -\frac{\mu}{2a} \quad \text{(Keplerian motion)} \tag{2.14a}$$

$$\mathcal{H}_2 = \frac{2!}{\epsilon^2}(\nu K_\odot) \quad \text{(augmented Hamiltonian)} \tag{2.14b}$$

$$\mathcal{H}_3 = \frac{3!}{\epsilon^3}\left[\frac{1}{2}\frac{\mu}{r}\left(\frac{\alpha}{r}\right)^2 J_2\left(\frac{3}{2}s^2 - \frac{3}{2}s^2\cos\left(2f + 2g\right) - 1\right)\right] \quad \text{(Earth oblateness)} \tag{2.14c}$$

$$\mathcal{H}_5 = \frac{5!}{\epsilon^5}\left[-\beta\frac{r}{r^2_{\odot,\text{sat}}}(T_c\cos f + T_s sinf)\right] \quad \text{(SRP)} \tag{2.14d}$$

Here,

$$\begin{aligned} T_c = \frac{1}{4}\big[&(c+1)(c_\odot+1)\cos(g+h-h_\odot-k_\odot) \\ &+(c-1)(c_\odot-1)\cos(g-h+h_\odot-k_\odot) \\ &-(c+1)(c_\odot-1)\cos(g+h-h_\odot+k_\odot) \\ &-(c-1)(c_\odot+1)\cos(g-h+h_\odot+k_\odot) \\ &+4ss_\odot\sin(g)\sin(k_\odot)\big] \end{aligned} \tag{2.15a}$$

$$\begin{aligned} T_s = \frac{1}{4}\big[&(-c-1)(c_\odot+1)\sin(g+h-h_\odot-k_\odot) \\ &-(c-1)(c_\odot-1)\sin(g-h+h_\odot-k_\odot) \\ &+(c+1)(c_\odot-1)\sin(g+h-h_\odot+k_\odot) \\ &+(c-1)(c_\odot+1)\sin(g-h+h_\odot+k_\odot) \\ &+4ss_\odot\cos(g)\sin(k_\odot)\big] \end{aligned} \tag{2.15b}$$

The solar perturbation strength (β) is defined in Eq. 2.16:

$$\beta = (1+\rho)\frac{A_{\text{sat}}}{m_{\text{sat}}}P_\Phi \tag{2.16}$$

The values of reflectivity (ρ) and the satellite area-to-mass ratio $\left(\frac{A_{\text{sat}}}{m_{\text{sat}}}\right)$ are set to be 0.2 and 2.0 $\frac{m^2}{kg}$. P_Φ is the solar constant. The small parameter, ϵ [65] (chosen to be 0.1), is used for comparison against the magnitudes of constants ν, J_2, and β to choose the placement of the Hamiltonian components in the total Hamiltonian.

2.1.3.2 Lie Transformation

This subsection presents an overview of the Lie transformation defined by Deprit [29] to investigate the Hamiltonian of a problem. The method generates a convergent, real valued series expansion for the resultant transformation. Deprit [29] created a recursive transformation of an

analytical function under the Lie transformation called the Depit Triangle:

$$
\begin{array}{ccccccccccc}
\mathcal{H}_{0,0} & & & & & & & & & & \\
| & & & & & & & & & & \\
\mathcal{H}_{1,0} & - & \mathcal{H}_{0,1} & & & & & & & & \\
| & & | & & & & & & & & \\
\mathcal{H}_{2,0} & - & \mathcal{H}_{1,1} & - & \mathcal{H}_{0,2} & & & & & & \\
| & & | & & | & & & & & & \\
\mathcal{H}_{3,0} & - & \mathcal{H}_{2,1} & - & \mathcal{H}_{1,2} & - & \mathcal{H}_{0,3} & & & & \\
| & & | & & | & & | & & & & \\
\mathcal{H}_{4,0} & - & \mathcal{H}_{3,1} & - & \mathcal{H}_{2,2} & - & \mathcal{H}_{1,3} & - & \mathcal{H}_{0,4} & & \\
| & & | & & | & & | & & | & & \\
\mathcal{H}_{5,0} & - & \mathcal{H}_{4,1} & - & \mathcal{H}_{3,2} & - & \mathcal{H}_{2,3} & - & \mathcal{H}_{1,4} & - & \mathcal{H}_{0,5} \\
| & & | & & | & & | & & | & & | \\
\mathcal{H}_{6,0} & - & \mathcal{H}_{5,1} & - & \mathcal{H}_{4,2} & - & \mathcal{H}_{3,3} & - & \mathcal{H}_{2,4} & - & \mathcal{H}_{1,5} & - & \mathcal{H}_{0,6} \\
| & & | & & | & & | & & | & & | & & |
\end{array}
$$

The Deprit Triangle (2.18)

This provides a simple way to compute the transformed Hamiltonian functions. Some examples of this computation are shown below:

$$\mathcal{O}(\epsilon^0) : \mathcal{H}_0^{(0)} = \mathcal{H}_{0,0} \tag{2.19a}$$

$$\mathcal{O}(\epsilon^1) : \mathcal{H}_0^{(1)} = \mathcal{H}_{0,1} = \mathcal{H}_{1,0} + \mathcal{L}_{\mathcal{W}_1}\mathcal{H}_{0,0} \tag{2.19b}$$

$$\mathcal{O}(\epsilon^2) : \mathcal{H}_0^{(2)} = \mathcal{H}_{0,2} = \mathcal{H}_{1,1} + \mathcal{L}_{\mathcal{W}_1}\mathcal{H}_{0,1} = \mathcal{H}_{2,0} + \mathcal{L}_{\mathcal{W}_1}(\mathcal{H}_{1,0} + \mathcal{H}_{0,1}) + \mathcal{L}_{\mathcal{W}_2}\mathcal{H}_{0,0}$$

$$\mathcal{O}(\epsilon^3) : \mathcal{H}_0^{(3)} = \mathcal{H}_{0,3} = \mathcal{H}_{3,0} + \mathcal{L}_{\mathcal{W}_1}(2\mathcal{H}_{2,0} + \mathcal{H}_{0,2}) + \mathcal{L}_{\mathcal{W}_2}(2\mathcal{H}_{1,0} + \mathcal{H}_{0,1}) + \mathcal{L}_{\mathcal{W}_3}\mathcal{H}_{0,0}$$

$$+ \mathcal{L}_{\mathcal{W}_1}\mathcal{L}_{\mathcal{W}_1}\mathcal{H}_{1,0} + \mathcal{L}_{\mathcal{W}_1}\mathcal{L}_{\mathcal{W}_2}\mathcal{H}_{0,0}$$

$$\vdots \tag{2.19c}$$

For every order of ϵ, the generating functions ($\mathcal{W}$) can be written as a form of the partial differential equation as follows:

$$\mathcal{L}_0(\mathcal{W}_n) + \mathcal{K}_n = \widetilde{\mathcal{H}}_{0,n} \tag{2.20}$$

This is called the homological equation. The Deprit-Lie method essentially allows a recursive derivation of the mean Hamiltonian and the generating functions to allow a separate representation of the mean ($\mathcal{K}$) and short-period variation ($\mathcal{W}$) terms of the total Hamiltonian. The generating function of the transformation ($\mathcal{W}$) can again be represented in a power series expansion:

$$\mathcal{W}(\boldsymbol{q}, \boldsymbol{p}; \epsilon) = \sum_{n\geq 0}^{\infty} \frac{\epsilon^n}{n!}\mathcal{W}_{n+1}(\boldsymbol{q}, \boldsymbol{p}) \tag{2.21}$$

$\mathcal{L}_0(-)$ represents the Lie operator:

$$\mathcal{L}_0(\mathcal{W}_n) = \{\mathcal{W}_n,\ \mathcal{H}_0\} = \sum_{i=1}^{N}\left(\frac{\partial \mathcal{H}_0}{\partial q_i}\frac{\partial \mathcal{W}_n}{\partial p_i} - \frac{\partial \mathcal{H}_0}{\partial p_i}\frac{\partial \mathcal{W}_n}{\partial q_i}\right) \tag{2.22}$$

The value of $N = 4$ is equal to the dimension of the $\boldsymbol{q}$ and $\boldsymbol{p}$ vectors.

Kamel [46] proposed a generalise algorithm to apply such a transformation. The analytical solutions for the mean and the generating functions can be obtained based on the theory of perturbations. This method uses the generating function ($\mathcal{W}$) to perform a canonical transformation ψ: $(\hat{\boldsymbol{q}}, \hat{\boldsymbol{p}}; \epsilon) \longmapsto (\boldsymbol{q}, \boldsymbol{q})$ defined by the solutions $\boldsymbol{q}(\hat{\boldsymbol{q}}, \hat{\boldsymbol{p}}; \epsilon)$ and $\boldsymbol{p}(\hat{\boldsymbol{q}}, \hat{\boldsymbol{p}}; \epsilon)$. The solution should satisfy:

$$\frac{\mathrm{d}\boldsymbol{q}}{\mathrm{d}t} = \frac{\partial \mathcal{W}}{\partial \boldsymbol{p}}, \qquad \frac{\mathrm{d}\boldsymbol{p}}{\mathrm{d}t} = -\frac{\partial \mathcal{W}}{\partial \boldsymbol{q}} \tag{2.23}$$

where $\boldsymbol{q}(\hat{\boldsymbol{q}}, \hat{\boldsymbol{p}}; 0) = \hat{\boldsymbol{q}}$ and $\boldsymbol{p}(\hat{\boldsymbol{q}}, \hat{\boldsymbol{p}}; 0) = \hat{\boldsymbol{p}}$ [65].

The mean Hamiltonian (that contains the secular and long-period variations) can be computed simply using averaging over the fast variable (mean anomaly):

$$\mathcal{K}_n = \frac{1}{2\pi} \int_0^{2\pi} \widetilde{\mathcal{H}}_{0,n} \mathrm{d}l \tag{2.24}$$

The Deprit triangle [29] leads to an additional J_2^2 term in the mean Hamiltonian. Using the same notations as the full Hamiltonian, the mean Hamiltonian can be represented as follows [65]:

$$\widehat{\mathcal{K}} = \mathcal{K}_0 + \epsilon \mathcal{K}_1 + \frac{\epsilon^2}{2!}\mathcal{K}_2 + \frac{\epsilon^3}{3!}\mathcal{K}_3 + \frac{\epsilon^4}{4!}\mathcal{K}_4 + \frac{\epsilon^5}{5!}\mathcal{K}_5 + \frac{\epsilon^6}{6!}\mathcal{K}_6 \tag{2.25}$$

In Eq. (2.25), each component can be calculated using the mean anomaly averaging defined above. The results from the MATLAB symbolic computer are shown in Eq. (2.26). $\mathcal{K}_0$, $\mathcal{K}_3$, and $\mathcal{K}_5$ are the mean Hamiltonians associated with the Keplerian motion, J_2, and SRP respectively. $\mathcal{K}_2$ is the averaged component of the augmentation. $\mathcal{K}_6$ is the additional J_2^2 term that appears due to the Deprit triangle from Eq. (2.18).

$$\mathcal{K}_0 = -\frac{\mu}{2a} \tag{2.26a}$$

$$\mathcal{K}_2 = \frac{2!}{\epsilon^2}(\nu K_\odot) \tag{2.26b}$$

$$\mathcal{K}_3 = \frac{3\alpha^2 J_2 \mu (3s^2-2)}{2a^3\eta^3\epsilon^3} \tag{2.26c}$$

$$\mathcal{K}_5 = -\frac{180a\beta e T_c}{\epsilon^5} \tag{2.26d}$$

$$\begin{aligned}\mathcal{K}_6 = &-\frac{45\alpha^4 J_2^2 \mu}{8a^5\eta^9\epsilon^6}\big[6e^2\eta^2 s^2(15s^2-14)\cos(2g) + e^2\{-(3\eta^2(5s^4+8s^2-8)+4(2-3s^2)^2)\} \\ &+ 4\{3\eta^3(2-3s^2)^2 + \eta^2(21s^4-42s^2+20) + (2-3s^2)^2\}\big]\end{aligned} \tag{2.26e}$$

The MATLAB symbolic computer is also used to derive the mean system Delaunay EOMs using:

$$\begin{aligned}\dot{l} = \frac{\partial\widehat{\mathcal{K}}}{\partial L}, \quad \dot{g} = \frac{\partial\widehat{\mathcal{K}}}{\partial G}, \quad \dot{h} = \frac{\partial\widehat{\mathcal{K}}}{\partial H}, \quad \dot{k}_\odot = \frac{\partial\widehat{\mathcal{K}}}{\partial K_\odot} \\ \dot{L} = -\frac{\partial\widehat{\mathcal{K}}}{\partial l}, \quad \dot{G} = -\frac{\partial\widehat{\mathcal{K}}}{\partial g}, \quad \dot{H} = -\frac{\partial\widehat{\mathcal{K}}}{\partial h}, \quad \dot{K}_\odot = -\frac{\partial\widehat{\mathcal{K}}}{\partial k_\odot}\end{aligned} \tag{2.27}$$

The resultant mean equations of motion that account for the J_2 and SRP perturbations are shared in Appendix B.

The Lie operator from Eq. (2.22) can be used to back-solve for the generating functions ($\mathcal{W}_n$) using the definition:

$$\mathcal{L}_0(\mathcal{W}_n) = \widetilde{\mathcal{H}}_{0,n} - \mathcal{K}_n \tag{2.28}$$

The generating functions corresponding to the system Hamiltonian are computed using the MATLAB symbolic computer to be:

$$\mathcal{W}_3 = \frac{3!}{\epsilon^3}\frac{L^3\alpha^2 J_2}{4\mu a^3\eta^3}\Big[-3s^2\left(\frac{1}{2}\sin 2(f+g)+\frac{1}{2}e\sin(f+2g)+\frac{1}{6}e\sin(3f+2g)\right)$$
$$+(3s^2-2)(f+e\sin f-l)\Big] \tag{2.29a}$$

$$\mathcal{W}_5 = \frac{30a\beta}{n\epsilon^5}\big(4e^2T_c\sin E+e(\eta T_s\cos 2E-T_c(6E+\sin 2E-6l))-4\eta T_s\cos E+4T_c\sin E\big) \tag{2.29b}$$

$$\mathcal{W}_6 = \frac{45\alpha^4 J_2^2 n}{8a^2e\eta^9\epsilon^6}\Big[-6e^3\eta^2s^2(15s^2-14)(f-l)\cos 2g+8(2-3s^2)^2(e^2+\eta^3-1)\sin f$$
$$+e\{2(2-3s^2)^2(e^2+\eta^3-1)\sin 2f+(f-l)(e^2(3\eta^2(5s^4+8s^2-8)+4(2-3s^2)^2)$$
$$-4(\eta^2(21s^4-42s^2+20)+(2-3s^2)^2))\}\Big] \tag{2.29c}$$

These generating functions are used to calculate the analytical offset equations to convert between the mean and osculating states, as defined in the following sub-section.

2.1.3.3 Analytical Equations for Short-Period Variation Removal and Addition

For propagation with the SDS dynamics, the osculating state ($\boldsymbol{q},\ \boldsymbol{p}$) is converted to the mean state ($\hat{\boldsymbol{q}},\ \hat{\boldsymbol{p}}$). This mean state is propagated to the desired time, t, using the averaged dynamics defined in Eq. (2.27). Short-period variation offsets can be analytically computed at this given time, t, and added back into the mean state to achieve the osculating state for accurate object information.

The conversion from the osculating state to the mean state is achieved by removal of short-period variations using offset correction [45, 64] given in Eq. 2.30:

$$\hat{\boldsymbol{q}} = \boldsymbol{q}_0^{(0)} + \sum_{n\geq 1}\frac{\epsilon^n}{n!}\boldsymbol{q}_0^{(n)} \tag{2.30a}$$

$$\hat{\boldsymbol{p}} = \boldsymbol{p}_0^{(0)} + \sum_{n\geq 1}\frac{\epsilon^n}{n!}\boldsymbol{p}_0^{(n)} \tag{2.30b}$$

Here, $\boldsymbol{q}_0^{(0)}$ and $\boldsymbol{p}_0^{(0)}$ refer to the epoch osculating state, and $\boldsymbol{q}_0^{(n)}$ and $\boldsymbol{p}_0^{(n)}$ are:

$$\boldsymbol{q}_0^{(n)} = -\hat{\boldsymbol{q}}_0^{(n)} + \sum_{1\leq j\leq n-1} C_j^n G_j \hat{\boldsymbol{q}}_0^{(n-j)},\ (n \geq 1) \tag{2.31a}$$

$$\boldsymbol{p}_0^{(n)} = -\hat{\boldsymbol{p}}_0^{(n)} + \sum_{1\leq j\leq n-1} C_j^n G_j \hat{\boldsymbol{p}}_0^{(n-j)},\ (n \geq 1) \tag{2.31b}$$

$\hat{\boldsymbol{q}}_0^{(n)}$ and $\hat{\boldsymbol{p}}_0^{(n)}$ are:

$$\hat{\boldsymbol{q}}_0^{(n)} = \frac{\partial \mathcal{W}_n}{\partial \hat{\boldsymbol{p}}} + \sum_{1\leq j\leq n-1} C_j^{n-1} G_j \hat{\boldsymbol{q}}_0^{(n-j)},\ (n \geq 1) \tag{2.32a}$$

$$\hat{\boldsymbol{p}}_0^{(n)} = -\frac{\partial \mathcal{W}_n}{\partial \hat{\boldsymbol{q}}} + \sum_{1\leq j\leq n-1} C_j^{n-1} G_j \hat{\boldsymbol{p}}_0^{(n-j)},\ (n \geq 1) \tag{2.32b}$$

C_k^n is the binomial coefficient and G_j is defined as follows:

$$G_j = \mathcal{L}_j - \sum_{0\leq m\leq j-2} C_m^{j-1} \mathcal{L}_{m+1} G_{j-m-1}, (1 \leq j \leq n) \tag{2.33}$$

where $\mathcal{L}_k$ is the Lie operator defined in Eq. 2.22.

The final mean state is converted back to the osculating state by adding back the short-period variations using offset correction defined as follows [45, 64]:

$$\boldsymbol{q} = \hat{\boldsymbol{q}}_0^{(0)} + \sum_{n\geq 1} \frac{\epsilon^n}{n!} \hat{\boldsymbol{q}}_0^{(n)} \tag{2.34a}$$

$$\boldsymbol{p} = \hat{\boldsymbol{p}}_0^{(0)} + \sum_{n\geq 1} \frac{\epsilon^n}{n!} \hat{\boldsymbol{p}}_0^{(n)} \tag{2.34b}$$

This SDS dynamics propagation combines the speed of mean dynamics propagation with the accuracy of converting back to the osculating state. The SDS propagation method is shown in Fig. 2.2.

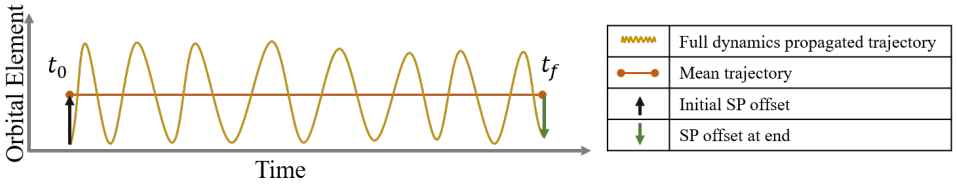

Figure 2.2: The initial osculating state is converted to the mean state for propagation with the SDS. At the final time, the final mean state is converted back to an osculating state to get an accurate final state. [50]

2.1.3.4 Simplified Dynamical System Propagation Demonstration

The SDS propagation method is also tested using an object with the set of orbital elements shown in Table 2.1. The state is first propagated using full system dynamics with SRP and J_2 perturbations. Then, the system is propagated using the SDS by converting to mean state at epoch, propagating with the averaged dynamics, and converting to the osculating state at the last orbit in this case.

Table 2.1: Orbital Elements at epoch for the SDS propagation example.

Orbital Elements	a (km)	e	i (deg)	Ω (deg)	ω (deg)	M (deg)
	8000	0.15	60	0	0	0

Fig. 2.3 show that the Delaunay orbital elements when propagated with SDS, in addition to osculating to mean and reverse conversions matches the trajectory propagated with full dynamics. In this test plot, the mean to osculating offset is added at the last orbit to see a comparison against the full dynamics propagated trajectory.

Figure 2.4 shows the short period variations in the Delaunay frame as the difference between the full dynamics propagation and the SDS propagation. At the last orbit, when the variations are added in, the difference between the two methods of propagation drops close to zero.

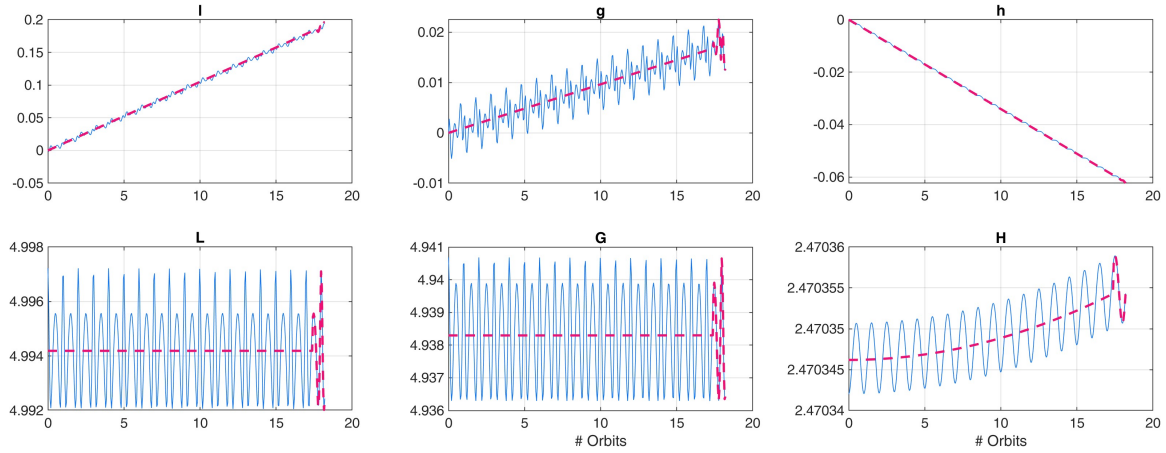

Figure 2.3: A comparison of Delaunay elements propagated with full dynamics (blue solid line) vs SDS (pink dashed line) with short-period variations added at the last orbit.

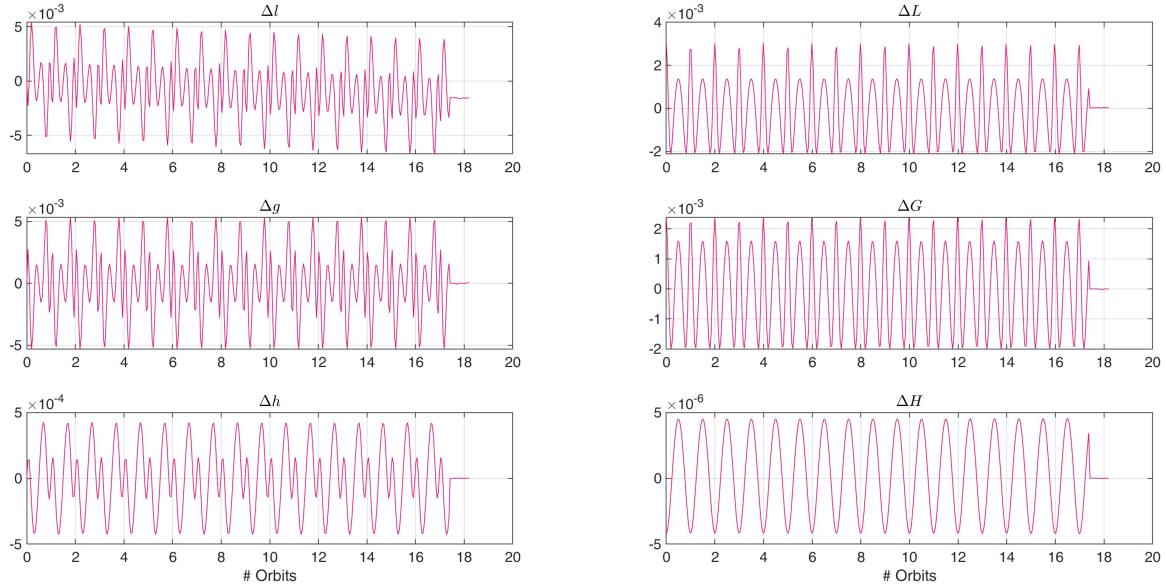

Figure 2.4: The difference between the Delaunay elements propagated with full dynamics vs SDS with short-period variations added at the last orbit.

2.2 Cislunar Regime: The Circular Restricted Three-Body Problem

In the cislunar environment, the CR3BP dynamics are introduced with the following assumptions: there are three bodies in the system, the mass of body 3 is much less than that of primaries 1 and 2, primaries 1 and 2 travel in circular orbits about their mutual barycenter, and the masses of the three bodies are modeled as point and constant masses. In the CR3BP, non-dimensional

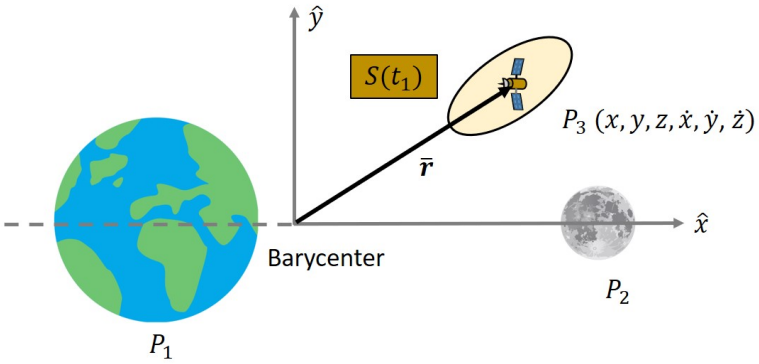

Figure 2.5: Earth, Moon, and a third body in the CR3BP rotating frame.

units are used for propagation, where the characteristic mass is the sum of the masses of the primaries. The distance between these two masses is unity and the time is characterised such that the non-dimensional gravitational constant is unity.

The non-dimensional EOMs ($\dot{\boldsymbol{x}} = \boldsymbol{f}(\boldsymbol{x})$) are defined using a pseudo-potential:

$$U(\boldsymbol{x}) = \frac{1-\mu}{r_1} + \frac{\mu}{r_2} + \frac{1}{2}(x^2 + y^2) \tag{2.35}$$

where r_1 and r_2 are the non-dimensional distances from the third body to the Earth and the Moon, respectively. μ is the mass ratio defined by:

$$\mu = \frac{m_2}{m_1 + m_2} \tag{2.36}$$

where m_1 and m_2 are the masses of the two primaries. x and y refer to the position of the third body in the barycentric system.

Based on the system pseudo-potential function, the EOMs of the system can now be defined as follows:

$$f(\boldsymbol{x}) = [\dot{x}, \dot{y}, \dot{z}, 2n\dot{y} + U_x, -2n\dot{x} + U_y, U_z]^T \tag{2.37}$$

Here, U_x, U_y, and U_z are partial derivatives of the pseudo-potential with respect to the rotating position coordinates. n represents the non-dimensional mean motion of the primary system.

2.3 State Transition Tensors

STTs (Φ) are higher order expansions of a solution that allow nonlinear mapping from initial to final state. The first term in this expansion about a nominal solution is the familiar State Transition Matrix (a second order mathematical tensor), with the inclusion of higher order terms resulting in higher order tensors. In case of simple Keplerian dynamics, these higher order STTs can be computed purely analytically because the final state and initial state have a direct analytical relationship. Because of the lack of this simple analytical mapping in the case of non-Keplerian dynamics, STTs can be computed through numerical propagation. This is done by initiating the STT with an identity matrix in the first order and zeros in all higher orders, and computing the STT EOMs ($\dot{\Phi}$) using the system dynamics. In this work, second-order STTs are used to map the means and covariances of each GMM component to the desired times. It is implied that as nonlinearity growth increases there is a need to go to higher orders of the STTs for an accurate uncertainty capture.

2.3.1 Mathematical Formulation

Suppose the EOMs that govern the motion of an orbiting object are:

$$\dot{\boldsymbol{x}} = f(t, \boldsymbol{x}(t)), \quad \boldsymbol{x}(t) = \phi(t; \boldsymbol{x}^0, t^0) \tag{2.38}$$

with ϕ representing the solution flow.

Taking the Taylor series expansion of the solution function about some reference trajectory, the state deviation ($\delta\boldsymbol{x}(t) = \phi(t; \boldsymbol{x}^0 + \delta\boldsymbol{x}^0, t^0) - \phi(t; \boldsymbol{x}^0, t^0)$) with respect to the nominal trajectory and its dynamics can be written using the Einstein summation with Dyadic notation [37] as follows:

$$\delta\boldsymbol{x}(t) = \sum_{p=1}^{m} \frac{1}{p!} \Phi_{i,k_1 \ldots k_p} \boldsymbol{x}^o_{k_1} \ldots \boldsymbol{x}^o_{k_p} \tag{2.39a}$$

$$\delta\dot{\boldsymbol{x}}(t) = \sum_{p=1}^{m} \frac{1}{p!} A_{i,k_1 \ldots k_p} \boldsymbol{x}_{k_1} \ldots \boldsymbol{x}_{k_p} \tag{2.39b}$$

Here, i and k_j stand for i^{th} and k_j^{th} elements of the state vector, respectively, and m is the order of the STT being calculated. The i^{th} component is not summed over.

Given the dynamics, f, and the solution flow, ϕ, of an object, the STTs can now be calculated by taking partial derivatives of the state at time t, with respect to the initial state, $\boldsymbol{x}^0$:

$$\Phi_{i,k_1\ldots k_p} = \left.\frac{\partial^p \boldsymbol{x}_i}{\partial \boldsymbol{x}^o_{k_1}\ldots\partial \boldsymbol{x}^o_{k_p}}\right|_* \tag{2.40a}$$

$$A_{i,k_1\ldots k_p} = \left.\frac{\partial^p \boldsymbol{f}_i}{\partial \boldsymbol{x}_{k_1}\ldots\partial \boldsymbol{x}_{k_p}}\right|_* \tag{2.40b}$$

Here, A denotes the local dynamics tensor (LDT) and the subscript $_*$ implies that the STT and the LDT are evaluated over the nominal trajectory.

The STT can be simply computed with time dependency where an analytical solution exists between the initial and final states, such as 2BP and J_2 secular dynamics. In these cases where an analytical relationship exists, Eq. 2.40 gives an analytical expression for Φ. This analytical computation for Φ makes the propagation purely analytical for 2BP and J_2 secular cases.

On the other hand, when considering the averaged dynamics from the SDS and the CR3BP, no such analytical state propagation relationship exists and the future state has to be calculated through numerical integration. Therefore, Φ also needs to be numerically propagated to the final time. This numerical integration is performed using an initial STT, Φ_0, consisting of the identity matrix at its first order ($I_{6\times6}$), and zeros everywhere else. The system of equations to propagate Φ_0 forward in time, can be calculated using Eq. 2.41:

$$\dot{\Phi}_{i,ab} = \sum_{\alpha=1}^{N} A_{i,\alpha}\Phi_{\alpha,ab} + \sum_{\alpha=1}^{N}\sum_{\beta=1}^{N} A_{i,\alpha\beta}\Phi_{\alpha a}\Phi_{\beta b} \tag{2.41}$$

where i, a, and b subscripts for $\dot{\Phi}$ represent the three dimensions of a second-order STT. The LDTs (A) come from Eq. (2.40).

2.3.2 Nonlinear Mapping of Moments with State Transition Tensors

A Gaussian PDF of the deviated system can be expressed using the initial mean of the deviated state ($\delta\boldsymbol{m}$) and the covariance ($\boldsymbol{P}$) associated with the system at a given time, where N is the dimension of the state deviation, $\delta\boldsymbol{x}$:

$$p_g(\delta\boldsymbol{x}) = \frac{1}{\sqrt{(2\pi)^N|\boldsymbol{P}|}} \exp\left\{-\frac{1}{2}(\delta\boldsymbol{x}-\delta\boldsymbol{m})^T\boldsymbol{P}^{-1}(\delta\boldsymbol{x}-\delta\boldsymbol{m})\right\} \tag{2.42}$$

Previous works [64] have shown that the moments of this PDF can be propagated using STTs. The mean of the PDF can be propagated nonlinearly as:

$$\delta\boldsymbol{m}_i(t) = \sum_{p=1}^{m}\frac{1}{p!}\Phi_{i,k_1\ldots k_p}\ E[\delta\boldsymbol{x}^0_{k_1}\ldots\delta\boldsymbol{x}^0_{k_p}] \tag{2.43}$$

Similarly, the covariance of the PDF can be propagated as:

$$\boldsymbol{P}_{ij}(t) = \left(\sum_{p=1}^{m}\sum_{q=1}^{m}\frac{1}{p!q!}\Phi_{i,k_1\ldots k_p}\Phi_{j,l_1\ldots l_q}E[\delta\boldsymbol{x}^0_{k_1}\ldots\delta\boldsymbol{x}^0_{k_p}\delta\boldsymbol{x}^0_{l_1}\ldots\delta\boldsymbol{x}^0_{l_q}]\right) - \delta\boldsymbol{m}_i(t)\delta\boldsymbol{m}_j(t) \tag{2.44}$$

Here, m stands for the order of STT being used. i, j, k_b, and l_c represent the i^{th}, j^{th}, k_b^{th}, and l_c^{th} elements of the state vector, respectively. $\delta\boldsymbol{m}$ is the mean offset and $\boldsymbol{P}$ is the covariance of the system PDF.

E represents the moments of the distribution [67]. Moments up to the fourth order are plugged into Eq. (2.43) and Eq. (2.44) to achieve the second order mean and covariance propagation equations, respectively:

$$\begin{aligned}
E[\delta\boldsymbol{x}_i] &= \delta\boldsymbol{m}_i \\
E[\delta\boldsymbol{x}_i\delta\boldsymbol{x}_j] &= \delta\boldsymbol{m}_i\delta\boldsymbol{m}_j + \boldsymbol{P}_{ij} \\
E[\delta\boldsymbol{x}_i\delta\boldsymbol{x}_j\delta\boldsymbol{x}_k] &= \delta\boldsymbol{m}_i\delta\boldsymbol{m}_j\delta\boldsymbol{m}_k + (\delta\boldsymbol{m}_i\boldsymbol{P}_{jk} + \delta\boldsymbol{m}_j\boldsymbol{P}_{ik} + \delta\boldsymbol{m}_k\boldsymbol{P}_{ij}) \\
E[\delta\boldsymbol{x}_i\delta\boldsymbol{x}_j\delta\boldsymbol{x}_k\delta\boldsymbol{x}_l] &= \delta\boldsymbol{m}_i\delta\boldsymbol{m}_j\delta\boldsymbol{m}_k\delta\boldsymbol{m}_l + (\delta\boldsymbol{m}_i\delta\boldsymbol{m}_j\boldsymbol{P}_{kl} + \delta\boldsymbol{m}_i\delta\boldsymbol{m}_k\boldsymbol{P}_{jl} + \delta\boldsymbol{m}_i\delta\boldsymbol{m}_j\boldsymbol{P}_{kl} + \delta\boldsymbol{m}_j\delta\boldsymbol{m}_k\boldsymbol{P}_{il} + \\
&\quad \delta\boldsymbol{m}_i\delta\boldsymbol{m}_l\boldsymbol{P}_{jk} + \delta\boldsymbol{m}_j\delta\boldsymbol{m}_l\boldsymbol{P}_{ik} + \delta\boldsymbol{m}_k\delta\boldsymbol{m}_l\boldsymbol{P}_{ij}) + \boldsymbol{P}_{ij}\boldsymbol{P}_{kl} + \boldsymbol{P}_{ik}\boldsymbol{P}_{jl} + \boldsymbol{P}_{il}\boldsymbol{P}_{jk}
\end{aligned} \tag{2.45}$$

These moments can be expanded to higher orders for propagation with higher order STTs.

2.3.3 State Transition Tensors for Near-Earth and Cislunar Regions

In this section, the STTs are computed directly for the 2BP and J_2 secular dynamics, and the STT EOMs are computed for the SDS and the CR3BP.

2.3.3.1 Two-Body Problem

Using Eq. (2.40) and the solution flow from Eq. (2.2), an STT of order p can be computed using the partial derivatives to be:

$$\Phi_{i,k_1\ldots k_p} = \begin{cases} (-1)^p \sqrt{\mu}\, \frac{(2p+1)!}{2^{2p} p! (a^0)^{p+\frac{3}{2}}}\, \Delta \mathrm{t} & i = 1 \text{ and } k_1 = k_2 = \ldots = k_p = 1 \\ 1 & p = 1 \text{ and } k_1 = i \\ 0 & \text{elsewhere} \end{cases} \tag{2.46}$$

This STT formulation can be used to directly map the deviated mean ($\delta \boldsymbol{m}$) and covariance ($\boldsymbol{P}$) of a system PDF using Eq. (2.43) and Eq. (2.44) to map the PDF in time.

2.3.3.2 J_2 Secular Dynamics

Similar to the 2BP case, the STT for J_2 secular dynamics can be compute using Eq. (2.40) and the solution flow from Eq. (2.2):

$$\Phi_{i,k_1\ldots k_p} = \begin{cases} (-1)^p\sqrt{\mu}\,\frac{(2p+1)!}{2^{2p}p!(a^o)^{p+\frac{3}{2}}}\,\Delta\mathrm{t} & k_1 = k_2 = \ldots = k_p = 1 \text{ and } i = 1 \\ 1 & p = 1,\ k_1 = i \text{ and } i = 1, 6 \\ \cos\left(\dot{\omega}\right) & p = 1,\ k_1 = i \text{ and } i = 2, 3 \\ \cos\left(\dot{\Omega}\right) & p = 1,\ k_1 = i \text{ and } i = 4, 5 \\ \sin\left(\dot{\omega}\right) & p = 1,\ k_1 = 3 \text{ and } i = 2 \\ -\sin\left(\dot{\omega}\right) & p = 1,\ k_1 = 2 \text{ and } i = 3 \\ \sin\left(\dot{\Omega}\right) & p = 1,\ k_1 = 5 \text{ and } i = 4 \\ -\sin\left(\dot{\Omega}\right) & p = 1,\ k_1 = 4 \text{ and } i = 5 \\ 0 & \text{elsewhere} \end{cases} \tag{2.47}$$

Same as before, this STT formulation can be used to map the system PDF to the desired time.

2.3.3.3 Simplified Dynamical System

As described in previous sections, there is not direct analytical mapping between the final and initial states in the SDS. This means that the STT needs to be numerically propagated to the desired time using the STT EOMs (Eq. (2.41)), which are calculated using the LDTs. The averaged dynamics solution flow from Eq. (2.27) is used to compute the LDTs from Eq. (2.40) in the Delaunay frame:

$$A_{1st} = \frac{\partial \boldsymbol{f}_{\mathrm{del}}(\boldsymbol{x}_{\mathrm{del}})}{\partial \boldsymbol{x}_{\mathrm{del}}},\ \ A_{2nd} = \frac{\partial A_{1\mathrm{st}}}{\partial \boldsymbol{x}_{\mathrm{del}}},\ \ \ldots \tag{2.48}$$

The moment propagation process in the SDS is as follows. First, the osculating initial $\delta\boldsymbol{m}$ is converted to the mean $\delta\boldsymbol{m}$ using Eq. (2.30). The STTs are propagated to the desired time using the mean dynamics generated STT EOMs. The $\delta\boldsymbol{m}$ and $\boldsymbol{P}$ are mapped to this time using Eq. (2.43) and Eq. (2.44). Then, the short-period variations are added to $\delta\boldsymbol{m}$ to achieve the osculating state

mean using Eq. 2.34. This process is similar to that described previously in Figure 2.2, simply replacing the numerical propagation with the STT mapping.

2.3.3.4 Cislunar Space: Circular Restricted Three-Body Problem

In the CR3BP, the STTs are again propagated numerically using the STT EOMs (Eq. (2.41)), which are calculated using the LDTs. The CR3BP dynamics solution flow from Eq. (2.37) is used to compute the LDTs from Eq. (2.40) in the Delaunay frame:

$$A_{1st} = \frac{\partial \boldsymbol{f}(\boldsymbol{x})}{\partial \boldsymbol{x}}, \quad A_{2nd} = \frac{\partial A_{1\text{st}}}{\partial \boldsymbol{x}}, \quad ... \tag{2.49}$$

Once the STTs are mapped to the desired time, the moments of the PDF ($\delta \boldsymbol{m}$ and $\boldsymbol{P}$) can simply be mapped to this time using Eq. (2.43) and Eq. (2.44)

2.4 Conclusion

In this chapter, a variety of dynamical systems are presented for use in near-Earth and cislunar domains including; Two-Body Problem (2BP) dynamics, J_2 secular dynamics, a Simplified Dynamical System (SDS), and the Circular Restricted Three-Body Problem (CR3BP). A method is developed to propagate the system probability density function (PDF) by direct moment mapping using State Transition Tensors (STTs). STTs are higher order Taylor series expansions of the system dynamical flow. After a mathematical background on STT calculations, equations are defined to propagated mean and covariance associated with a system PDF. Then, STT computations are defined for different dynamical systems of choice.

Chapter 3

Semi-Analytical Propagation of Uncertainty

In this chapter, we define a method of state and uncertainty propagation that combines two mathematical tools: Gaussian Mixture Models (GMMs) and State Transition Tensors (STTs). The initial Gaussian uncertainty of an object can be split into smaller Gaussian distributions using GMM splitting. These smaller distributions preserve linearity for longer propagation times. STTs are used to propagate these small individual GMM component distributions to the desired time. Smaller distributions have a multi-fold purpose: due to their preservation of linearity they can be more accurately mapped using lower order STTs, allowing lower computation costs; and the nearly-Gaussian final individual GMM components can later be combined with conjunction methods that assume Gaussian uncertainty for the objects in conjunction. A benefit of this method is that the number of GMM components can be easily increased, without a major impact on the computation time.

The outline of this chapter is as follows. First, the mathematical definition of GMMs is presented. This is followed by GMM splitting techniques. The GMM split is applied in the equinoctial frame in near-Earth space using a suboptimal algorithm from Horwood et al. [39], that extends a univariate library to apply it to a multi-directional split. A similar splitting process is implemented in the cislunar space in the Cartesian frame using a combination of methods from Huber et al. [40] and Vittaldev et al. [81, 80]. Then, the combination of these GMMs with STTs is defined to achieve propagation with different dynamical systems. Lastly, two examples are presented, one each in near-Earth and cislunar space, that demonstrate the ability of this uncertainty propagation

method by validating it against numerically propagated distributions.

3.1 Gaussian Mixture Models

Given a mean ($\boldsymbol{m}$) and covariance ($\boldsymbol{P}$) associated with an object at a given time, the Gaussian PDF is defined as follows, where N is the dimension of the random variable, $\boldsymbol{x}$:

$$p_g(\boldsymbol{x}) = \frac{1}{\sqrt{(2\pi)^N |\boldsymbol{P}|}} \exp\left\{-\frac{1}{2}(\boldsymbol{x}-\boldsymbol{m})^T \boldsymbol{P}^{-1}(\boldsymbol{x}-\boldsymbol{m})\right\} \tag{3.1}$$

This system PDF of $\boldsymbol{x}$ can also be expressed as a uniformly converging series of n Gaussian PDFs, or GMMs, as shown below [34, 28]:

$$p(\boldsymbol{x}) = \sum_{\alpha=1}^{n} w_\alpha p_g(\boldsymbol{x}; \boldsymbol{\mu}_\alpha, \boldsymbol{P}_\alpha) \tag{3.2}$$

where the weights associated with each GMM component are defined as:

$$0 \leq w_\alpha \leq 1, \quad i \in \{1, 2, 3, ...n\} \tag{3.3a}$$

$$\sum_{\alpha=1}^{n} w_\alpha = 1 \tag{3.3b}$$

Here, $\boldsymbol{\mu}_\alpha$ and $\boldsymbol{P}_\alpha$ are the means and covariances of the α^{th} GMM component.

A graphic of a nine-component GMM split is shown in Figure 3.1a. Here, the satellite denotes the nominal state and the largest black ellipse represents the full uncertainty. The black plus signs and the smaller ellipses correspond to the means and covariances associated with the GMM components, respectively. The Figure shows weight gradation, where darker colors represent higher component weights centered near the nominal. As previously explained, each individual GMM component mean and covariance can be propagated to the final time and the weighted sum of the final components (Eq. (3.2)) equals the final nonlinear distribution. Figure 3.1b shows that even though each individual GMM component stays nearly Gaussian, the final non-Gaussian distribution is captured by the combination of the propagated GMM components.

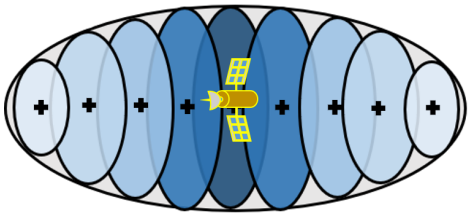

(a) Gaussian split. The darker the blue of each component, the higher the associated weight.

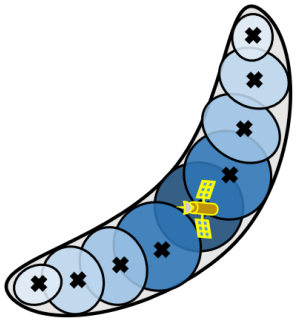

(b) Propagated GMM captures the non-Gaussian evolution of the distribution.

Figure 3.1: These figures show the initial and final distributions constituting the GMM components.

The main reason behind performing such a split is to allow for "smaller" distributions to be accurately mapped to a future time, which ensures that the linearity is preserved for a longer amount of time. This way each propagated small distribution remains approximately Gaussian for an accurate analytical conjunction analysis. The next section defines how this split can be performed to retrieve weights, means, and covariances that can be combined in a weighted sum to fully capture the distribution PDF.

3.2 Gaussian Mixture Model Splitting Methods

In this section, a variety of GMM splitting methods are defined that can accurately capture the PDF of the distribution.

3.2.1 Near-Earth Region

Generally, the distribution is split along the direction of largest nonlinearity growth, so that the components can be stretched along that direction. A concern with using Cartesian elements is that nonlinearity grows in all six dimensions. This is why alternate element sets are considered in near-Earth GMM splitting. In the equinoctial orbital elements, nonlinearity only grows in the mean anomaly direction, when using Keplerian dynamics. With non-Keplerian dynamics, such as perturbations from J_2 and SRP, the nonlinearity still grows in that one dimension, with nearly-

linear propagation in the other five dimensions. Due to this smoothing effect, element sets such as the equinoctial element set are used in GMM splitting.

This growth of nonlinearity in one dimension means that in the near-Earth space, the GMM split can be a convenient unidirectional split with the use of the equinoctial set, that allow the largest uncertainty growth to be restricted to one dimension of the set. Horwood et al. [39] created a sub-optimal algorithm that can be used to split the distribution into a desired number of components. In applications of this GMM splitting, there need to be enough GMM components to completely capture the full distribution. More GMM components imply that each GMM component has a smaller associated covariance. Appropriate number of components allow for accurate propagation and coverage of the entire distribution. The weights, means, and covariances of the GMM components are computed using the Horwood algorithm. Figure 3.2 shows the weight distribution of a 37 component split, with respect to the component means. As expected, the highest weighted component is nearest to the nominal trajectory and the further the component gets from the nominal, the lower the associated weight. This is clear from Figure 3.2, where the weight reduces exponentially the further you move from the center. The GMM split can be verified by comparing the PDF of the total distribution to the weighted sum of the GMM component PDFs (Eq. (3.2)).

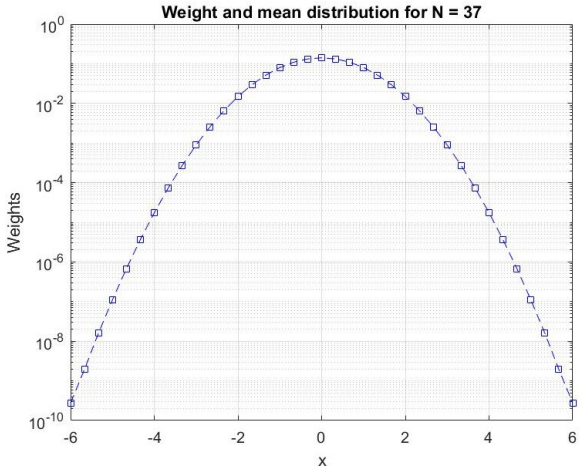

Figure 3.2: The distribution of weights relative to the means of GMM components. [49]

The optimization problem defined by Horwood et al. [39] is based in equinoctial frame to allow the nonlinearity to be bound in one direction to allow a simple one-direction split that can later be extended over the six-dimensional space. The L2 optimization problem introduced is solved once offline to generate the univariate weights, means, and standard deviation to allow easy use online. To avoid the complications that come with a non-smooth nonlinear optimization problem, this method uses a suboptimal solution based on a cost function that compares the moments of the total distribution with the summed total distribution. The refinement happens along the semi-major axis direction to limit the uncertainty growth in-track. There are a few assumptions made for simplification. One is that the means are fixed using a chosen value depending on the standard deviation, and therefore the optimization is over weights only. Covariance sizes of all GMM components are also set to be equal. Also the weights are restricted to between 0 and 1 and the sum of weights is set to 1. All these simplifications work towards a "fitting" problem to have weights and means assigned to each component in turn also generating the same smaller covariance for each GMM component. The Horwood suboptimal algorithm is adopted using a parameter, m (use $m = 4$ for less than 17 components and $m = 6$ for a larger number of components), to initiate the splitting process. Based on this, the following algorithm is set up.

The standard deviation is computed using:

$$\sigma = \frac{2m}{N-1} \tag{3.4}$$

where, N is the number of GMM components to split into.

For $\alpha = 1, ..., N$, the univariate means can be calculated using:

$$\mu_\alpha = -m + \sigma(\alpha - 1) \tag{3.5}$$

These weights, means, and σ can be used to compute matrix $(\boldsymbol{M})_{\alpha\beta} = \mathcal{N}(\nu_\alpha - \nu_\beta; 0, 2\sigma^2)$ and vector $(\boldsymbol{n})_\alpha = \mathcal{N}(\nu_\alpha; 0, \sigma^2 + 1)$ using function normpdf. An optimization problem is set up using quadprog, with 'ConstraintTolerance' of 10^{-25} and 'OptimalityTolerance' of 10^{-25} to

minimize: $\frac{1}{2}\boldsymbol{w}^T\boldsymbol{M}\boldsymbol{w} - \boldsymbol{w}^T\boldsymbol{n}$ over $\boldsymbol{w}$ subject to constraints: $\sum_{\alpha=1}^{N} w_\alpha = 1$ and $w_\alpha \geq 0$, where $\alpha = 1, ..., N$. For same α, calculate $\tilde{w}_\alpha = \frac{\sqrt{2\pi}}{\sqrt{1-\sigma^2}} w_\alpha \exp\left[\frac{\mu_\alpha^2}{2(1-\sigma^2)}\right]$, $\tilde{\mu}_\alpha = \frac{\mu_\alpha}{1-\sigma^2}$, and $\tilde{\sigma}^2 = \frac{\sigma^2}{1-\sigma^2}$. Compute $\hat{\mu}_\alpha = \nu^1 + \sqrt{Q^1}\tilde{\mu}_\alpha$, $\hat{w}_\alpha = \tilde{w}_\alpha$, and $\hat{\sigma}^2 = \tilde{\sigma}^2 Q^{11}$.

Based on this, the GMM component covariance becomes: $\bar{\boldsymbol{Q}} = (\hat{\sigma}^{-2}\boldsymbol{e}_1\boldsymbol{e}_1^T + \boldsymbol{Q}^{-1})^{-1}$, the GMM component means are: $\bar{\boldsymbol{\nu}}_\alpha = \bar{\boldsymbol{Q}}(\hat{\sigma}^{-2}\hat{\mu}_\alpha\boldsymbol{e}_1 + \boldsymbol{Q}^{-1}\boldsymbol{\nu})$, and $\bar{w}_\alpha = \hat{w}_\alpha \mathcal{N}(\hat{\mu}_\alpha - \boldsymbol{e}_1^T\boldsymbol{\nu}; 0, \hat{\sigma}^2 + \boldsymbol{e}_1^T\boldsymbol{Q}\boldsymbol{e}_1)$, where $\boldsymbol{e}_1 = (1, 0, ..., 0)^T \in \mathbb{R}$. Lastly, re-normalize the weights: $\bar{w}_\alpha = \bar{w}_\alpha / \sum_{\beta=1}^{N} \bar{w}_\beta$.

This algorithm outputs the desired weights, means, and covariances for a GMM mixture with N components.

3.2.2 Cislunar Region

Previous works [39] have developed efficient methods of using one-dimensional GMM splitting that can then be extended to achieve the full six-dimensional sets of each component. Work by Horwood et al. [39] performs such a one-dimension split for an equinoctial element set in near-Earth applications. In cislunar space, the initial distribution needs to be split in the Cartesian frame, where nonlinearity grows in all six-dimensions. This means that the direction chosen for the unidirectional split becomes important to capture the largest direction of nonlinearity growth.

The multivariate Gaussian distribution in cislunar space is approximated by GMMs by applying a unidirectional splitting library along a desired direction. The univariate splitting library, precomputed in Huber et al. [40] for up to 39 components, defines the locations of means, weights, and standard deviations to approximate the standard normal distribution. The multi-directional split is achieved by applying this library along a desired column of the covariance matrix of the initial Gaussian distribution. The multivariate split ensures a better approximation of the non-Gaussian final PDF. To achieve the best split to capture this final non-Gaussian PDF, it is essential to apply the univariate library in the direction of largest nonlinear behaviour.

Huber et al. [40] and DeMars et al. [25] use eigen factorization of the initial covariance matrix to account for the largest direction of nonlinearity. The eigenvector associated with the largest eigenvalue of this initial covariance matrix provides the direction of largest initial uncertainty, mean-

ing that the GMM components get spread out over this largest uncertainty nonlinearity direction at the initial split. In this section, eigen factorization is one of the methods used to select the direction of GMM splitting. Eq. (3.6) shows the eigen decomposition of the covariance matrix, $\boldsymbol{P}$:

$$\boldsymbol{P} = \boldsymbol{V}\Lambda\boldsymbol{V}^T \tag{3.6}$$

Here, $\boldsymbol{V}$ is a matrix containing all eigenvectors of the covariance matrix. Λ is a diagonal matrix whose diagonal elements correspond to the eigenvalues of the matrix.

Although a great preliminary splitting direction, the eigen factorization of the initial covariance matrix only gives us the largest nonlinearity direction of the initially chosen covariance. It does not consider the largest direction of nonlinearity growth because of the system dynamics. In many problems, where the covariance is large, this can be sufficient to capture the spread of the propagated uncertainty. However, in some cases, with smaller initial covariances and/or long propagation times, it is also important to consider the nonlinearity growth direction based on the system dynamics. Therefore, another method is tested where the eigen decomposition of the propagated covariance is used to determine the direction of split. This leads to the coverage of the nonlinearity from the covariance size and STT nonlinearity growth direction.

Eigen factorization is just one method that allows a direction selection for the GMM split. It is important to have a parameter that can be used to compute the nonlinearity growth in different directions to quantify the most useful direction to split the GMM. To quantify the nonlinearity growth in different test directions, Vittaldev et al. [81] develops a nonlinearity metric that deviates the nominal trajectory in the chosen test direction and propagates the deviated trajectory to compute the offset from the nominal at the final time. This allows the nonlinearity growth to be captured. Vittaldev et al. [81] recommends testing along the following directions: $\boldsymbol{r}_x$, $\boldsymbol{r}_y$, $\boldsymbol{r}_z$, $\boldsymbol{v}_x$, $\boldsymbol{v}_y$, $\boldsymbol{v}_z$, $\boldsymbol{r}_r$, $\boldsymbol{r}_v$, $\boldsymbol{r}_h$, $\boldsymbol{r}_t$, $\boldsymbol{v}_r$, $\boldsymbol{v}_v$, $\boldsymbol{v}_h$, $\boldsymbol{v}_t$. Here, the last eight vector subscripts r, v, h, and t stand for the position and velocity vectors computed along unit vector directions of: $\boldsymbol{r}$, $\boldsymbol{v}$, $\boldsymbol{h} = \boldsymbol{r} \times \boldsymbol{v}$, and $\boldsymbol{t} = \boldsymbol{h} \times \boldsymbol{r}$, respectively. The splitting direction choice is based on the direction associated with

the largest value of the nonlinearity parameter from Vittaldev et al. [81], among the test directions mentioned above. In addition to these test directions, our paper also tests this parameter using the initial eigen vectors and the propagated covariance eigen vectors.

The Vittaldev nonlinearity parameter [79] for any chosen direction, $\boldsymbol{a}$, is defined as follows, with deviations measured about the nominal initial state, $\bar{\boldsymbol{x}}$:

$$\phi = \left|\left| \frac{f(\bar{\boldsymbol{x}} + \tilde{h}\sigma_{||\hat{\boldsymbol{a}}}\hat{\boldsymbol{a}}) + f(\bar{\boldsymbol{x}} - \tilde{h}\sigma_{||\hat{\boldsymbol{a}}}\hat{\boldsymbol{a}}) - 2f(\bar{\boldsymbol{x}})}{2\tilde{h}^2} \right|\right|_2 \tag{3.7}$$

where $\tilde{h} = \sqrt{3}$ and

$$\sigma_{||\hat{\boldsymbol{a}}} = ||\boldsymbol{S}^{-1}\hat{\boldsymbol{a}}||_2^{-1} \tag{3.8}$$

Here, $\boldsymbol{S}$ is the square-root factor of the covariance matrix, $\boldsymbol{P}$, such that $\boldsymbol{P} = \boldsymbol{S}\boldsymbol{S}^T$.

Larger values of ϕ correspond to more nonlinear behaviour, whereas smaller values correspond to less nonlinearity. Upon testing different directions with this metric, the split is performed along the direction with the largest ϕ value, indicating the largest nonlinearity growth direction. This also introduces the possibility of multi-directional splits, by allowing the ranking of different directions by their nonlinear behaviours. For instance, if the highest two $\boldsymbol{\phi}$ values are close to each other, the split can be performed in both directions one after the other to capture nonlinearity growth more closely [81].

Once a direction of splitting is established, the splitting can be performed as follows:

$$\boldsymbol{m}_i = \boldsymbol{m} + m_i\boldsymbol{S}\hat{\boldsymbol{a}}_* \tag{3.9a}$$

$$\boldsymbol{P}_i = \boldsymbol{S}[\boldsymbol{I}_6 + (\sigma_i^2 - 1)\hat{\boldsymbol{a}}_*\hat{\boldsymbol{a}}_*^T]\boldsymbol{S}^T \tag{3.9b}$$

Here, $\boldsymbol{m}$ is the nominal state and $\boldsymbol{m}_i$ and $\boldsymbol{P}_i$ are the mean and covariance associated with the i^{th} GMM component, respectively. The vector $\hat{\boldsymbol{a}}_*$ is:

$$\hat{\boldsymbol{a}}_* = \frac{\boldsymbol{S}^{-1}\boldsymbol{a}}{|\boldsymbol{S}^{-1}\boldsymbol{a}|} \tag{3.10}$$

m_i, σ_i, and weights associated with each component are introduced from the precomputed libraries from Huber et al. [40].

3.3 Combining Gaussian Mixture Models and State Transition Tensors

As described in the previous chapter, STTs can be computed using the chosen dynamics in near-Earth and cislunar space. These STTs are used to map the means and covariances of the GMM components to the desired time. This mapping is performed using:

$$\delta \boldsymbol{m}_i^{\alpha}(t) = \sum_{p=1}^{m} \frac{1}{p!} \Phi_{i,k_1 \ldots k_p} \; E[\delta \boldsymbol{x}_{k_1}^0 \ldots \delta \boldsymbol{x}_{k_p}^0] \tag{3.11a}$$

$$\boldsymbol{P}_{ij}^{\alpha}(t) = \left(\sum_{p=1}^{m} \sum_{q=1}^{m} \frac{1}{p!q!} \Phi_{i,k_1 \ldots k_p} \Phi_{j,l_1 \ldots l_q} E[\delta \boldsymbol{x}_{k_1}^0 \ldots \delta \boldsymbol{x}_{k_p}^0 \delta \boldsymbol{x}_{l_1}^0 \ldots \delta \boldsymbol{x}_{l_q}^0] \right) - \delta \boldsymbol{m}_i(t) \delta \boldsymbol{m}_j(t) \tag{3.11b}$$

Here, m stands for the order of STT being used, which is two in this case. i, j, k_b, and l_c represent the i^{th}, j^{th}, k_b^{th}, and l_c^{th} elements of the state vector, respectively. $\delta \boldsymbol{m}^{\alpha}$ is the mean offset and $\boldsymbol{P}^{\alpha}$ is the covariance of the α^{th} GMM component of the distribution. E represents the moments of the distribution [67], as defined in Eq. (2.45).

The GMM components are individually propagated using STTs to capture the final nonlinear uncertainty distribution. Each GMM component mean and covariance is individually propagated using STTs. The final distribution is captured by a weighted sum of these propagated GMM components. Figure 3.3 demonstrates the nonlinear evolution of the distribution and its capture using the GMM-STT propagation.

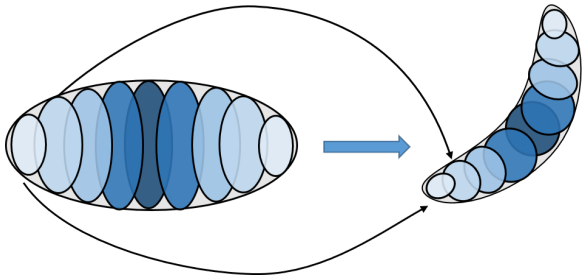

Figure 3.3: Propagation of uncertainty using the GMM-STT method. [49]

As described in the previous chapter, the 2BP and J_2 secular STTs are purely time-dependent and computed analytically. On the other hand, the Simplified Dynamics System (SDS) and Circular Restricted Three-Body Problem (CR3BP) STTs are computed by propagating the STT Equations of Motion (EOMs). In each condition, these propagated STTs are used to map GMM components to the desired final time. The mapping in 2BP dynamics, J_2 dynamics, and CR3BP dynamics in straight forward. Whereas, combining SDS with the GMM-STT propagation is more complex.

To utilise the SDS dynamics with this GMM-STT uncertainty propagation method, the initial state is converted from osculating to mean elements to ensure that the propagation is performed in the mean element space. Once the $\delta\boldsymbol{m}$ and $\boldsymbol{P}$ are mapped to the desired time, the short-period variations are added to $\delta\boldsymbol{m}$ to achieve the osculating state mean. Figure 3.4 summarises the propagation process. The initially offset mean of the GMM component is mapped with the mean dynamics STT, then offset using the short-period analytical equations to get the final osculating GMM mean. This is similar to the description in Figure 2.2, except for the mapping of the component mean to the final time using STTs.

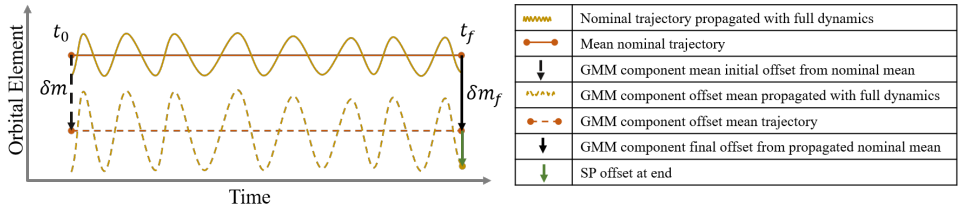

Figure 3.4: The final $\delta\boldsymbol{m}_f$ added to the nominal final state gives the final averaged GMM component mean. To improve accuracy, this final SDS mean state is converted to its corresponding osculating state to get the final GMM component mean [50].

The application of GMM-STT analytical or semi-analytical propagation in near-Earth space can be simply achieved by propagating these GMM components using the STT computed using the nominal trajectory. In cislunar environment, the process becomes more complex due to the chaotic nature of dynamics in that region. A way to capture the motion for GMM distributions further away from the nominal trajectory is to compute these STTs more locally around the GMM means of each GMM distribution. This GMM-STT semi-analytical process of propagation using

non-nominal STTs is demonstrated further in the following sections.

The second order STT sufficiently captures the nonlinearity in mapping for the short-duration or short-term conjunctions. Even for long-term conjunctions, second order STTs give statistically good results, but with lower associate uncertainties, possibly indicating a need for higher order STTs for accurate mapping. This will demonstrated in more detail in later chapters.

3.4 Uncertainty Propagation using Gaussian Mixture Models and State Transition Tensors

Previous sections in this chapter define GMMs, describe the splitting methods to achieve GMMs, and list the equations used to propagate the GMM components. In this section, examples from near-Earth and cislunar regions are generated to understand the capture of nonlinear behaviour in the propagated distribution through these splitting processes.

3.4.1 Near-Earth Case

First, a test case is introduced in near-Earth space using simple 2BP dynamics and the Horwood splitting method. The orbital elements at epoch are listed in Table 3.1 and the initial covariance is non-diagonal of the order of 100 m in position and 10 cm/s in velocity. This state and uncertainty is split into a GMM mixture using the suboptimal Horwood algorithm [39] described in the previous section. The means, weights, and standard deviation library generated for a 15 component split at the epoch are shown in Table 3.2.

Orbital Elements	a (km)	e	i (deg)	Ω (deg)	ω (deg)	M (deg)
	8000	0.15	60	0	0	0

Table 3.1: Orbital Elements at epoch for the near-Earth GMM-STT propagation test.

A thousand points chosen from the initial distribution are propagated numerically for seven orbit periods, approximately 14 hours, using 2BP solution flow from Eq. (2.2). Then, the 15 initial GMM means and covariances form the splitting process are propagated using Eq. (3.11) with 2BP

GMM Component (i)	σ_i	w_i	m_i
1	0.57143	2.1567e-06	-4
2	0.57143	4.4497e-05	-3.4286
3	0.57143	0.00064899	-2.8571
4	0.57143	0.0057422	-2.2857
5	0.57143	0.031346	-1.7143
6	0.57143	0.10533	-1.1429
7	0.57143	0.21799	-0.57143
8	0.57143	0.27779	0
9	0.57143	0.21799	0.57143
10	0.57143	0.10533	1.1429
11	0.57143	0.031346	1.7143
12	0.57143	0.0057422	2.2857
13	0.57143	0.00064899	2.8571
14	0.57143	4.4497e-05	3.4286
15	0.57143	2.1567e-06	4

Table 3.2: Univariate split library for near-Earth test case.

STTs from Eq. (2.46) calculated about the nominal trajectory. These numerically propagated points and analytically propagated means and covariances are plotted in Figure 3.5.

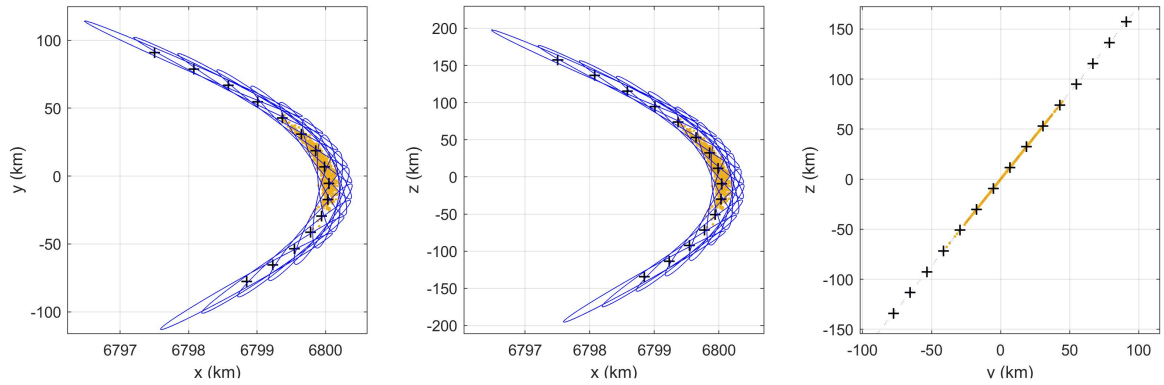

Figure 3.5: GMM-STT propagated example. Here, the 1000 yellow dots represent the MC propagated points, the black plus symbols represent the propagated GMM component means and the blue ellipses represent the propagated component covariances.

It is clear that the means and covariances fully capture the distribution in an expected manner, where the nonlinearity of the distribution is captured by the propagated GMM components. The Horwood algorithm gives a nice coverage to the distributions. The propagated covariances will be compared to compute the probability of collision and tested for statistical accuracy in later chapters. In addition to the 2BP dynamics, cases will also be presented with J_2 secular dynamics

and the SDS.

3.4.2 Cislunar Case

In the cislunar test case, it is important to test the different splitting directions to ensure the validity of the nonlinearity parameter from Vittaldev et al. [81]. In addition to this, an interesting observation was that the STT calculated using the nominal trajectory did not account for the nonlinear growth in the dynamics. The reason for this is likely the chaotic dynamical environment in cislunar space. To circumvent this issue, the STTs are computed at the means associated with each GMM for the highest level of accuracy. In this subsection, a test case is presented where different directions of GMM splitting are tested for accurate capture of the nonlinear evolution, and a comparison is shown between the GMMs propagated with the nominal STT and the GMMs propagated with the non-nominal STTs calculated with the individual GMM mean trajectories.

The state at epoch is shown in Table 3.3 and a diagonal covariance is chosen to be 315 m in position and 3.15 mm/s in velocity. The initial distribution is split into an 11 component GMM using the univariate library from Huber et al. [40], with the standard deviation, weights, and means shown in Table 3.4.

State [nd]	x	y	z	$\dot{x}$	$\dot{y}$	$\dot{z}$
	0.9874	-4.9076E-05	0.0085907	0.049661	1.60214	0.015030

Table 3.3: State at epoch for cislunar GMM-STT propagation test.

To perform the split, the nonlinearity parameter from Eq. (3.7) is computed for all the chosen test directions previously defined. Table 3.5 shows the computed ϕ values in each of these directions. The smallest and largest ϕ values are considered to see the worst and best capture of the nonlinear behaviour with the GMM-STT propagation method, respectively. In this test case, The direction that should perform the worst is $\boldsymbol{v}_h$, and the direction that should best capture the nonlinear evolution of the distribution is $\boldsymbol{r}_v$.

GMM Component (i)	σ_i	w_i	m_i
1	0.30151	0.0061199	-2.6705
2	0.30151	0.02545	-2.0287
3	0.30151	0.066272	-1.4777
4	0.30151	0.12422	-0.96797
5	0.30151	0.17792	-0.47937
6	0.30151	0.20003	0
7	0.30151	0.17792	0.47937
8	0.30151	0.12422	0.96797
9	0.30151	0.066272	1.4777
10	0.30151	0.02545	2.0287
11	0.30151	0.0061199	2.6705

Table 3.4: Univariate split library for cislunar test case.

GMM split direction	Nonlinearity Parameter (ϕ)
$\boldsymbol{r}_x$	0.00010766
$\boldsymbol{r}_y$	7.6303E-05
$\boldsymbol{r}_z$	0.00017149
$\boldsymbol{v}_x$	1.1993E-06
$\boldsymbol{v}_y$	1.634E-06
$\boldsymbol{v}_z$	2.5246E-05
$\boldsymbol{r}_r$	0.00011823
$\boldsymbol{r}_v$	0.00027509
$\boldsymbol{r}_h$	2.1979E-05
$\boldsymbol{r}_t$	0.00021521
$\boldsymbol{v}_r$	1.5672E-06
$\boldsymbol{v}_v$	2.8021E-05
$\boldsymbol{v}_h$	3.5355E-08
$\boldsymbol{v}_t$	2.6484E-05
$\boldsymbol{eig}_0$	1.1993E-06
$\boldsymbol{eig}_T$	2.2609E-05

Table 3.5: Directions and nonlinear parameter values from Eq. (3.7).

500 trajectories from this initial distribution are propagated numerically for approximately ten days using CR3BP dynamics from Eq. (2.37). Then, 11 GMM components from the initial GMM split are propagated for the same time period using Eq. (3.11) with CR3BP STTs from the previous section calculated at individual GMM means. The multi-directional split is first implemented using the smallest nonlinearity parameter ϕ direction ($\boldsymbol{v}_h$) indicating the smallest direction of nonlinearity growth. This is purely to see an inaccurate capture of the nonlinear behaviour of the propagated distribution. Figure 3.6 shows the GMM components propagated using STTs mapped over the numerically propagated points.

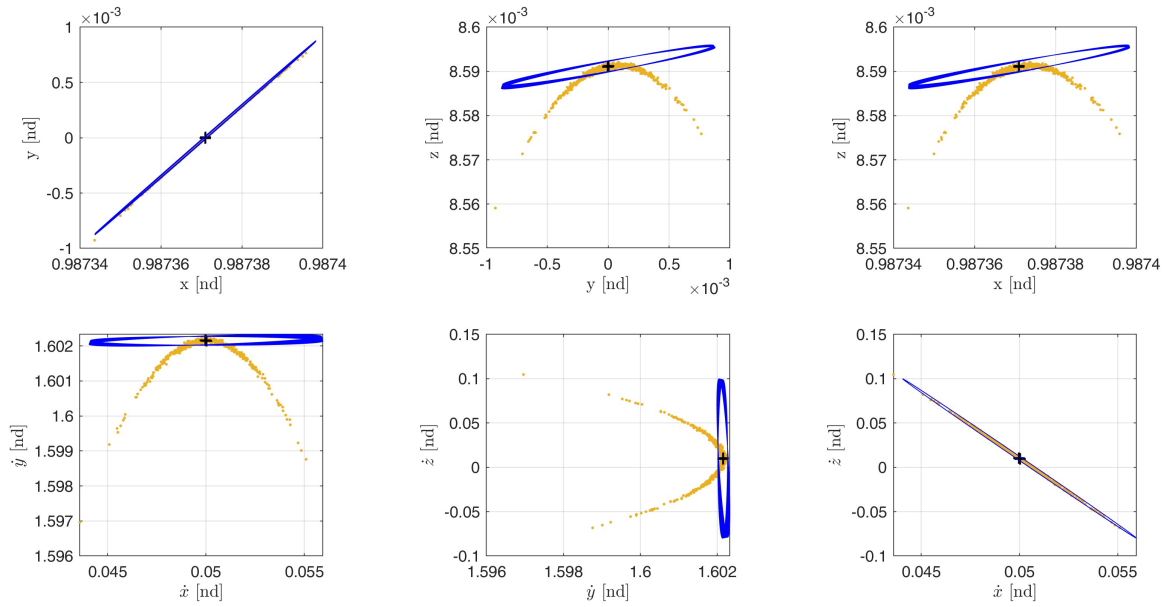

Figure 3.6: GMM-STT propagated example in cislunar space using the lowest ϕ or the smallest nonlinearity growth direction mapped with the non-nominal STTs. Here, the 500 yellow dots represent the MC propagated points, the black plus symbols represent the propagated GMM component means and the blue ellipses represent the propagated component covariances.

For the second test, the same split is performed in the direction associated with the largest ϕ ($\boldsymbol{r}_v$) indicating the capture of the most nonlinearity growth. Figure 3.7 plots the new split propagated components overlapping the numerically propagated distribution. Figure 3.7 demonstrated a much better visual capture of the six-dimensional distribution after propagation. This shows that using the largest direction of nonlinearity from the test directions does provide a better estimate of the final nonlinear distribution.

Now that a direction of split is established, a similar run is performed with 11 GMM components split along the highest direction of nonlinearity mapped using the STT propagated about the nominal trajectory. Figure 3.8 plots the new split propagated components overlapping the numerically propagated distribution. It is clear that the nominal STT is not enough to capture the nonlinear evolution of the distribution in the cislunar environment.

In summary, in cislunar GMM-STT propagation it is important to use the STTs computed about the non-nominal individual GMM means to fully capture the evolution of the distribution.

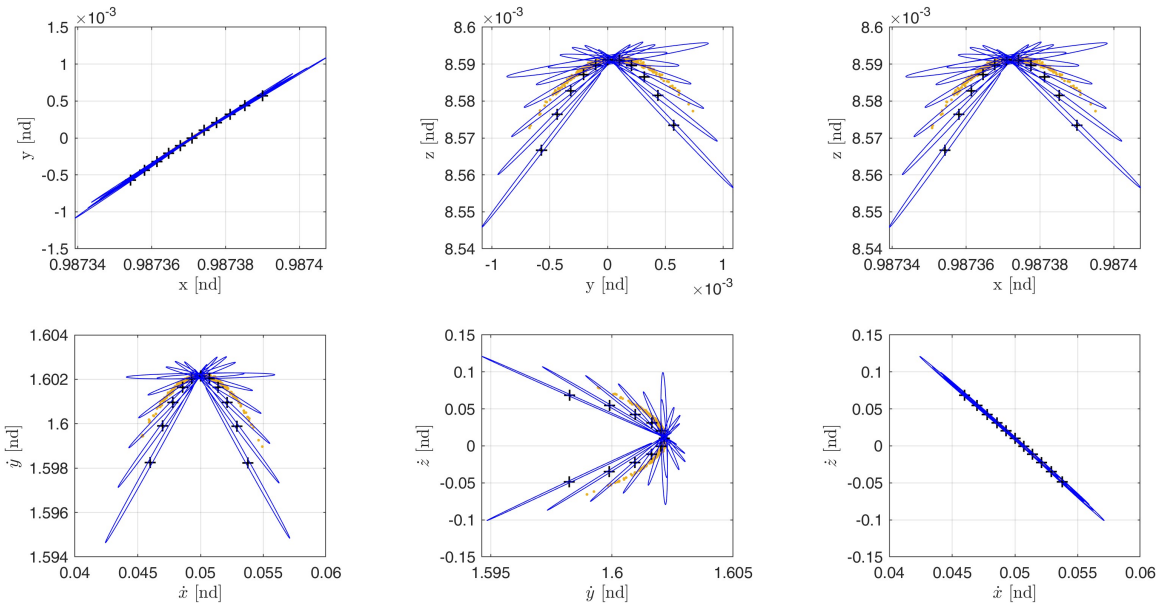

Figure 3.7: GMM-STT propagated example in cislunar space using the highest ϕ or the largest nonlinearity growth direction mapped with the non-nominal STTs. Here, the 500 yellow dots represent the MC propagated points, the black plus symbols represent the propagated GMM component means and the blue ellipses represent the propagated component covariances.

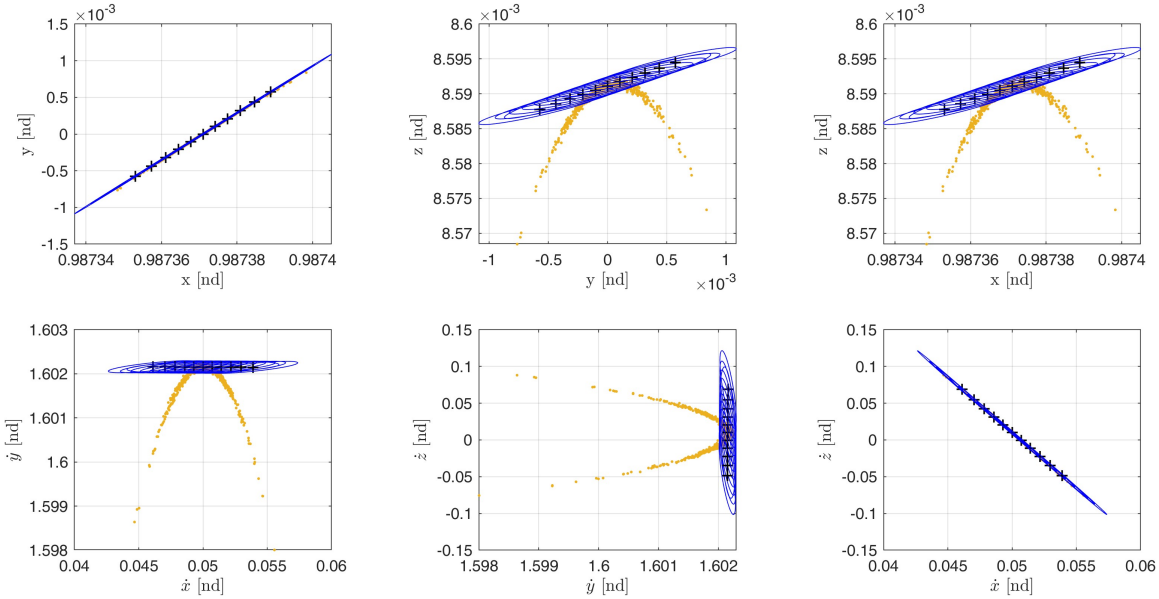

Figure 3.8: GMM-STT propagated example in cislunar space using the highest ϕ or the largest nonlinearity growth direction mapped with the nominal STTs. Here, the 500 yellow dots represent the MC propagated points, the black plus symbols represent the propagated GMM component means and the blue ellipses represent the propagated component covariances.

In addition to this, it is crucial that the GMM split is performed along the largest direction of nonlinearity growth which can be established using nonlinearity parameters, such as the one developed by Vittaldev et al. [81].

3.5 Conclusion

This chapter describes a method that combines Gaussian Mixture Models (GMMs) and State Transition Tensors (STTs) to map a distribution to the final time, and accurately capture the nonlinear behaviour of the uncertainty evolution. An initial distribution is split into a Gaussian mixture using a suboptimal algorithm in the equinoctial frame in the near-Earth space and a multi-directional splitting method in the Cartesian frame in the cislunar space. These GMM components from the split are mapped using analytically computed STTs when using the Two-Body dynamics and J_2 Secular dynamics; or using semi-analytically computed STTs when using the Simplified Dynamics System or the Circular Restricted Three-Body Problem.

The final GMM components, when combined, represent a nonlinear final distribution which captures the boundaries of the numerically propagated population. This GMM-STT method is key to a fast and accurate alternate method to propagate an initial distribution. Multiple methods of splitting a GMM are described for near-Earth and cislunar space. Lastly, two test cases are presented in near-Earth and cislunar regions to demonstrate the GMM-STT mapping method and the capture of the final distribution.

Chapter 4

Probability of Collision

An important application of accurate uncertainty tracking is in the field of conjunction assessment. Historically, Monte Carlo numerical methods are used to compute the probability of collision between two objects by propagating a point cloud from the initial uncertainty of each object. With a large number of trajectories these methods [4] provide accurate probability of collision results, but are computationally expensive. To surpass this expense, analytical formulas are developed that use the means and covariances of the two object distributions at the time of closest approach to approximate the probability of collision [32, 5, 19, 18, 21, 28]. It is important to consider the assumptions associated with each of these methods to understand applicability.

In this chapter, a hybrid conjunction analysis method is developed with the semi-analytical uncertainty propagation using Gaussian Mixture Models (GMMs) and State Transition Tensors (STTs) that allows the use of propagated state and uncertainty information in a combination with an analytical probability of collision formula. This Chapter first defines the necessity of accurate uncertainty propagation method in conjunction analysis. It then categorizes collisions into two types: short-term and long-term conjunctions, depending on the conjunction duration. After this, two main probability of collision methods are defined: 1) the numerical Monte Carlo analysis that is considered to be the baseline truth and 2) the hybrid conjunction analysis method.

4.1 Uncertainty Propagation in Conjunction Analysis

As described in previous chapters, uncertainty becomes non-Gaussian when propagated with nonlinear orbit dynamics. In two dimensions this looks like an evolution from an ellipse to a crescent shape. Even if the nominal trajectories of two objects do not cross, an overlap in this propagated uncertainty can lead to a conjunction (Figure 4.1). Due to this uncertainty distortion, it becomes important to incorporate the non-Gaussian nature of the propagated uncertainty in conjunction assessment methods for accurate probability of collision calculations.

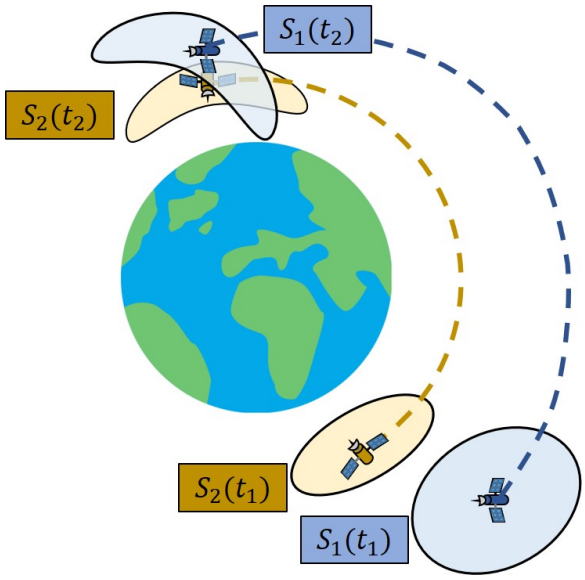

Figure 4.1: Uncertainty overlap at a future time. The initially Gaussian uncertainty distributions loose their Gaussianity when propagated using nonlinear dynamics. A conjunction can occur when there is an overlap in object uncertainties. [50]

Numerical Monte Carlo methods propagate a large number of points from the initial uncertainty of the two objects using the system dynamics to capture the nonlinear evolution of the distribution in time. With enough points, the non-Gaussian behaviour of the distribution is captured accurately. The points from the two objects are compared at their respective times of closest approach to achieve a probability of collision. More and more points are needed as the propagation time increases or the overlap between the two objects reduces to accurately capture the probability of collision.

To achieve the same nonlinear capture using analytical conjunction methods, it is important to consider the loss of accuracy that comes with some analytical propagation methods. Several analytical and semi-analytical methods can be used to propagate the object distributions, achieve a time of closest approach, and compute the probability [58]. Many of these methods assume a Gaussian distribution associated with the objects in conjunction at the time of closest approach, which can lead to oversimplification of the conjunction analysis problem due to the nonlinear behaviour in orbital dynamics and non-Gaussian evolution of uncertainty. To avoid this, it is essential to capture the nonlinear evolution of uncertainties accurately and to evaluate the conjunction considering non-Gaussian distributions at the time of closest approach. One such method is discussed in the later sections.

4.2 Conjunction Models

There are two encounter models that are defined based on the duration of the conjunction. The short-term conjunctions are of short or instantaneous duration, such that the objects pass each other quickly, and assume rectilinear motion for the two objects at the point of closest approach [5, 32, 58]. The long-term conjunctions span over longer conjunction times, meaning that the object uncertainty distributions need to be compared over longer time periods [18, 21, 10, 58]. This makes the long-term conjunction problem much more complex.

4.2.1 Short-Term Conjunctions

A conjunction is considered to be short-term if the encounter time is very short, ranging from a fraction of a second to a few seconds [58]. This means that the relative velocity between the two objects is very large, such that the motion near the conjunction time is considered as uniform rectilinear motion [5]. The position uncertainty is considered to be constant due to the short duration and the velocity uncertainty to be negligible due to a comparatively high relative velocity. These simplifications allow the use of simple analytical conjunction analysis techniques [32, 5, 22, 21, 3] in evaluating short-term conjunctions.

Figure 4.2 shows an example of a short-term conjunction. Figure 4.2a shows trajectories of the two objects that cross at a singular point. Figure 4.2b shows the relative distance between the two objects in conjunction with respect to the orbit periods of object 1. This relative distance plot is over 3 days, with the nominal time of closest approach between the trajectories at 1.5 days from epoch. The plot shows a quick dip in the relative distance of the two objects. The short-duration pass means that the velocity uncertainty is insignificant compared to the position uncertainty [22] in the small encounter time. In addition to this, the uncertainty ellipsoid can be considered constant over time [22].

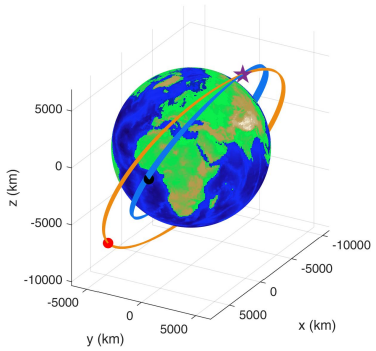

(a) An example of a short-term conjunction. Orbits, initial locations, and nominal conjunction points of the two objects. [50]

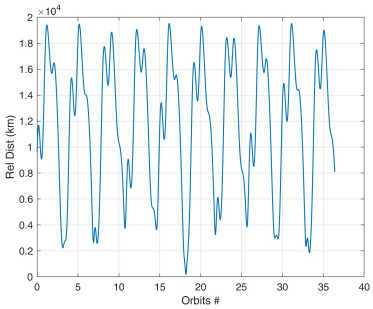

(b) Relative distance between objects in conjunction.

Figure 4.2: Short-term conjunction example. (a): The blue ellipse is the trajectory of object 1, whereas the yellow is the trajectory of object 2. The black point is the initial location of object 1, and the red is the initial location of object 2. The violet star is the nominal conjunction point of the two objects. (b): Relative distance between the two objects over 3 days.

In such short-term encounters, simplified techniques are used to evaluate the conjunction. Typically, a two-dimensional integral in the encounter plane is used to calculate the collision probability [32, 5]. In this encounter plane, the axes are oriented along the relative position and the relative velocity directions.

4.2.2 Long-Term Conjunctions

When it comes to long-term encounters, a lot of the assumptions made for short-term encounters are no longer valid, adding complexity to the problem. For instance, velocity uncertainty can no longer be ignored and the full state uncertainty ellipsoid can no longer be assumed constant over the conjunction period.

An example of such a long-term conjunction is shown in Figure 4.3. Figure 4.3a shows the trajectories of the two objects and Figure 4.3b shows the distance between the two objects in conjunction with respect to the orbit periods of the primary over 3 days. Same as the short-term example in Figure 4.2, the nominal time of closest approach is 1.5 days after the epoch. The two objects stay in the vicinity of each other for a long time with a slow dip in the relative distance. The red dashed line in Figure 4.3b shows an arbitrary threshold, below which the objects are considered to be in a conjunction. This threshold is specified based on the uncertainty associated with the object states.

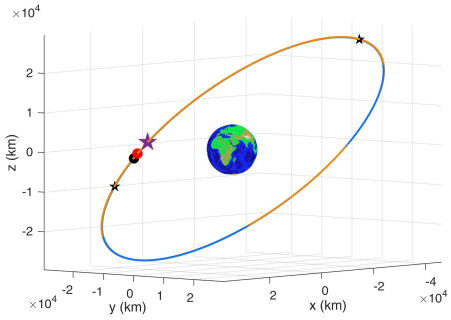

(a) Long-term conjunction example. [51]

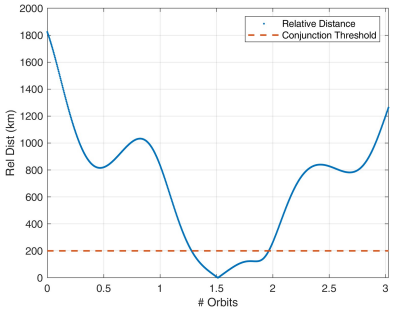

(b) Relative distance between objects in conjunction. [51]

Figure 4.3: Long-term conjunction example. (a): Orbits, initial locations, and nominal conjunction points of the two objects. The blue ellipse is the trajectory of object 1, whereas the yellow is the trajectory of object 2. The black point is the initial location of object 1, and the red is the initial location of object 2. The violet star is the nominal conjunction point of the two objects. The black stars show the beginning and end of the conjunction. (b): Relative distance between the two objects over 3 days. Red dashed line represents an arbitrary line of the distance below which the objects are considered to be in a conjunction.

In a long-term conjunction, the period of time in close proximity is non-instantaneous. This

means that we need an additional integration for the change in the six-dimensional uncertainty ellipsoid over the period of conjunction.

4.3 Monte Carlo Method

The Monte Carlo analysis use a point cloud generated from the object uncertainty and propagates this forward to capture the final uncertainty distribution. In collision analysis applications, the uncertainty of the two objects in conjunction are propagated forward using numerical propagation and compared to get the probability of collision [2]. With enough points, usually a significant amount of points, the Monte Carlo analysis gives a true solution to compare other probability of collision results against [26].

First, the actual time of closest approach is calculated between the chosen pair of trajectories in the Monte Carlo evaluation. The actual time of closest approach is computed using a simple stepping method [1] in case of the short-term encounters because the pass is instantaneous, leading to a drastic drop in the relative position. The time step is simply:

$$\Delta t = \frac{\Delta \boldsymbol{r}.\Delta \boldsymbol{v}}{|\Delta \boldsymbol{v}|^2} \tag{4.1}$$

where $\Delta \boldsymbol{r}$ and $\Delta \boldsymbol{v}$ are the relative position and velocity vectors between the two objects, respectively. The method is initiated with the nominal time of closest approach as the initial guess. Each step brings the objects closer and reduces the step size. Once the step size reduces below a small chosen threshold, the time is considered to have converged. This is the final time of closest approach.

In case of long-term conjunctions, the stepping method fails because the drop in the relative distance near the nominal time of closest approach is gradual. The MATLAB 'event' function is used to find a global minima for the objects in these cases because the objects are in the proximity for a longer period of time. This is also initiated using the nominal time of closest approach as the starting point and moving away from the nominal time until the event function triggers a stopping

point at a minima, which denotes the actual time of closest approach.

Once the actual time of closest approach is computed in either conjunction case, the distance of closest approach (DCA) is compared to the combined radii of the two objects ($R = r_1 + r_2$). If DCA is less than the combined radii, it's considered to be a collision. This set of points is discarded and a new set of points is chosen for the same evaluation. The number of points that collide compared to the total number of points in the analysis (ten million) gives the total probability of collision:

$$P_{c,MC} = \frac{\#\text{ Sample conjunctions where DCA } < R}{\#\text{ Total conjunctions tested}} \tag{4.2}$$

Figure 4.4 summarises the Monte Carlo method of probability of collision calculations.

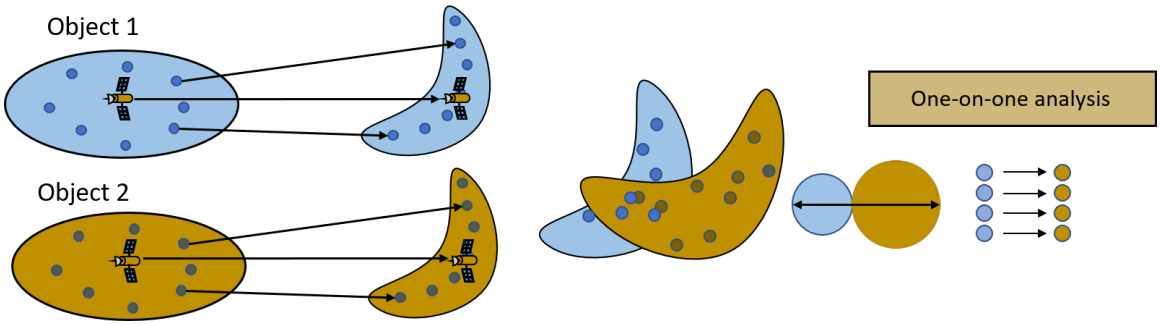

Figure 4.4: In the Monte Carlo method, (from left to right) points from initial distribution of each object are propagated to the final time, where their distance of closest approach informs the collision probability in a one-on-one analysis.

Adding confidence bounds around the Monte Carlo probability of collision allow a comparison with other probability of collision methods. These bounds are computed using the normal approximation of the binomial confidence interval [54].

$$\text{CI} = z\sqrt{\frac{P_{c,MC}(1 - P_{c,MC})}{y}} \tag{4.3}$$

Here, the z-value for a 95% confidence is 1.96. y is ten million, which denotes the total number of Monte Carlo points in the analysis. If the probability of collision from the analytical methods being tested falls within a confidence interval (CI) of the Monte Carlo probability of

collision ($P_{c,MC}$), it is considered to be accurate with a 95% confidence.

$$P_{c,\text{bounds}} = P_{c,MC} \pm \text{CI} \tag{4.4}$$

4.3.1 Test Case for Monte Carlo with the Simplified Dynamical System

The computational time with this Monte Carlo analysis increases with an increase in modeled dynamics fidelity. When full J_2 and Solar Radiation Pressure (SRP) perturbations are added, the full dynamics Monte Carlo takes a long time to run. To ease the computational burden, a similar Monte Carlo approach is developed using the Simplified Dynamical System (SDS). To use the SDS for propagation in the Monte Carlo analysis, the osculating object states are converted to mean states at epoch for propagation using mean dynamics and converted back to the osculating state at the desired times for accurate distance of closest approach calculations. Work from Park and Scheeres [65] shows that the SDS propagation is statistically accurate relative to the full dynamics Monte Carlo. This reduces the computational burden tremendously, by outputting an accurate truth probability of collision without the need to use the full system dynamics. The full dynamics and the SDS dynamics Monte Carlo results are compared in a test cases to verify accuracy.

The orbital elements for the test case are shown in Table 4.1. The nominal time of closest approach is at 1.5 days from epoch. The initial uncertainty associated with the two objects are of the order of 100 m in position and 10 cm/s in velocity. The Monte Carlo method is run with 10 million points to evaluate the probability of collision using: 1) full dynamics with J_2 and SRP and 2) SDS with J_2 and SRP.

Table 4.1: Orbital Elements for the SDS Monte Carlo example.

Orbital Elements	a (km)	e	i (deg)	Ω (deg)	ω (deg)	M (deg)
Object 1	8000	0.15	60	0	0	0
Object 2	9843.3	0.241038	61.8685	-10.9875	55.5795	-87.5619

Table 4.2 shows the results from the two Monte Carlo runs. The collision probability from the two runs with the full dynamics and the SDS dynamics differ by $4.40E-06$. The SDS Monte Carlo

collision probability does fit within the 97^{th} percentile normal approximation confidence bounds of the full dynamics Monte Carlo result. The Monte Carlo run with the SDS demonstrates a significant computational burden reduction when compared to the full dynamics model.

Table 4.2: Probability of collision for the Monte Carlo method with different dynamics.

Dynamics	Probability of collision	Runtime (s)
Full Dynamics	4.67E-05	457302 ($\approx$ 5.3 days)
SDS	5.11E-05	18888 ($\approx$ 5.25 hours)

This result signifies that the Monte Carlo probability of collision evaluated using SDS can be used as baseline truth to compare probability computed using analytical methods that use the SDS. It also justifies the use of the SDS in combination with the GMM-STT propagation model.

4.4 The Hybrid Method of Uncertainty Propagation and Conjunction Analysis

In this section, a hybrid method of uncertainty propagation is combined with analytical conjunction analysis methods to achieve a fast and accurate solution for collision probability. The semi-analytical uncertainty propagation is performed by splitting the initial uncertainty of the objects in conjunction into a GMM and propagating individual GMM components using higher order STTs. These previously defined mathematical concepts are combined with chosen dynamical models: two-body dynamics, J_2 secular dynamics, a Simplified Dynamical System (SDS), or a Circular Restricted Three-Body Problem (CR3BP) dynamics in case of cislunar space. In near-Earth applications, the SDS provides an efficient and accurate dynamical system that uses non-Keplerian motion under perturbations due to J_2 gravity field harmonics and Solar Radiation Pressure (SRP) for propagation. This is achieved through propagation with averaged dynamics and addition of analytical short-period variations at the final time for accuracy (Simplified Dynamical System + short-period variations = SDS+SP dynamics). This combination of the GMM-STT model with the SDS dynamics allows for real-world conjunction analysis applications of this method in near-Earth space. The propagated GMM components associated with the non-Gaussian uncertainties of the

two objects are compared to each other using analytical conjunction assessment formulas.

Most analytical equations of probability of collision evaluation assume a Gaussian distribution for both objects in conjunction. In this work, the individual GMMs propagated using the STTs stay nearly-Gaussian after propagation to the actual times of closest approach. This means that the individual GMM components of the two objects can even be compared using probability of collision methods that assume Gaussian distributions for the objects in conjunction. In this hybrid approach, an all-on-all analysis is used to compute the probability of collision between each individual GMM components associated with two objects in conjunction at their respective actual times of closest approach using propagation with SDS-STTs. Then, these individual probabilities of collision are combined using a double weighted sum using the GMM component weights associated with the GMM components in comparison.

The typical approach to compare the individual GMM components depends on the duration of the conjunction. In case of short-term conjunctions, there are several simple analytical probability of collision solutions that can be used to compare Gaussian distributions [58]. With enough GMM components, each small distribution of a GMM components can be treated as a Gaussian distribution, allowing easy comparisons with such analytical probability of collision techniques. On the other hand, in case of the long-term conjunctions, the objects stay in the vicinity of each other for longer duration, meaning that simplified short-term conjunction techniques can not be implemented with ease. Very few analytical techniques for evaluation of long-term collision probability exist [58]. Coppola's triple integral formula [21] that takes into account both position and velocity uncertainty is primarily used in long-term conjunction analysis. A key find in this research is that these small GMM components, when compared individually for long-term probability of collision calculations can be evaluated using simplified short-term conjunction formulas when these components are "small enough". This is because each individual interaction behaves as a short-term conjunction.

Figure 4.5 summarises the hybrid method of uncertainty propagation and conjunction analysis for near-Earth and cislunar applications. In near-Earth applications, the initial cartesian

distribution of the two objects is converted to the Equinoctial frame [12] to allow a split using a suboptimal algorithm defined in Chapter 3. The individual components of this distribution are propagated using the STTs computed with the chosen dynamics, as described in Chapter 2. The final distribution is converted back to the cartesian frame for a comparison to evaluate the probability of collision. In cislunar space, the initial distribution in the cartesian frame is split into a GMM (Chapter 3) which is propagated using the CR3BP STTs (Chapter 2). The final cartesian GMM components are compared to evaluate the probability of collision.

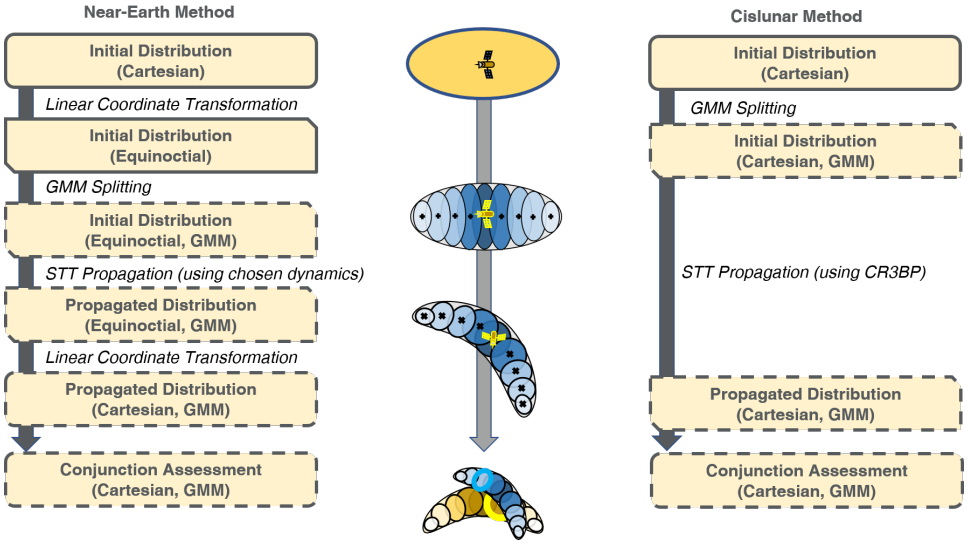

Figure 4.5: Uncertainty propagation and conjunction assessment toolkit process summary.

Coppola's triple integral [21] is a general approach that applies to all types of conjunctions. Over the next sections, the general probability of collision from Coppola [21] is described, followed by the modifications from DeMars [26] that add GMMs into this generalised formula. At the end of this section, certain assumptions are made and applied to this formula to achieve the simplified formula used in the hybrid collision probability analysis.

4.4.1 Coppola's Conjunction Analysis Formula

Coppola proposed a probability of collision formula that uses the state and velocity uncertainty of an object to evaluate the conjunction without restricting the relative motion of the two

objects in conjunction [21]. The formula assumes Gaussian uncertainty for the duration of the conjunction. This method of conjunction analysis tracks the influx of the relative position probability distribution into a hardball of the combined radii of the two objects fixed at one of the objects in conjunction [26, 21]. With simplification Coppola reduces a 12-dimensional integral into a 2-dimensional integral of a sphere and a 1-dimensional integral of time. In application of the hybrid method, the probability of collision at epoch is assumed to be zero, because the chosen nominal conjunction time is chosen in the future. Coppola [21] uses the mean cartesian relative state of the two objects ($\boldsymbol{\mu}$) and the combined covariance associated with them ($\boldsymbol{P} = \boldsymbol{P}_1 + \boldsymbol{P}_2$) to defined the probability of collision.

The six dimensional cartesian covariance can be split into four 3x3 parts:

$$\boldsymbol{P} = \begin{bmatrix} \boldsymbol{A} & \boldsymbol{B}^T \\ \boldsymbol{B} & \boldsymbol{C} \end{bmatrix} \tag{4.5}$$

Here, $\boldsymbol{A}$ and $\boldsymbol{C}$ are symmetric positive-definite 3x3 matrices. The mean relative state can be split into mean relative position (3x1) and mean relative velocity (3x1):

$$\boldsymbol{\mu} = \begin{bmatrix} \boldsymbol{\mu}_r & \boldsymbol{\mu}_v \end{bmatrix}^T \tag{4.6}$$

Using this relative state and combined covariances, Coppola [21] defines the probability of collision as follows:

$$P_I = \int_{t_0}^{t_0+T} \int_0^{2\pi} \int_{-\frac{\pi}{2}}^{\frac{\pi}{2}} \mathcal{N}_3(\boldsymbol{r}; \boldsymbol{\mu}_r(t), \boldsymbol{A}(t)) \nu(\hat{\boldsymbol{r}}, t) R^2 \cos\theta \; d\theta \; d\phi \; dt \tag{4.7}$$

Here, T is the duration of conjunction, $\boldsymbol{r}$ is the relative position between the two objects in conjunction, $\boldsymbol{\mu}_r(t)$ is the mean relative position, $\boldsymbol{A}(t)$ is the combined covariance of the relative position, and $\nu(\hat{\boldsymbol{r}}, t)$ is a parameter introduced to account for combined velocity uncertainty. (θ,ϕ) are spherical parameters parameterizing $\hat{\boldsymbol{r}}$. $\nu(\hat{\boldsymbol{r}}, t)$ is defined as follows:

$$\nu(\hat{\boldsymbol{r}},t) = \frac{\sigma(\hat{\boldsymbol{r}},t)}{\sqrt{2\pi}} H(\tilde{\nu}) \tag{4.8a}$$

$$H(\tilde{\nu}) = e^{-\tilde{\nu}^2} - \sqrt{\pi}\tilde{\nu}(1 - \mathrm{erf}(\tilde{\nu})) \tag{4.8b}$$

$$\tilde{\nu} = \frac{\nu_0(\hat{\boldsymbol{r}},t)}{\sqrt{2}\sigma(\hat{\boldsymbol{r}},t)} \tag{4.8c}$$

$$\nu_0(\hat{\boldsymbol{r}},t) = \hat{\boldsymbol{r}}^T[\boldsymbol{\mu}_v + \boldsymbol{B}\boldsymbol{A}^{-1}(R\hat{\boldsymbol{r}} - \boldsymbol{\mu}_r)] \tag{4.8d}$$

Here, $\sigma(\hat{\boldsymbol{r}},t)$ is the standard deviation of the relative velocity uncertainty in the $\hat{\boldsymbol{r}}$ direction:

$$\sigma^2 = \hat{\boldsymbol{r}}^T(\boldsymbol{C} - \boldsymbol{B}\boldsymbol{A}^{-1}\boldsymbol{B}^T)\hat{\boldsymbol{r}} \tag{4.9}$$

DeMars et al. [26] applies this conjunction formula from Eq. (4.7) to a GMM distribution such that the cumulative probability of collision can be computed using a double weighted sum of the individual GMM component interactions. The next section shows the evolution of these equations.

4.4.2 Combining General Conjunction Formula with GMMs

DeMars et al. [26] achieves this combination of collision probability equations with GMMs by replacing the combined object pdf from Eq. (4.7) with the weighted sum pdf of the form of Eq. (3.2).

The relative state of the second object at a time, t, ($\boldsymbol{x}_{b,t}$) relative to the first object ($\boldsymbol{x}_{a,t}$) can be represented as:

$$\boldsymbol{x}_{b,t} = \boldsymbol{x}_{a,t} + \boldsymbol{x}_t \tag{4.10}$$

The pdf of the relative state ($\boldsymbol{x}_t$) can be given by marginalization over $\boldsymbol{x}_{a,t}$:

$$p(\boldsymbol{x}_t) = \int p(\boldsymbol{x}_{a,t}, \boldsymbol{x}_{b,t}) d\boldsymbol{x}_{a,t} = \int p(\boldsymbol{x}_{a,t}, \boldsymbol{x}_{a,t} + \boldsymbol{x}_t) d\boldsymbol{x}_{a,t} \tag{4.11}$$

Each object pdf is then split into GMMs with L_a and L_b components respectively. $w_a^{(i)}(t)$ and $w_b^{(j)}(t)$ are the weights associated with the i^{th} and j^{th} components of objects 1 and 2 respectively. Assuming independent states, the product of the pdfs of the two objects can be defined by substituting the individual pdfs with the weighted sums of GMM components of each object:

$$p(\boldsymbol{x}_{a,t})p(\boldsymbol{x}_{b,t}) = \sum_{i=1}^{L_a}\sum_{j=1}^{L_b} w_a^{(i)}(t)w_b^{(j)}(t)p_g(\boldsymbol{x}_{a,t};\boldsymbol{m}_{a,t}^{(i)},\boldsymbol{P}_{a,t}^{(i)})p_g(\boldsymbol{x}_{a,t}+\boldsymbol{x}_t;\boldsymbol{m}_{b,t}^{(j)},\boldsymbol{P}_{b,t}^{(j)}) \tag{4.12}$$

Following the steps from Coppola [21], the pdf from Eq. (4.7) can be substituted with a combined pdf (left hand of Eq. (4.12)). The double weighted sum (right side of Eq. (4.12)) can be introduced in place of the combined pdfs to achieve the new DeMars et al. [26] equation that combines GMM distributions with Coppola's probability of collision formula, as shown in Eq. (4.13).

$$p(\boldsymbol{x}_t) = \sum_{i=1}^{L_a}\sum_{j=1}^{L_b} w_a^{(i)}(t)w_b^{(j)}(t)p_g(\boldsymbol{x}_t;\boldsymbol{\mu}_t^{(ij)},\boldsymbol{P}_t^{(ij)}) \tag{4.13a}$$

$$P_c = \int_{t_0}^{t_0+T} R^2 \sum_{i=1}^{L_a}\sum_{j=1}^{L_b} w_a^{(i)}(t)w_b^{(j)}(t) \int_0^{2\pi}\int_{-\frac{\pi}{2}}^{\frac{\pi}{2}} \mathcal{N}_3(\boldsymbol{r};\boldsymbol{\mu}_r^{(ij)}(t),\boldsymbol{A}^{(ij)}(t))\nu(\hat{\boldsymbol{r}},t)\cos\theta \; d\theta \; d\phi \; dt \tag{4.13b}$$

DeMars et al. [26] proposes using trapezoidal integration to perform the time integration and methods like the Newton Cotes quadrature [68] to perform the spherical integration. This reduces computational expense, while ensuring user defined accuracy. A major drawback to this approach is that the time step in the trapezoidal integration is arbitrary, too small of a time step to increase accuracy leads to an increase in computational expense. Lebedev's grid [56] can be used to perform the spherical integration for the probability of collision evaluation.

Due to the computational expense associated with the tedious triple integration, the formula from Eq. (4.13) is investigated in more depth. As previously mentioned, when using the GMM-STT uncertainty propagation method for long-term conjunction evaluation, individual GMM component interactions start behaving like short-term interactions when there are enough GMM components

split from the initial distribution. Next section shows the reduction of this general conjunction formula defined in Eq. (4.13) to a short-term GMM component interaction formula.

4.4.3 New Approach to Improve Speed

The individual GMM component interactions are now introduced with a closer inspection within the weighted sum. Firstly, in the case of short-term conjunctions, each individual interaction uses nearly-Gaussian uncertainties at the times of closest approach to evaluate the probability of collision. This means that the probability of collision within the weighted sum for these short-term conjunctions can be simplified using assumptions including: rectilinear motion of the two objects at the time of closest approach, no velocity uncertainty due to the short duration of the pass, and a constant uncertainty ellipsoid over the short duration of the conjunction. These simplifications are applied in this section to achieve a simple conjunction formula.

Secondly, in the case of long-term conjunctions, as the number of components increase in the weighted sums of the two objects, the component covariance reduces in size, which results in a decrease in the time of interaction between each component. This means that short-term conjunction assumptions can be applied within the weighted sum for such short-duration component interactions in the long-term conjunction assessment. Therefore, same as in the case of short-term conjunctions, the probability of collision equations can be simplified further. These identical reductions output a single simplified conjunction formula that applied to both, short-term and long-term conjunctions.

In the hybrid method developed in this section, the GMM component weights are computed at the epoch and remain constant throughout the propagation. This means that the probability of collision equation from Eq. (4.13) can be rewritten as follows:

$$P_c = \sum_{i=1}^{L_a} \sum_{j=1}^{L_b} w_a^{(i)} w_b^{(j)} \int_{t_0}^{t_0+T} \int_0^{2\pi} \int_{-\frac{\pi}{2}}^{\frac{\pi}{2}} \mathcal{N}_3(\boldsymbol{r}; \boldsymbol{\mu}_r^{(ij)}(t), \boldsymbol{A}^{(ij)}(t)) \nu(\hat{\boldsymbol{r}}, t)\ R^2\ \cos\theta\ d\theta\ d\phi\ dt \qquad (4.14)$$

Each interaction inside the weighted double sum is the same as the triple integral from

Coppola's general probability of collision equation from Eq. (4.7). Previous works from Foster [32] and Alfriend et al. [5] show the reduction of such a general triple integral formula to a short-term conjunction formula with the following simplifying assumptions: no velocity uncertainty, a short encounter time, and that time integrates out. Applying these assumptions, Coppola [21] reduces the general conjunction formula from Eq. (4.7) to a short-term conjunction formula. This transformed short-term formula is a double integral over a circle of the combined radii projected onto an encounter plane ($[\hat{\boldsymbol{i}};\hat{\boldsymbol{j}};\hat{\boldsymbol{k}}]$):

$$\boldsymbol{i} = \frac{\boldsymbol{\rho}_0}{\rho_0},\ \boldsymbol{j} = \frac{\boldsymbol{v}_R}{\mathrm{v}_R},\ \boldsymbol{k} = \boldsymbol{i} \times \boldsymbol{j} \tag{4.15a}$$

$$P_c = \iint_{|\zeta|<R} \mathcal{N}_2(\boldsymbol{\zeta}, \boldsymbol{\mu}_{\zeta_0}, \boldsymbol{P}_C) d\boldsymbol{\zeta} \tag{4.15b}$$

Using the nominal time of closest approach, relative distance ($\boldsymbol{\rho}_0$) and relative velocity ($\boldsymbol{v}_R$). Here, $\boldsymbol{P}_C$ is the combined covariance of the relative position projected onto this plane. This probability of collision formula can be re-written as follows:

$$P_{c,ij} = \frac{1}{2\pi\sqrt{|P^*|}} \int_{-R}^{R} \int_{-\sqrt{R^2-x^2}}^{\sqrt{R^2-x^2}} \exp\left(-A^*\right) dz\, dx \tag{4.16}$$

The relative state and combined covariance are transformed into the encounter frame and the probability of collision is computed using the relative position of the two objects at the nominal time of closest approach ($\boldsymbol{s}_0$) and the actual time of closest approach ($\boldsymbol{s}$).

$$\boldsymbol{s} = x\boldsymbol{i} + z\boldsymbol{k},\ \boldsymbol{s}_0 = x_0\boldsymbol{i} + z_0\boldsymbol{k} \tag{4.17a}$$

$$A^* = (\boldsymbol{s} - \boldsymbol{s}_0)^T P^{*-1} (\boldsymbol{s} - \boldsymbol{s}_0)/2 \tag{4.17b}$$

$$P_{c,ij} = \frac{1}{2\pi\sqrt{|P^*|}} \int_{-R}^{R} \int_{-\sqrt{R^2-x^2}}^{\sqrt{R^2-x^2}} \exp\left(-A^*\right) dz\, dx \tag{4.17c}$$

Same as before, the cumulative probability of collision is calculated using the double weighted sum of these individual GMM component interactions. Eq. (4.14) can be re-written using the shortened probability of collision formula as shown in Eq. (4.18).

$$P_c = \sum_{i=1}^{L_a}\sum_{j=1}^{L_b} w_a^{(i)} w_b^{(j)} P_{c,ij}$$
$$= \frac{1}{2\pi\sqrt{|P^*|}} \sum_{i=1}^{L_a}\sum_{j=1}^{L_b} w_a^{(i)} w_b^{(j)} \int_{-R}^{R}\int_{-\sqrt{R^2-x^2}}^{\sqrt{R^2-x^2}} \exp\left(-A^{*,ij}\right) dz\, dx \tag{4.18}$$

Note that this is a simplified version of Eq. (4.14). This is a very powerful result that allows short-term analytical equations to be utilised in both short-term and long-term conjunction cases. This makes a significant difference in reducing computation cost, for both these conjunction types, still giving accurate probability of collision results due to the use of the semi-analytical uncertainty propagation approach with GMMs. Figure 4.6 shows a component wise comparison of the two propagated distributions.

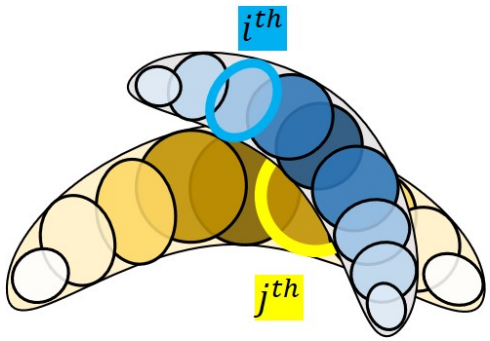

Figure 4.6: The total probability of collision in the GMM-STT method is an all-on-all analysis between propagated GMM components of objects 1 (blue) and 2 (yellow). $P_{c,ij}$ is a comparison between i^{th} and j^{th} GMM components from objects 1 and 2 respectively. The highlighted GMM components are the ones being compared for the probability of collision calculations.[50]

4.5 Conclusion

This chapter describes the importance of accurate nonlinear uncertainty propagation in conjunction analysis methods. After this, two conjunction models are defined based on their duration: short-term and long-term conjunctions. A Monte Carlo method is defined that can generate an accurate collision probability with a significant number of points from the initial distributions propagated numerically. As an alternate to this expensive method, a hybrid method is presented that

propagates the uncertainty fast and accurately to achieve the final distribution using a combination of Gaussian Mixture Models (GMMs) and State Transition Tensors (STTs). The propagated components from the GMMs are compared in an all-on-all analysis to achieve the probability of collision of the system. Test cases are presented in the next chapter to validate this hybrid method of collision probability computations.

Chapter 5

Conjunction Assessment Test Cases

To evaluate the performance of the proposed hybrid uncertainty propagation and conjunction analysis method from chapter 4, a variety of conjunction cases are tested using different dynamics models. A combination of Gaussian Mixture Models (GMMs) and State Transition Tensors (STTs) is used to propagate the object distributions. In an all-on-all analysis, the initial distribution of each object is split into GMMs, which are compared to achieve the collision probability. In each comparison, the GMM components are propagated to their respective actual times of closest approach using STTs computed with chosen dynamics. Then, all GMM component comparisons are combined using a double weighted sum. The probability of collision from this hybrid method is compared against the Monte Carlo probability to test the statistical accuracy.

In this chapter, test cases are presented in near-Earth space using two-body (2BP) dynamics, J_2 secular dynamics, and a Simplified Dynamical System (SDS) that adds perturbations from full J_2 and Solar Radiation Pressure (SRP). A repeating conjunction study is presented using the 2BP dynamics to understand the evolution of the GMM-STT propagation method over time. Short-term and long-term conjunction cases are tested in the SDS dynamics subsection. In the end, test cases are presented for different orbits in cislunar space using the Circular Restricted Three-Body Problem (CR3BP). For each of these test cases, the initial conditions to test are found by propagating a chosen trajectory to the chosen nominal time of closest approach (TCA), shifting the position and velocity by a chosen amount, and back-propagating to achieve the second orbital element set at epoch. The propagation is performed using the chosen dynamics model.

5.1 Near-Earth Region

5.1.1 Two-Body Dynamics Test Case

The orbital elements for both objects at epoch are shown in Table 5.1. Fig. 5.1a shows the two orbits and the initial locations of each object.

Orbital Elements	a (km)	e	i (deg)	Ω (deg)	ω (deg)	M (deg)
Object 1	8000	0.15	60	0	0	0
Object 2	6801.6	0.013155	0.37645	90	-0.5016	262.32

Table 5.1: Orbital Elements for the 2BP example.

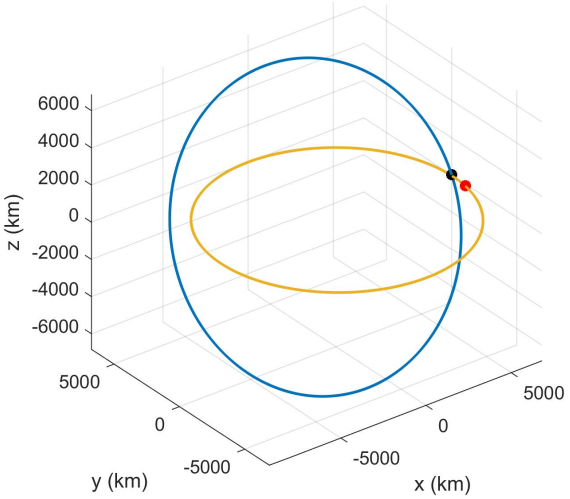

(a) Orbits and initial locations of the two objects in the 2BP example.

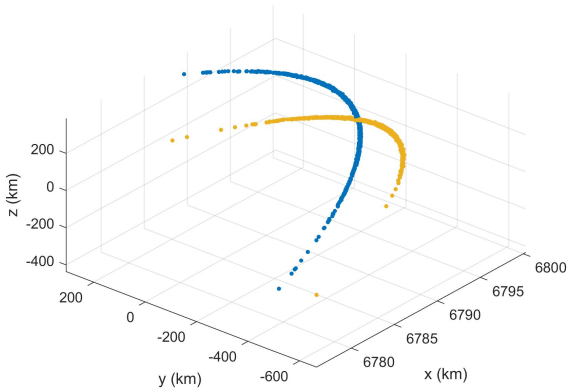

(b) Uncertainty distribution of the two objects in the 2BP example.

Figure 5.1: Subfig. (a) Orbits and initial locations of the two objects in the 2BP example. The blue ellipse is the trajectory of object 1, whereas the yellow is the trajectory of object 2. The black point is the initial location of object 1 and the red is the initial location of object 2. Subfig. (b) Uncertainty distribution of the two objects in the 2BP example at their nominal TCA. The blue and yellow points represent the Monte Carlo propagated points from the initial uncertainties of objects 1 and 2 respectively.

A large non-diagonal initial covariance is chosen for both objects of the order of 100 m in position and 10 cm/s in velocity. The nominal TCA is 1.5 days from epoch. The probability of collision is computed using Monte Carlo and hybrid methods, and compared to understand the accuracy of the latter. Fig. 5.1b shows the Monte Carlo uncertainty distribution of the two objects

at the nominal conjunction time.

As mentioned previously, to compute the GMM-STT method probability, first the GMM components are computed using the Horwood algorithm. The means and covariances of each of these components are propagated using the 2BP STTs (Eq. 2.46).

Fig. 5.2 shows that as the number of components increases, the GMM-STT probability of collision converges with the Monte Carlo truth value CI bounds at about 100 GMM components.

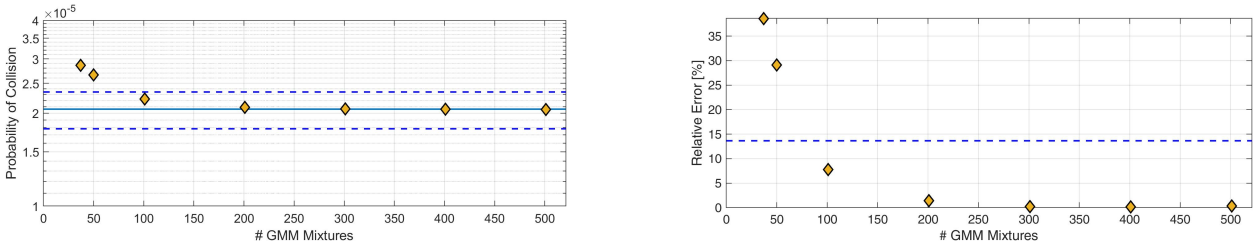

(a) Probability of collision comparison.

(b) Relative error plot.

Figure 5.2: Subfig. (a) shows the GMM-STT collision probability vs Monte Carlo results for the 2BP example, whereas Subfig. (b) shows the relative error in the GMM-STT results wrt the Monte Carlo ones. The solid blue line represents the Monte Carlo probability of collision, the dashed blue lines represent the 95% confidence bounds, and the yellow diamonds represent the GMM-STT probability of collisions at different number of GMM mixture components.

5.1.2 2BP Repeating Conjunction Study

In this special case, the unique condition of 2BP repeating conjunctions is observed. The main purpose of this experiment is to understand the change in the GMM-STT method probability of collision solution convergence to the Monte Carlo solution as the propagation time increases. This can only be observed in the 2BP scenario, because the objects return to the same configuration periodically. Three cases presented here increase sequentially in propagation time to demonstrate the change in distribution, probability of collision, and hybrid method convergence. The first case is at the 5th conjunction from the epoch time, the second case is at the 10th, and the third case is at the 20th conjunction from epoch. A large non-diagonal initial covariance is chosen of the order of 100 m in position and 10 cm/s in velocity.

Table 5.2 shows the orbital element set chosen to perform this study and Fig. 5.3 shows the two nominal orbits and object initial locations.

Orbital Elements	a (km)	e	i (deg)	Ω (deg)	ω (deg)	M (deg)
Object 1	8000	0.15	60	0	0	0
Object 2	9033.94588	0.01838	94.37746	0	0	30

Table 5.2: Orbital Elements for the Repeating Conjunctions example.

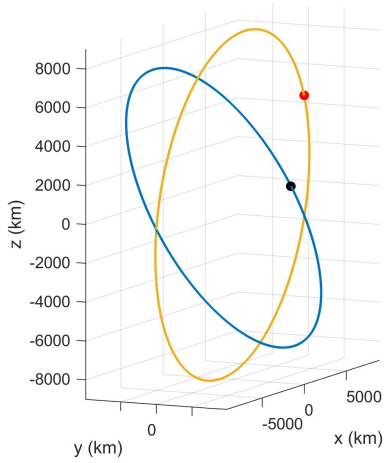

Figure 5.3: Orbits and initial locations of the two objects in the Repeating Conjunction example. The blue ellipse is the trajectory of object 1, whereas the yellow is the trajectory of object 2. The black point is the initial location of object 1 and the red is the initial location of object 2.

Same as before, the collision probability is computed using the Monte Carlo method and the hybrid method. Fig. 5.4a, 5.4b, and 5.4c show the distributions for the repeating conjunctions at the nominal times of closest approach associated with the different cases. The distribution spreads out further towards its ends as the propagation time increases, leading to fewer points intersecting.

The collision probability from the hybrid method converges with that from the Monte Carlo analysis. Fig. 5.4d, 5.4e, and 5.4f show the respective hybrid method convergence. The probability of collision from the Monte Carlo method decreases in value with an increase in propagation time because fewer points are in the vicinity of each other for probability of collision computations. The probability of collision from the GMM-STT method takes a sequentially larger number of mixture components to converge with the Monte Carlo probability of collision. This increase is because

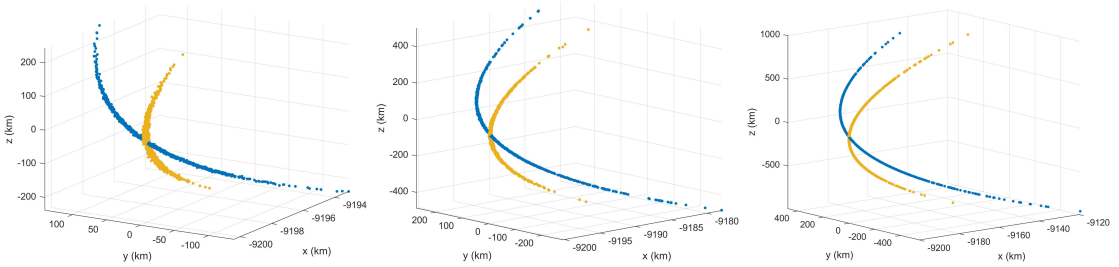

(a) Case 1 uncertainty distribution.

(b) Case 2 uncertainty distribution.

(c) Case 3 uncertainty distribution.

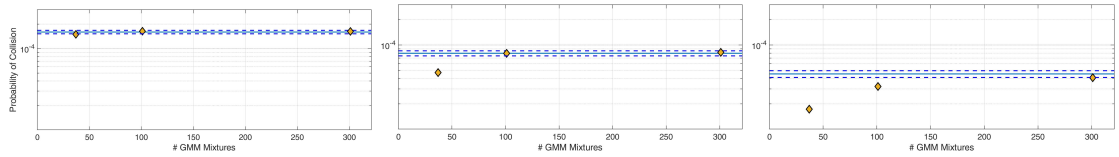

(d) Case 1 GMM-STT-Pc vs MC-Pc.

(e) Case 2 GMM-STT-Pc vs MC-Pc.

(f) Case 3 GMM-STT-Pc vs MC-Pc.

Figure 5.4: Subfig. (a), (b), and (c) show the uncertainty distribution in the Repeating Conjunction example. The blue and yellow points represent the Monte Carlo propagated points from the initial uncertainties of objects 1 and 2 respectively.
Subfig. (d), (e), and (f) show the GMM-STT collision probability vs Monte Carlo probability for the Repeating Conjunction example. The solid blue line represents the Monte Carlo probability of collision, the dashed blue lines represent the 95% confidence bounds, and the yellow diamonds represent the GMM-STT probability of collisions at different numbers of Gaussian mixture components.

longer propagation time means that more (and smaller) initial distribution mixture components will be needed to accurately capture the propagation nonlinearity. Also, as the propagation time increases, the STT calculations about the nominal trajectory lose accuracy.

5.1.3 2BP + J_2 Secular Dynamics Test Case

In this example, the secular effects due to Earth J_2 are considered in addition to the 2BP dynamics to propagate the states in the Monte Carlo analysis, and to compute the STTs. Given the solution flow, the new STT from Eq. 2.47 is used in the hybrid method. The epoch states for the objects in this example are shown in Table 5.3. Fig. 5.5a shows the nominal propagated orbits and initial locations of the two objects.

Orbital Elements	a (km)	e	i (deg)	Ω (deg)	ω (deg)	M (deg)
Object 1	8000	0.15	60	0	0	0
Object 2	6881.49141	0.254197	54.34536	8.76088	-110.10574	22.92517

Table 5.3: Orbital Elements for the J_2 Secular example.

A large non-diagonal initial covariance is chosen for both objects of the order of 100 m in position and 10 cm/s in velocity. The nominal TCA is 1.5 days from epoch. Fig. 5.5b shows the uncertainty distribution of these two objects at the nominal TCA. Same as in the 2BP dynamics example, the Horwood GMM method is used to split the individual uncertainties into smaller distributions. Again, the collision probability is calculated using the Monte Carlo and the hybrid methods.

Figure 5.6 shows that the cumulative hybrid probability of collision converges with the Monte Carlo probability of collision with 100 components.

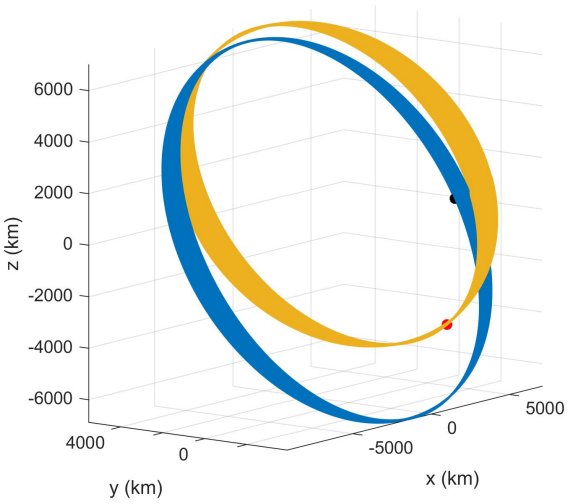

(a) Orbits and initial locations of the two objects in the J_2 Secular example.

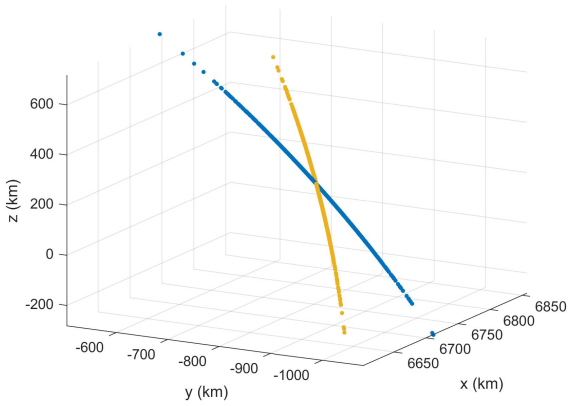

(b) Uncertainty distribution of the two objects in the J_2 Secular example.

Figure 5.5: Subfig. (a) Orbits and initial locations of the two objects in the J_2 Secular example. The blue ellipse is the trajectory of object 1, whereas the yellow is the trajectory of object 2. The black point is the initial location of object 1 and the red is the initial location of object 2. Subfig. (b) Uncertainty distribution of the two objects in the J_2 Secular example at the nominal TCA. The blue and yellow points represent the Monte Carlo propagated points from the initial uncertainties of objects 1 and 2, respectively.

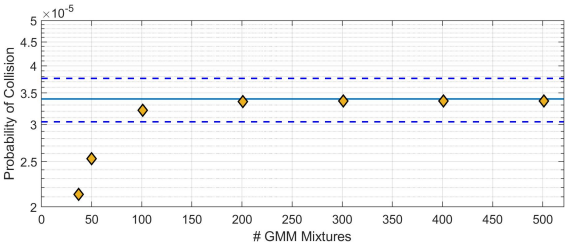

(a) Probability of collision comparison.

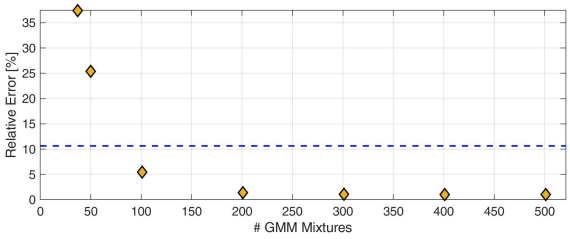

(b) Relative error plot.

Figure 5.6: Subfig. (a) shows the GMM-STT collision probability vs Monte Carlo probability for the J_2 Secular example, whereas Subfig. (b) shows the relative error between the two. The solid blue line represents the Monte Carlo probability of collision, the dashed blue lines represent the 95% confidence bounds, and the yellow diamonds represent the GMM-STT probability of collisions at different number of GMM mixture components.

5.1.4 Simplified Dynamical System Test Case

This Section presents two case studies, one each for a short-term conjunction and a long-term conjunction. For each of these test cases, the initial conditions to test are found by propagating

a chosen trajectory to the chosen nominal TCA, shifting the position and velocity by a chosen amount, and back-propagating to achieve the second orbital element set at epoch. The propagation is performed using the SDS dynamics. The initial covariance choice is critical because it drives the number of GMM components necessary for accurate capture of the propagated uncertainty and probability of collision calculations.

The probability of collision is computed using: 1) the Monte Carlo method and 2) the hybrid method developed in chapter 4. The latter is compared to the Monte Carlo probability of collision with a 95% confidence interval.

5.1.4.1 Short-Term Encounter

Table 5.4 shows the initial conditions of the two objects in conjunction. A large non-diagonal initial covariance is chosen for both objects of the order of 100 m in position and 10 cm/s in velocity. The nominal TCA is 1.5 days from epoch. Figure 5.7a shows the epoch locations of the two objects, their trajectories, and their conjunction point. Figure 5.7b shows the Monte Carlo SDS dynamics propagated uncertainty of the two objects at the nominal TCA.

Table 5.4: Orbital Elements for the SDS example. [50]

Orbital Elements	a (km)	e	i (deg)	Ω (deg)	ω (deg)	M (deg)
Object 1	8000	0.15	60	0	0	0
Object 2	9843.3	0.241038	61.8685	-10.9875	55.5795	-87.5619

In the Monte Carlo conjunction analysis, the points are propagated numerically to evaluate the conjunction. In this test case, the Monte Carlo analysis is first performed using full dynamics with SRP and J_2 perturbations. Then, the same analysis is performed using the SDS dynamics with SRP and J_2 to confirm the use of the latter as a baseline truth. In the semi-analytical GMM-STT analysis, the initial distribution is split into Gaussian components that are propagated using SDS-STTs, as previously described.

Figure 5.8a shows the GMM-STT probability of collision compared to the two types of Monte Carlo probability of collision. The plot shows that: 1) The SDS Monte Carlo probability of collision

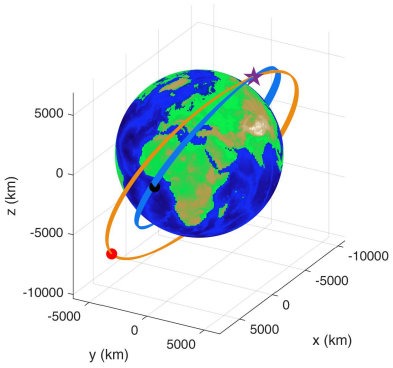

(a) Initial orbits.

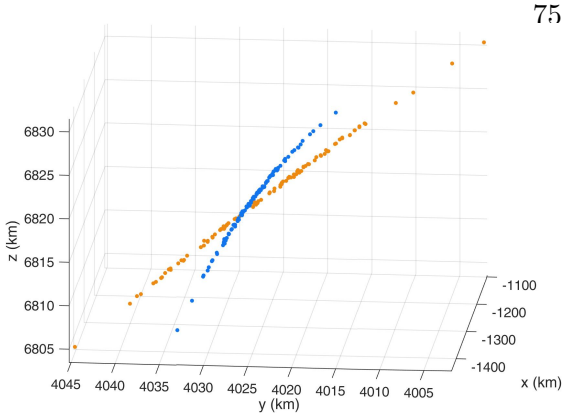

(b) Uncertainty distributions at the nominal TCA.

Figure 5.7: (a): Orbits, epoch locations, and the conjunction point of the two objects. Object 1 trajectory is represented in blue and object 2 trajectory is represented in yellow. The black point denotes the initial location of object 1, and the red point denotes that of object 2. The purple star is the conjunction point of the two objects. (b): Uncertainty distribution of the two objects. The blue and yellow points represent the Monte Carlo propagated points of objects 1 and 2 respectively. [50]

is within 95% of the full dynamics Monte Carlo solution for probability of collision, and 2) the GMM-STT probability of collision is also accurate to within the 95% of the full dynamics Monte Carlo probability of collision using more than about 100 components. Figure 5.8b shows the relative error of the GMM-STT probability of collision wrt the full dynamics Monte Carlo probability of collision. This implies that the GMM-STT semi-analytical method of probability of collision is accurate with a 95% confidence.

The short-term probability of collision results are computed using the University of Colorado Boulder Research Computing Summit Supercomputer (Intel Xeon E5-2680 v3 @2.50GHz 2 CPUs/node, 24 cores/node, 2133 MT/s, Dual Rank, x4 Data Width RDIMM, 4.84 GB/core). The runtimes for each previously listed method are listed in Table 5.5. It is clear from the above results that the GMM-STT method with 100 GMM components associated with each object achieve accuracy to within 95% of the Monte Carlo results with a speed of 1700 times faster than the full dynamics Monte Carlo analysis.

Note that due to the extreme difference in the runtimes between the full dynamics Monte

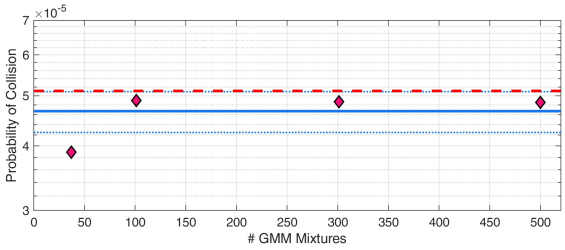

(a) Probability of collision comparison.

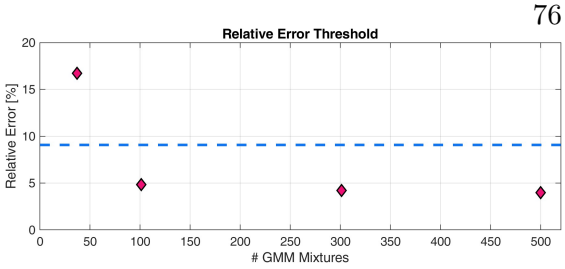

(b) Relative error plot.

Figure 5.8: Subfig. (a) shows the GMM-STT results and the SDS Monte Carlo results vs the full dynamics Monte Carlo probability of collision, whereas Subfig. (b) shows the relative error in the GMM-STT probability of collision wrt the full dynamics Monte Carlo probability of collision. The solid blue line shows the full dynamics Monte Carlo probability of collision, the dashed blue lines represent the 95% confidence bounds, the red dashed line represents the SDS Monte Carlo probability of collision, and the pink diamonds represent the GMM-STT probability of collisions at different numbers of GMM mixture components each. [50]

Table 5.5: Runtimes of different methods. [50]

Method	Runtime (s)
Full (non-simplified) Dynamics Monte Carlo	457302 ($\approx$ 5.3 days)
SDS dynamics Monte Carlo	18888 ($\approx$ 5.25 hours)
SDS 101 GMM-STT	266 ($\approx$ 4.43 minutes)

Carlo and the SDS dynamics Monte Carlo, along with the statistical agreement between the two, it is appropriate to use the SDS Monte Carlo results for verification of the GMM-STT method probability of collision.

5.1.4.2 Long-Term Encounter

Table 5.6 shows the orbital elements at epoch of the two objects in a long-term conjunction. Similar to the short-term conjunction example, the nominal TCA is 1.5 days from epoch and the uncertainty associated with the objects is non-diagonal with the order of 100 m in position and 10 cm/s in velocity.

Table 5.6: Orbital Elements for the example.

Orbital Elements	a (km)	e	i (deg)	Ω (deg)	ω (deg)	M (deg)
Object 1	42000	0.1	45	0	0	0
Object 2	42096.4927	0.0976	44.9276	-0.0070	-0.9984	3.0654

Figure 5.9a shows the nominal orbits of the two objects in conjunction. Figure 5.9b shows the relative orbits of the two objectives, along with the duration of the conjunction where the objects are within an arbitrary distance threshold. Figure 5.9c shows the relative distance between the two objects over time. The long time that the dip stays underneath the arbitrary distance threshold is significant to note, because in short-term conjunctions there is an instantaneous dip and rise in similar plots. Figure5.9d shows the uncertainty distributions of the two objects at the nominal TCA.

To forego the long computation time for the full dynamics Monte Carlo, and with the conclusion from the previous test case, the Monte Carlo calculations are only performed using the SDS dynamics in this test case. In addition to this, the GMM-STT probability of collision is computed using the same method as before. Figure 5.10a shows the comparison of the two probability of collision results, from the SDS Monte Carlo analysis and the GMM-STT method. Figure 5.10b show that even with a significantly large number of GMM components the probability of collision converges to a 25% error and does not decrease even with an increase in components.

To understand the reasoning behind this lack of convergence, the same test is run with lower covariance values of 45 m in position and 4.5 cm/s in velocity. Figures 5.11a and 5.11b show that with this lower uncertainty test, there is a convergence of the GMM-STT probability of collision results to within the desired 95% confidence.

This is an important result because it shows that the model functions well with lower uncertainty long-term conjunction cases. A potential issue could be the limitation of using 2^{nd} order STTs in the analysis. As the order of the STTs increases, so does the computation cost because the STTs are propagated to the desired time numerically. The same examples were tested with 3^{rd} order STTs. This output nearly identical results to the 2^{nd} order STT propagation results shown here. It is possible that to capture the higher uncertainty case, increasing the STT orders further can potentially lead to results with lower relative error.

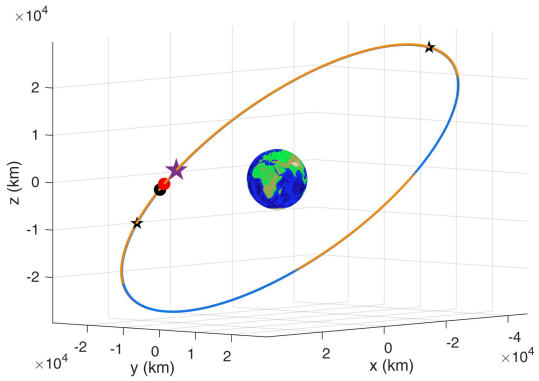

(a) Nominal trajectories of the two objects.

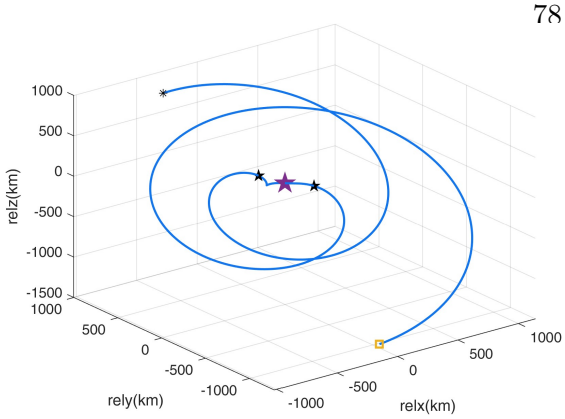

(b) Relative orbit.

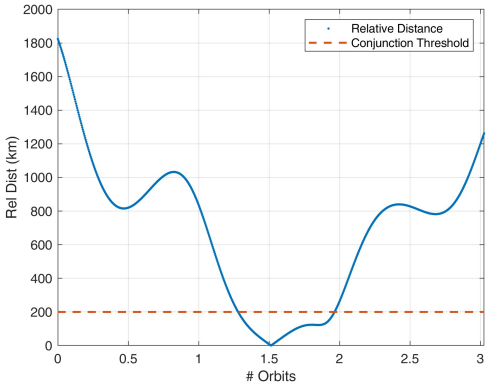

(c) Relative distance between the two objects.

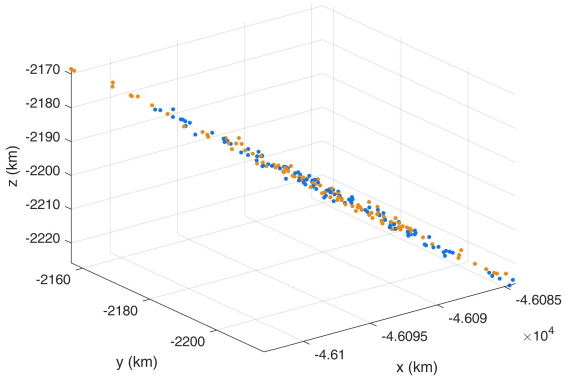

(d) Uncertainty distribution of the two objects at the nominal TCA.

Figure 5.9: (a): The blue ellipse and yellow ellipses are the trajectories of objects 1 and 2, respectively. The black and red points are the initial locations of object 1 and 2, respectively. The purple star is the nominal conjunction point of the two objects. The black stars show the beginning and end of the conjunction period. (b): The blue line represents the relative orbit. The purple star is the conjunction point of the two objects. The black stars show the duration of the conjunction period. (c) The blue line shows the relative distance between objects and the red dashed line shows an arbitrary threshold below which distance the objects are considered to be in a conjunction. (d) The blue and yellow points represent the Monte Carlo propagated points associated with objects 1 and 2, respectively, at the nominal TCA.

Using a personal ThinkPad laptop for computation, the approximate runtimes of different methods for the low uncertainty case are listed in Table 5.7. An additional test is run using the GMM-STT conjunction method with the long-term Coppola analytical formula using 101 GMM components associated with each object, to see a difference in computational time. The GMM-STT method run with both types of conjunction formulas (Coppola and reduced short-term formula)

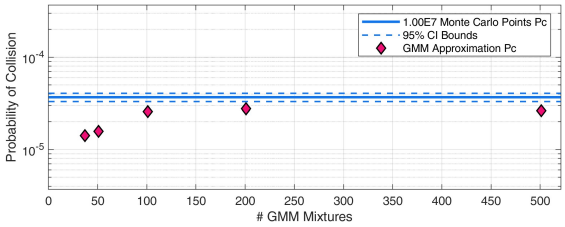

(a) GMM-STT-Pc vs MC-Pc.

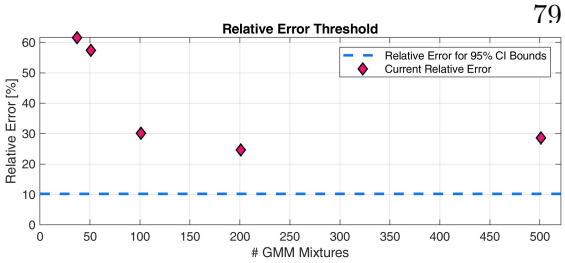

(b) Relative error.

Figure 5.10: High uncertainty case: (a) and (b): The solid blue line represents the SDS dynamics Monte Carlo probability of collision, the dashed blue lines represent the 95% confidence bounds, and the pink diamonds represent the semi-analytical probability of collisions at different numbers of GMM mixture components.

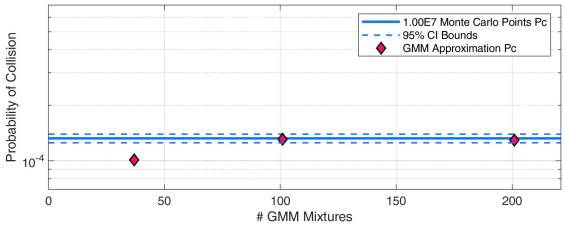

(a) GMM-STT-Pc vs MC-Pc.

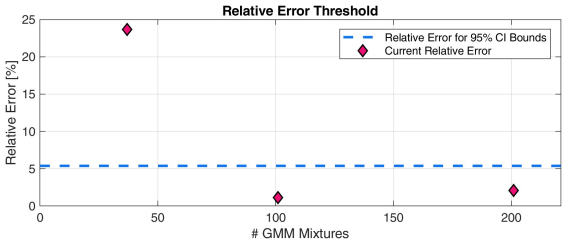

(b) Relative error.

Figure 5.11: Low uncertainty case: (a) and (b): The solid blue line represents the SDS dynamics Monte Carlo probability of collision, the dashed blue lines represent the 95% confidence bounds, and the pink diamonds represent the semi-analytical probability of collisions at different numbers of GMM mixture components.

output nearly the same results with a large difference in computation time. The semi-analytical uncertainty propagation approach run with the simplified short-term conjunction formula provides statistically accurate results ≈ 72 times faster than the SDS Monte Carlo method. This is, again, a significant improvement in computation expense.

Table 5.7: Runtimes of different methods. [50]

Method	Runtime
SDS dynamics Monte Carlo	$\approx$ 30 hours
SDS 101 GMM-STT with Coppola formula	$\approx$ 16 hours
SDS 101 GMM-STT with reduced formula	$\approx$ 25 minutes

5.2 Cislunar Region

A broad array of orbits and nominal TCAs are chosen to test the validity of the method. This section details the test cases and the respective results.

5.2.1 Lyapunov Orbit Test Case

An orbit is selected from a family of planar Lyapunov orbits near the L1 libration point in the Earth-Moon region. The epoch state of this orbit is propagated to approximately 6.86 days using CR3BP dynamics. The state at this final time is deviated to achieve a final state of the second object in conjunction. The final deviated state of object 2 is propagated back to the epoch to achieve the epoch state for object 2. The states of the two objects in this conjunction at epoch are listed in Table 5.8.

Orbital Elements	x	y	z	$\dot{x}$	$\dot{y}$	$\dot{z}$
Object 1	0.8971	0	0	0	-0.38874	0
Object 2	1.09352	-0.09259	0.01176	-0.17283	0.093228	-0.08352

Table 5.8: Orbital Elements for the first test case. Object 1 is in an L1 Lyapunov orbit.

An initial uncertainty of about 200 m in position and 2 $\frac{mm}{s}$ in velocity is assigned to both objects. Ten million points are randomly generated from this initial uncertainty distribution of each object and are propagated to compute the Monte Carlo probability of collision, as detailed in previous sections. Figure 5.12a shows the two orbit trajectories in the x-y plane over the 7 days period in the nondimensional rotating frame and Figure 5.12b shows the 3D paths of these objects. Figure 5.12c shows the numerically propagated object uncertainties at the nominal TCA. The uncertainty looks linear even after 7 days of propagation, which is much longer than the shorter periods within which the uncertainty becomes nonlinear in near-Earth cases [50].

Figure 5.13a shows the comparison of the semi-analytical uncertainty propagation probability of collision vs the Monte Carlo probability of collision and Figure 5.13b shows the relative error between the two. The results show that with an increase in GMM components, the results

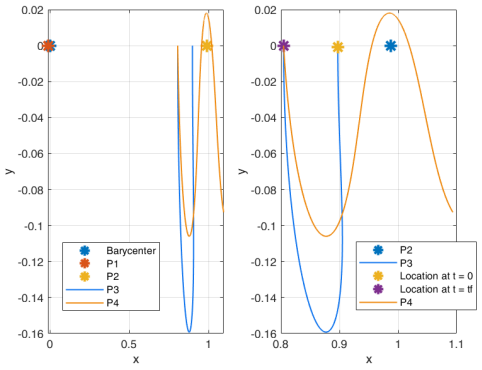

(a) Planar trajectories of the two objects in conjunction.

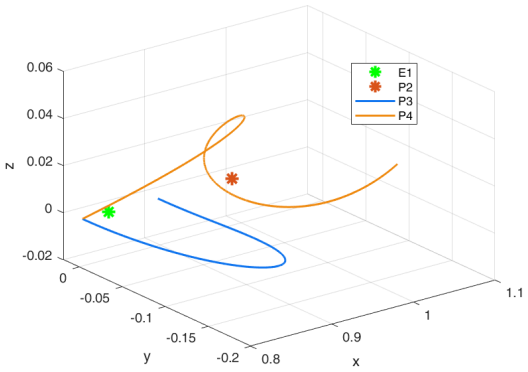

(b) 3D trajectories.

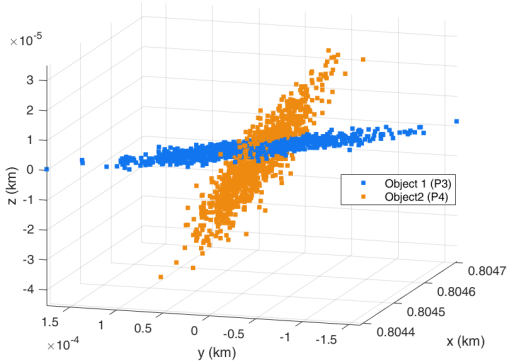

(c) Uncertainty of the two objects propagated to the nominal TCA.

Figure 5.12: Lyapunov test case: (a) and (b) show the trajectories on the two objects in conjunction in 2D and 3D views, respectively. The blue orbit is the Lyapunov orbit and the yellow trajectory represents the second object in conjunction. (c) shows the propagated uncertainty of the two objects at the nominal TCA.

get progressively close to the Monte Carlo probability of collision. As the uncertainty size and propagation time increases, so would the number of components needed for accurate probability of collision capture. In addition to being accurate, this semi-analytical method also shows a great improvement in computation time. The Monte Carlo probability of collision computation runs in 5.35 days, whereas the semi-analytical method calculated the probability of collision using 1, 15, and 31 components in 1 second, 118 seconds, and 503 seconds, respectively.

Method	RunTime
Monte Carlo	5.35 days
1 component GMM-STT method	1 second
15 component GMM-STT method	118 seconds
31 component GMM-STT method	503 seconds

Table 5.9: Time comparison of the semi-analytical uncertainty propagation method vs the Monte Carlo method for probability of collision computation.

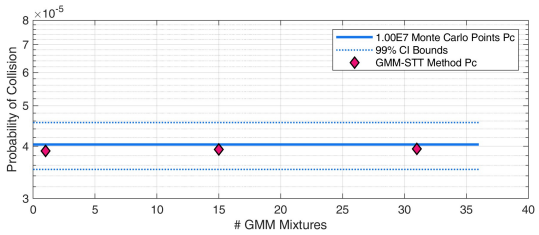

(a) Semi-analytical method probability of collision vs the Monte Carlo results.

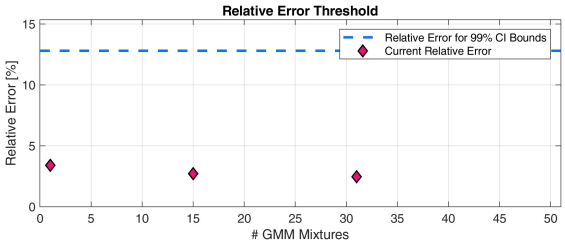

(b) Relative error between the semi-analytical method and the Monte Carlo results.

Figure 5.13: Lyapunov test case: These plots show the comparison of the probability of collision from the semi-analytical method developed in this paper to the Monte Carlo probability of collision. The solid blue line shows the Monte Carlo probability of collision, the dashed blue lines show the 99% error threshold, and the pink diamonds show the probability of collision computed using the semi-analytical uncertainty propagation.

5.2.2 Halo Orbit Test Case

5.2.2.1 Example 1

In addition to the Lyapunov orbit, an orbit was chosen from the L1 Halo family to test the method. Similar to the previous test case, the Halo orbit is propagated to the chosen nominal TCA of about 4.24 days (half its orbit period). The deviated final state is propagated back to epoch to get the initial states of both objects. The states at epoch are used to compute the probability of collision, using both the Monte Carlo method and the semi-analytical uncertainty propagation method. Table 5.10 shows the orbital elements at epoch for both objects.

Orbital Elements	x	y	z	$\dot{x}$	$\dot{y}$	$\dot{z}$
Object 1	0.89615	0	-0.1991	0	0.19234	0
Object 2	0.720946	0.094853	-0.20361	0.37510	0.362113	0.08011

Table 5.10: Orbital Elements for the first test case. Object 1 is in an L1 Halo orbit.

The initial covariance is set at 100 m in position and 1 $\frac{mm}{s}$ in velocity. Figure 5.14a shows the two nominal trajectories in consideration in a two dimensional view, whereas Figure 5.14b shows the same trajectories in a three dimensional view. Figure 5.14c shows the propagated uncertainties of the two objects at the nominal TCA.

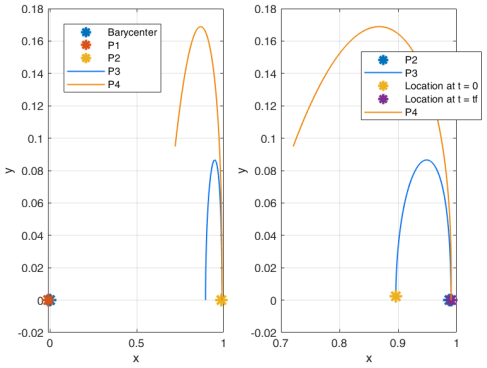

(a) Planar trajectories of the two objects in conjunction.

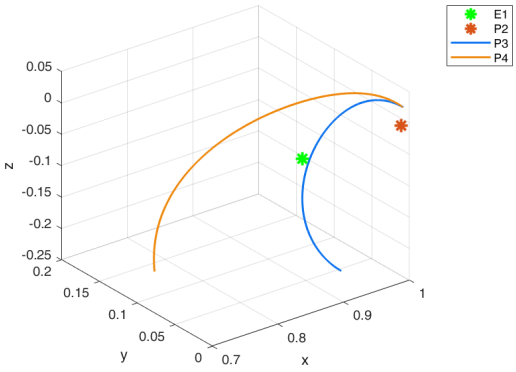

(b) 3D trajectories.

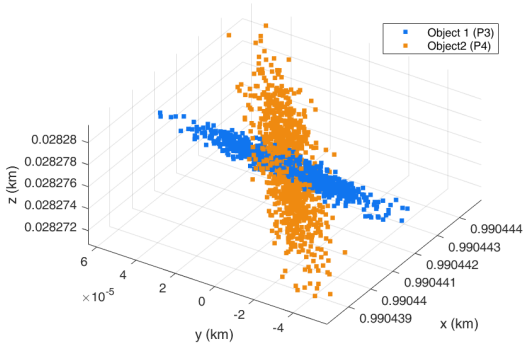

(c) Uncertainty of the two objects propagated to the nominal TCA.

Figure 5.14: Halo test case 1: (a) and (b) show the trajectories on the two objects in conjunction in 2D and 3D views, respectively. The blue and yellow trajectories refer to the Halo orbit and the secondary object orbit, respectively. (c) shows the propagated uncertainty of the two objects at the nominal TCA.

Figure 5.15a shows the results of the probability of collision computed using the semi-analytical uncertainty propagation in a comparison against that computed using the Monte Carlo Method. Figure 5.15b shows the relative error between the two probability of collisions.

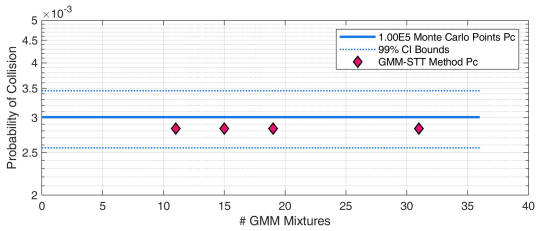

(a) Semi-analytical method probability of collision vs the Monte Carlo results.

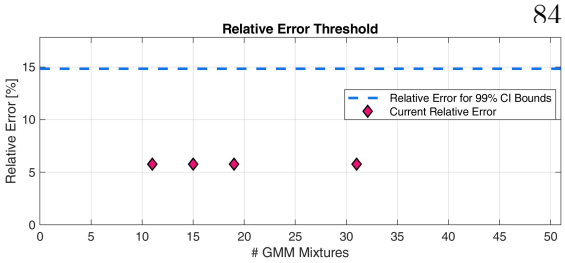

(b) Relative error between the semi-analytical method and the Monte Carlo results.

Figure 5.15: Halo test case 1: These plots show the comparison of the probability of collision from the semi-analytical method developed in this paper to the Monte Carlo probability of collision. The solid blue line shows the Monte Carlo probability of collision, the dashed blue lines show the 99% error threshold, and the pink diamonds show the probability of collision computed using the semi-analytical uncertainty propagation.

It is clear from these plots that the probability of collision from the semi-analytical method stays close to the same relative error as we increase the number of components. This is because of the lower initial uncertainty choice. It is important to note that, as the time of propagation and the uncertainty increases, more components are needed to achieve the same accuracy.

5.2.2.2 Example 2

Another test was run with a longer propagation time to study the change in convergence and the number of GMM components needed to capture the propagation for collision probability calculations. The first trajectory is the same Halo orbit as the subsection above. The epoch states of the two objects are listed in Table 5.11. The TCA is about 16.8 days and the covariance associated with object 1 is 173 m in position and 1.73 $\frac{mm}{s}$ in velocity. Figure 5.16a shows the nominal trajectories of the two objects in a two dimensional view, Figure 5.16b shows the trajectories in a three dimensional view, and Figure 5.16c shows the uncertainty overlap of the distributions at the nominal TCA.

The Monte Carlo analysis is performed using ten million points and the hybrid method of collision probability is also run using a variety of GMM components to capture the probability. Same as the previous cases, Figures 5.17a and 5.17b show that the hybrid collision probability matches

Orbital Elements	x	y	z	$\dot{x}$	$\dot{y}$	$\dot{z}$
Object 1	0.89615	0	-0.1991	0	0.19234	0
Object 2	-0.62924	-0.69684	0.05471	-0.070547	0.059268	0.22747

Table 5.11: Orbital Elements for the second Halo test case. Object 1 is in an L1 Halo orbit.

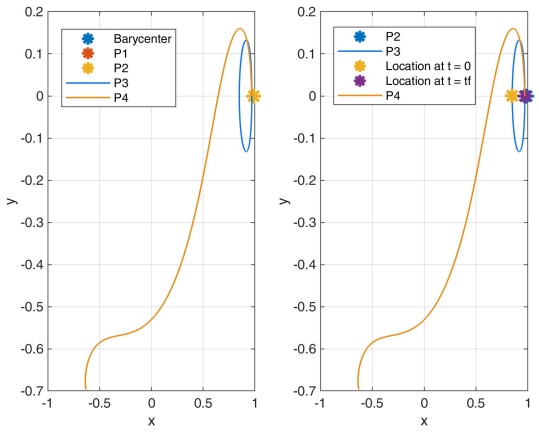

(a) Planar trajectories of the two objects in conjunction.

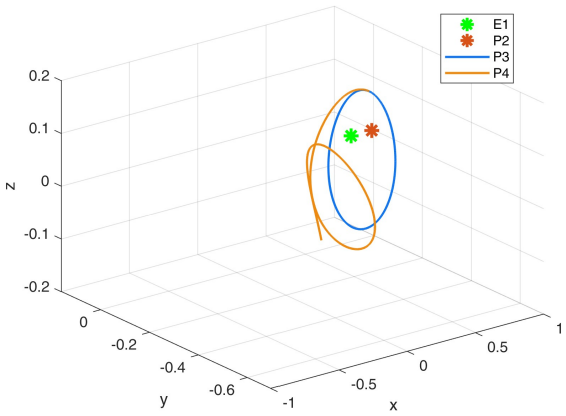

(b) 3D trajectories.

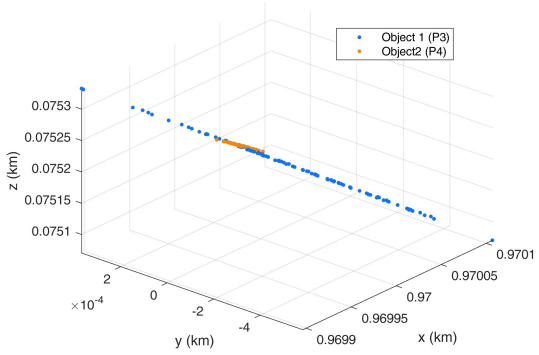

(c) Uncertainty of the two objects propagated to the nominal TCA.

Figure 5.16: Halo test case 2: (a) and (b) show the trajectories on the two objects in conjunction in 2D and 3D views, respectively. The blue and yellow trajectories refer to the Halo orbit and the secondary object orbit, respectively. (c) shows the propagated uncertainty of the two objects at the nominal TCA.

the Monte Carlo collision probability even with a low number of components. It is possible that this can be attributed to the low covariances values associated with the two objects in conjunction.

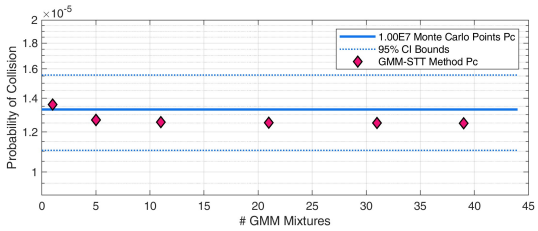

(a) Semi-analytical method probability of collision vs the Monte Carlo results.

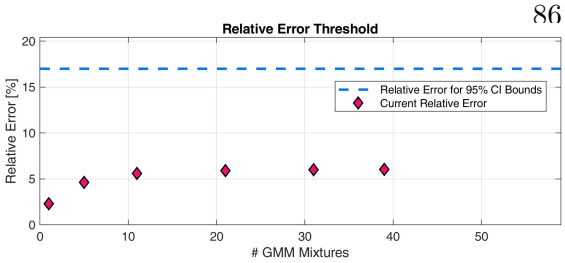

(b) Relative error between the semi-analytical method and the Monte Carlo results.

Figure 5.17: Halo test case 2: These plots show the comparison of the probability of collision from the semi-analytical method developed in this paper to the Monte Carlo probability of collision. The solid blue line shows the Monte Carlo probability of collision, the dashed blue lines show the 95% error threshold, and the pink diamonds show the probability of collision computed using the semi-analytical uncertainty propagation.

5.2.3 NRHO Test Case

Another example is run using a Near Rectilinear Halo Orbit (NRHO) about Lagrange Point 2 (L2) [75]. The states at epoch are listed in Table 5.12. The nominal TCA is about 9.9 days. A diagonal initial covariance is set at 315 m in position and 3.15 $\frac{mm}{s}$ in velocity for object 1, and 173 m in position and 1.73 $\frac{mm}{s}$ in velocity for object 2.

Orbital Elements	x	y	z	$\dot{x}$	$\dot{y}$	$\dot{z}$
Object 1	1.0224	0	-0.18236	0	-0.10408	0
Object 2	1.0113	0.021088	-0.041604	-0.011389	-0.095117	0.44639

Table 5.12: Orbital Elements for the NRHO test case. Object 1 is in an L2 NRHO orbit.

Figure 5.18a shows the nominal trajectories of the two objects in a two dimensional view, Figure 5.18b shows the nominal trajectories in a three dimensional view, and Figure 5.18c shows the uncertainties of the two objects propagated to the nominal TCA.

The Monte Carlo analysis is run using ten million points and the hybrid method is run using a varying number of GMMs. To demonstrate the importance of the splitting direction, two results are produced, one with the GMM splits in a low nonlinearity splitting direction and one with the GMM splits performed in the highest nonlinear splitting directions.

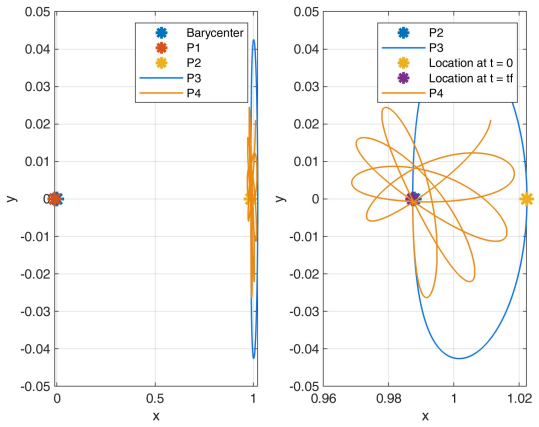

(a) Planar trajectories of the two objects in conjunction.

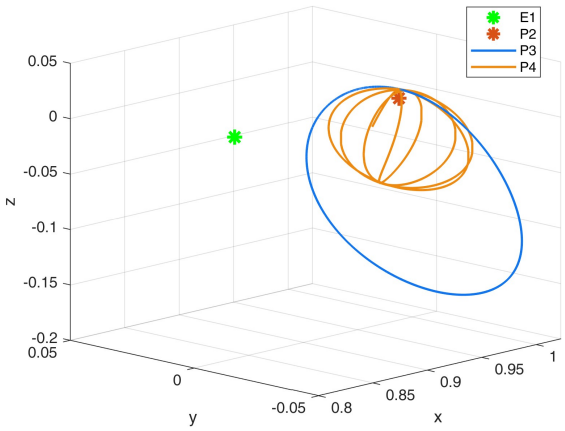

(b) 3D trajectories.

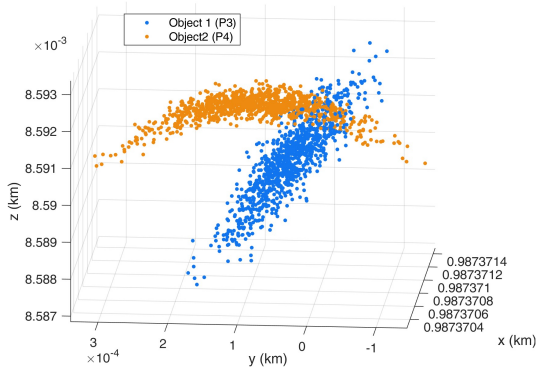

(c) Uncertainty of the two objects propagated to the nominal TCA.

Figure 5.18: NRHO test case: (a) and (b) show the trajectories on the two objects in conjunction in 2D and 3D views, respectively. The blue and yellow trajectories refer to the NRHO orbit and the secondary object orbit, respectively. (c) shows the propagated uncertainty of the two objects at the nominal TCA.

Figure 5.19a and Figure 5.19b compare the Monte Carlo and GMM-STT methods of collision probability calculations, where the GMM split for the two objects is performed in a low nonlinearity splitting direction. Figure 5.20a and Figure 5.20b compare the numerical and hybrid methods to analyze the accuracy of the method with GMM split for the two objects performed in their respective highest nonlinearity directions.

Even though the figures don't show a convergence to a 95% confidence interval in this case, the relative error improves greatly for the high nonlinearity splitting direction compared to the low

nonlinearity splitting direction. In this "good" or high nonlinear splitting direction, the relative error is settles at just below 20%. A potential cause for the relative error to converge outside of the 95% confidence bounds could be the splitting direction choice. Even though the GMM split is performed in the highest nonlinearity direction, the choice is still made from a finite set of predetermined directions as explained in chapter 3. It is possible that exploring more directions or computing the direction in a more complex way could lead to a better convergence with the numerical collision probability. Additionally, performing recursive splits in multiple directions of high nonlinearity could also improve the results.

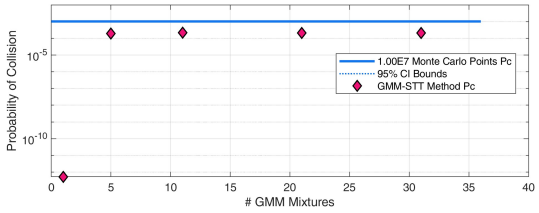

(a) Semi-analytical method probability of collision vs the Monte Carlo results.

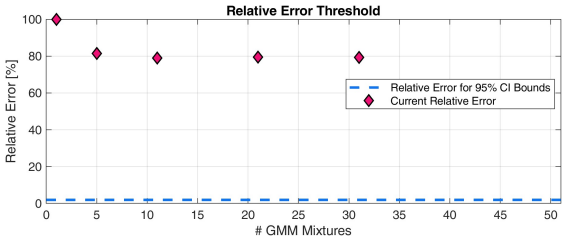

(b) Relative error between the semi-analytical method and the Monte Carlo results.

Figure 5.19: NRHO test case with "bad" GMM splitting: These plots show the comparison of the probability of collision from the semi-analytical method developed in this paper to the Monte Carlo probability of collision. The solid blue line shows the Monte Carlo probability of collision, the dashed blue lines show the 95% error threshold, and the pink diamonds show the probability of collision computed using the semi-analytical uncertainty propagation.

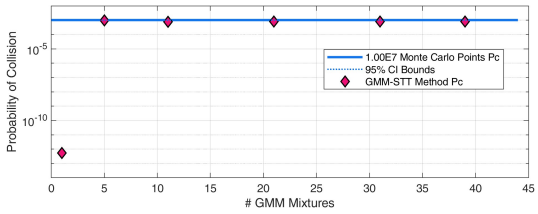

(a) Semi-analytical method probability of collision vs the Monte Carlo results.

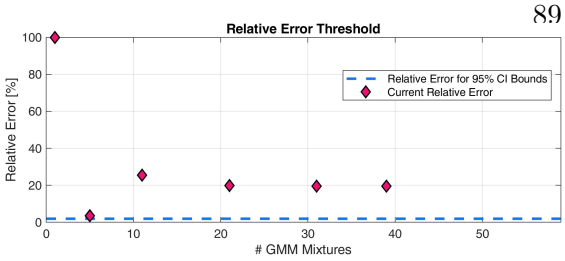

(b) Relative error between the semi-analytical method and the Monte Carlo results.

Figure 5.20: NRHO test case with "good" GMM splitting: These plots show the comparison of the probability of collision from the semi-analytical method developed in this paper to the Monte Carlo probability of collision. The solid blue line shows the Monte Carlo probability of collision, the dashed blue lines show the 95% error threshold, and the pink diamonds show the probability of collision computed using the semi-analytical uncertainty propagation.

5.3 Discussion

In this chapter, various test cases are presented in near-Earth and cislunar regimes to test the accuracy of the hybrid uncertainty propagation and conjunction analysis method developed in chapter 4. The following examples are presented: a Two-Body (2BP) dynamics test case, a repeating conjunction study with the 2BP dynamics, a J_2 secular dynamics test case, two test cases using the Simplified Dynamics System: short-duration and long-duration conjunctions, and lastly four cislunar test cases with Circular Restricted Three-Body Problem dynamics: an L1 Lyapunov orbit test case, two L1 Halo orbit test cases, and an L2 Near Rectilinear Halo orbit example. All test cases prove the validity of this method with test cases showing varying, but low relative errors. Some test cases also demonstrate the significant improvement in time in comparison to numerical Monte Carlo collision probability calculations.

Chapter 6

Near-Earth GitHub-Accessible Toolkits

The hybrid conjunction analysis techniques developed for near-Earth region in the previous chapters are coded in MATLAB to test cases. Some of these results are presented in chapter 5. This chapter presents the MATLAB conjunction toolkits applicable to short-term and long-term conjunctions. It takes inputs such as orbital parameters and generates a probability of collision using the hybrid semi-analytical uncertainty propagation conjunction analysis. The MATLAB scripts for this toolkit have been uploaded to GitHub and can be accessed using short-term [48] and long-term [47] repositories. The code implementation and initialization are defined in this paper.

First, the code implementation of the method of semi-analytical uncertainty propagation and probability of collision calculations is described. This is followed by a detailed implementation of the Monte Carlo probability of collision calculations. After the method implementations, the code initialisation parameters are defined and a test case is presented. Additionally, the parameters for the test case are listed and the outputs from the code are presented. This toolkit is accessible for public use and can be used to test short and long duration conjunction in the near-Earth space.

6.1 Semi-Analytical Uncertainty Propagation and Probability of Collision Calculation Implementation

Fig. 6.1 summarises the semi-analytical method of uncertainty propagation used for probability of collision calculations in near-Earth realm in the script 'ComputeGMMSTTMethodPc.m'. The initial distribution is transformed to an Equinoctial element set using a Jacobian matrix ('JacobianCalc.m') and a sub-optimal algorithm from Horwood et al. [39] is used to split this uncertainty into a chosen number of GMM components. These smaller distributions are converted to Delaunay frame using another Jacobian matrix for propagation using the STTs. Hamiltonian averaging is used to compute mean dynamics and the analytical time-dependent short-period variation equations. The mean dynamics are used to compute the STTs for the GMM component propagation.

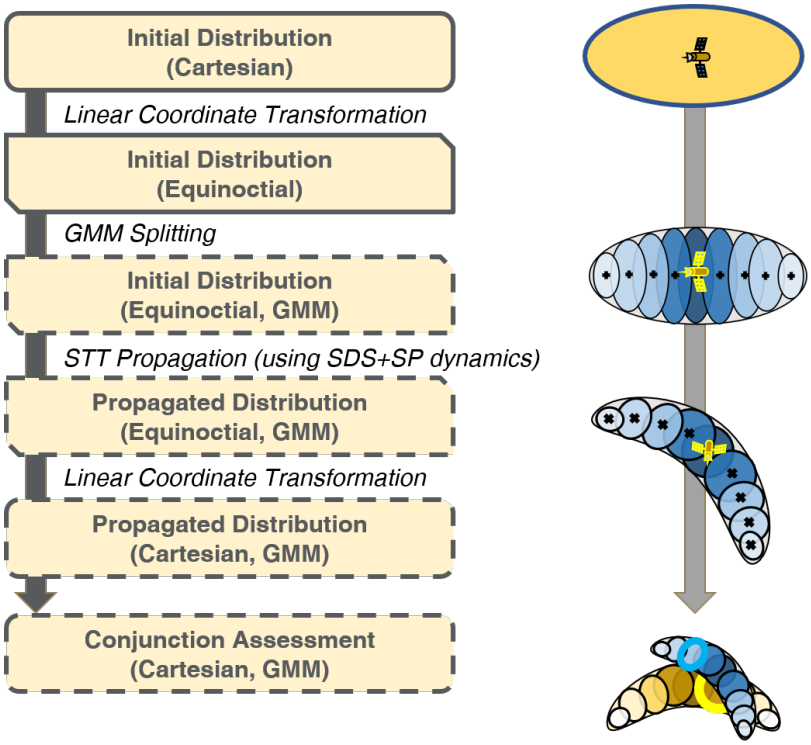

Figure 6.1: A summary of the semi-analytical uncertainty propagation and conjunction analysis method. [51]

The propagated GMM components are then compared in an all-on-all analysis to calculate the probability of collision. These probabilities are combined using a double weighted sum to

achieve a cumulative probability of collision of the system. A benefit of this is that the individual GMM components maintain Gaussianity and thus, can be combined with the Foster method of probability of collision calculation [32].

6.1.1 Gaussian Mixture Model Splitting

The GMM is split using the Horwood et al. [39] sub-optimal algorithm. This section is set up using the optimization toolbox in MATLAB. A parameter $m = 6$ is defined to initiate the splitting process. Based on this, the following algorithm is set up:

(1) $\sigma = \frac{2m}{N-1}$, where N is the number of GMM components to split into.

(2) For $\alpha = 1, ..., N$, $\mu_\alpha = -m + \sigma(\alpha - 1)$

(3) Compute matrix $(\boldsymbol{M})_{\alpha\beta} = \mathcal{N}(\nu_\alpha - \nu_\beta; 0, 2\sigma^2)$ and vector $(\boldsymbol{n})_\alpha = \mathcal{N}(\nu_\alpha; 0, \sigma^2 + 1)$ using function normpdf.

(4) Define an optimization using quadprog, with 'ConstraintTolerance' of 10^{-25} and 'OptimalityTolerance' of 10^{-25} to minimize: $\frac{1}{2}\boldsymbol{w}^T\boldsymbol{M}\boldsymbol{w} - \boldsymbol{w}^T\boldsymbol{n}$ over $\boldsymbol{w}$ subject to constraints: $\sum_{\alpha=1}^{N} w_\alpha = 1$ and $w_\alpha \geq 0$, where $\alpha = 1, ..., N$

(5) For same α, calculate $\tilde{w}_\alpha = \frac{\sqrt{2\pi}}{\sqrt{1-\sigma^2}} w_\alpha \exp\left[\frac{\mu_\alpha^2}{2(1-\sigma^2)}\right]$, $\tilde{\mu}_\alpha = \frac{\mu_\alpha}{1-\sigma^2}$, and $\tilde{\sigma}^2 = \frac{\sigma^2}{1-\sigma^2}$

(6) Compute $\hat{\mu}_\alpha = \nu^1 + \sqrt{Q^1}\tilde{\mu}_\alpha$, $\hat{w}_\alpha = \tilde{w}_\alpha$, and $\hat{\sigma}^2 = \tilde{\sigma}^2 Q^{11}$

(7) Based on this, $\bar{\boldsymbol{Q}} = (\hat{\sigma}^{-2}\boldsymbol{e}_1\boldsymbol{e}_1^T + \boldsymbol{Q}^{-1})^{-1}$, $\bar{\boldsymbol{\nu}}_\alpha = \bar{\boldsymbol{Q}}(\hat{\sigma}^{-2}\hat{\mu}_\alpha\boldsymbol{e}_1 + \boldsymbol{Q}^{-1}\boldsymbol{\nu})$, and $\bar{w}_\alpha = \hat{w}_\alpha \mathcal{N}(\hat{\mu}_\alpha - \boldsymbol{e}_1^T\boldsymbol{\nu}; 0, \hat{\sigma}^2 + \boldsymbol{e}_1^T\boldsymbol{Q}\boldsymbol{e}_1)$, where $\boldsymbol{e}_1 = (1, 0, ..., 0)^T \in \mathbb{R}$

(8) For $\alpha = 1, ..., N$, compute re-normalized weights $\bar{w}_\alpha = \bar{w}_\alpha / \sum_{\beta=1}^{N} \bar{w}_\beta$

This splitting function 'GMM_Component_Calcs.m' uses the number of components, nominal mean, nominal covariance, and a test flag as inputs. It outputs the GMM component weights ($\bar{w}$), means ($\bar{\boldsymbol{\mu}}$), and covariance ($\bar{\boldsymbol{Q}}$).

6.1.2 Simplified Dynamical System

The MATLAB symbolic computer is used to develop the Hamiltonian averaging equations to compute the mean dynamics equations and the time-based short-period variation equations in the script 'SDSGenerator.m'. As described in previous chapters, the SDS in the toolkit uses non-Keplerian perturbations from Solar Radiation Pressure (SRP) and J2 gravitational harmonics. The state and state Equations of Motion (EOMs) are represented as follows:

$$\begin{aligned} \boldsymbol{x}_{\text{del}} &= [l,\ g,\ h,\ k_{\odot}, L,\ G,\ H,\ K_{\odot}] \\ \boldsymbol{f}_{\text{del}} &= [\dot{l},\ \dot{g},\ \dot{h},\ \dot{k}_{\odot},\ \dot{L},\ \dot{G},\ \dot{H},\ \dot{K}_{\odot}] \end{aligned} \tag{6.1}$$

The mean Hamiltonian and generating function equations are shown in Appendix A. The mean dynamics are stored in the function: 'MeanDynamicsFunction.m' and the short-period offsets from mean to osculating and vice-versa are stored in 'getInitialDelOffset.m' and 'getFinalDelOffset.m', respectively. These offset functions can be accessed using the script 'getOffset.m' that uses state, time, constants, and a direction flag as inputs. It outputs the offset in the chosen direction.

6.1.3 State Transition Tensors

MATLAB symbolic computer is used to compute the STT EOMs. These EOMs are then used to propagate the STTs to the final time. The propagated STTs are used to map the mean and covariance of the GMM components to the final time using the following set of equations:

$$\dot{\Phi}_{i,ab} = \sum_{\alpha=1}^{N} A_{i,\alpha}\Phi_{\alpha,ab} + \sum_{\alpha=1}^{N}\sum_{\beta=1}^{N} A_{i,\alpha\beta}\Phi_{\alpha a}\Phi_{\beta b} \tag{6.2}$$

Here, $\Phi_{\alpha,ab}$ is a second order STT, $\Phi_{\alpha a}$ and $\Phi_{\alpha b}$ are first order STTs, $A_{i,\alpha}$ is the first order Local Dynamics Tensor (LDT), and $A_{i,\alpha\beta}$ is the second order LDT. N denotes the state dimension. i, a, and b are the three dimensions of the STT EOMs. The LDTs are computed using partials of the system dynamics with respect to the state about the nominal trajectory (denoted by *) as shown in the following equation.

$$A_{i,k_1...k_p} = \left. \frac{\partial^p \boldsymbol{f}_{\text{del}i}}{\partial \boldsymbol{x}_{\text{del}k_1} ... \partial \boldsymbol{x}_{\text{del}k_p}} \right|_* \tag{6.3}$$

where, i and k_j are the dimensions of the LDT.

The LDT calculations are performed using the MATLAB symbolic computer by taking symbolic partial derivatives of the Delaunay mean dynamics from the SDS with respect to the state in function: 'SymbolicSDSJ2Computer.m'. 'propagateWithDynamics.m' script is used to propagated the STTs alongside the state using ode113, with 10^{-13} as the relative and absolute tolerances.

6.1.4 Time of Closest Approach Finder

The function 'FindTCAGMMSTTMethod.m' is used to find the time of closest approach (TCA) between two chosen GMM components. Fig. 6.2 shows the propagation process for the GMM component means. The means of the GMM components are mapped to the final propagation time using the STTs computed with the mean dynamics using the function 'STTcalcs2BP.m':

$$\delta \boldsymbol{m}_i(t) = \sum_{p=1}^{m} \frac{1}{p!} \Phi_{i,k_1...k_p} \; E[\delta \boldsymbol{x}_{k_1}^0 ... \delta \boldsymbol{x}_{k_p}^0] \tag{6.4}$$

where, the moments, E, are defined in functions 'E1calc.m' and 'E2calc.m' using:

$$\begin{aligned} E[\delta \boldsymbol{x}_i] &= \delta \boldsymbol{m}_i \\ E[\delta \boldsymbol{x}_i \delta \boldsymbol{x}_j] &= \delta \boldsymbol{m}_i \delta \boldsymbol{m}_j + \boldsymbol{P}_{ij} \\ E[\delta \boldsymbol{x}_i \delta \boldsymbol{x}_j \delta \boldsymbol{x}_k] &= \delta \boldsymbol{m}_i \delta \boldsymbol{m}_j \delta \boldsymbol{m}_k + (\delta \boldsymbol{m}_i \boldsymbol{P}_{jk} + \delta \boldsymbol{m}_j \boldsymbol{P}_{ik} + \delta \boldsymbol{m}_k \boldsymbol{P}_{ij}) \\ &... \end{aligned} \tag{6.5}$$

The TCA approach between two GMM components is calculated using a stepping method that uses the time update:

$$t = \frac{\Delta \boldsymbol{r} . \Delta \boldsymbol{v}}{|\Delta \boldsymbol{v}|^2} \tag{6.6}$$

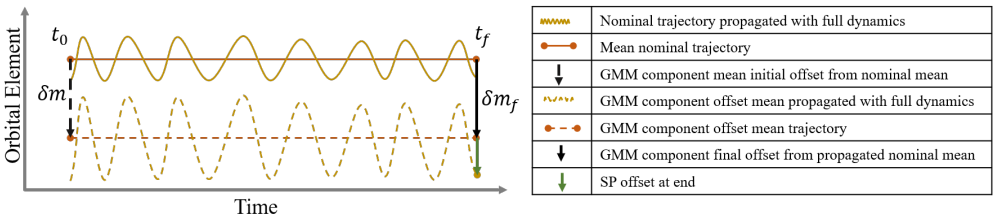

Figure 6.2: The initial GMM component mean is a deviation from the nominal mean state. This GMM mean is mapped to the final time using STTs and it is converted back to the osculating state. [51]

where $\Delta \boldsymbol{r}$ and $\Delta \boldsymbol{v}$ are the relative position and velocity vectors respectively. Each time update ensures a smaller difference in the relative distance between the two objects at the next time. The final converged time is the actual TCA. The covariance is mapped ('Covariance_Propagation.m') to this actual TCA using the second order STTs, as described in the equation below:

$$\boldsymbol{P}_{ij}(t) = \left(\sum_{p=1}^{m} \sum_{q=1}^{m} \frac{1}{p!q!} \Phi_{i,k_1 \ldots k_p} \Phi_{j,l_1 \ldots l_q} E[\delta \boldsymbol{x}_{k_1}^0 \ldots \delta \boldsymbol{x}_{k_p}^0 \delta \boldsymbol{x}_{l_1}^0 \ldots \delta \boldsymbol{x}_{l_q}^0] \right) - \delta \boldsymbol{m}_i(t) \delta \boldsymbol{m}_j(t) \tag{6.7}$$

The means and moments are the same as those described in Eq. 3.11 and Eq. 2.45, respectively.

6.1.5 Probability of Collision Calculations

Each propagated GMM components associated with the objects in conjunction are compared in an all-on-all analysis at their respective actual TCAs to achieve the cumulative probability of collision, as demonstrated in Fig. 6.3. This is done using the function script: 'GMM_Pc_Calcs_Fun.m'. The individual probability of collision between the i^{th} and j^{th} components of objects 1 and 2 respectively, can be computed using:

$$P_{c,ij} = \frac{1}{2\pi \sqrt{|P^*|}} \int_{-R}^{R} \int_{-\sqrt{R^2-x^2}}^{\sqrt{R^2-x^2}} \exp\left(-A^*\right) dz\, dx \tag{6.8}$$

P^* is the combined covariance of the two objects and A^* is defined as follows:

$$\boldsymbol{s} = x\boldsymbol{i} + z\boldsymbol{k},\ \boldsymbol{s}_0 = x_0\boldsymbol{i} + z_0\boldsymbol{k} \tag{6.9a}$$

$$A^* = (\boldsymbol{s} - \boldsymbol{s}_0)^T P^{*-1}(\boldsymbol{s} - \boldsymbol{s}_0)/2 \tag{6.9b}$$

where, s and s_0 are the relative positions in the encounter plane at the actual and nominal TCA, respectively.

The individual probabilities are combined using a double weighted sum:

$$P_c = \sum_{i=1}^{L_a}\sum_{j=1}^{L_b} w_a^{(i)} w_b^{(j)} P_{c,ij} \tag{6.10}$$

where, $w_a^{(i)}$ and $w_b^{(j)}$ are the weights associated with the i^{th} and j^{th} GMM components of objects 1 and 2, respectively. The double integral to compute the total probability of collision is implemented using 'integral2' in MATLAB.

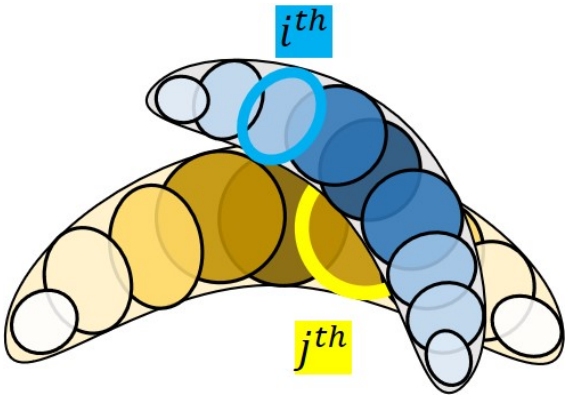

Figure 6.3: Each GMM component from object 1 is compared to that from object 2 to compute the cumulative probability of collision. [50]

6.2 Monte Carlo Method

In the Monte Carlo analysis, a cloud of points is propagated numerically to evaluate the probability of collision in the function script: 'Compute_MC_Pc_Cart_1on1.m'.

A random point is generated for each object in conjunction from the nominal states and epoch covariances using 'mvnrnd'. These points are propagated using 'propagateWithDynamics.m' to find the actual TCA, as shown in Fig. 6.4. The actual TCA is found using 'FindTCAMCMethod.m' with 'while' loops, using the nominal TCA as an initial guess. Same as before, the time update is computed as described in Eq. 6.6 using the relative position and velocity of the two objects.

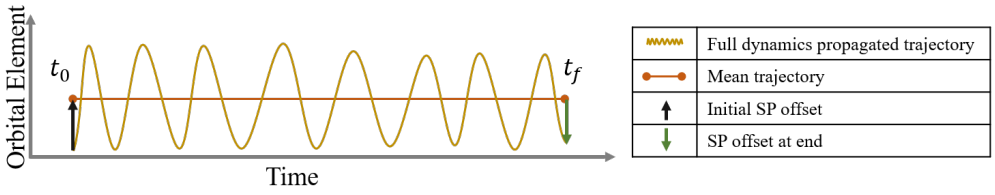

Figure 6.4: The initial state is converted to a mean state and is mapped to the final time using STTs, where it is converted back to the osculating state. [51]

The probability of collision in the Monte Carlo analysis is calculated by comparing the number of objects closer than the combined hard body radii of the two objects, to the total number of points in the analysis.:

$$\text{MC } P_c = \frac{\text{Conjunctions where DCA } < R}{\text{Total number of conjunctions tested}} \tag{6.11}$$

The binomial confidence bounds are found using the normal approximation [54]:

$$\text{CI} = \text{MC } P_c \pm z\sqrt{\frac{\text{MC } P_c(1 - \text{MC } P_c)}{n}} \tag{6.12}$$

$z = 1.96$ for a 95% confidence interval and n denotes the number of points in the Monte Carlo analysis.

6.3 Code Initialization

To initiate the code, the only scripts that need to be edited are: 'Main_Code.m' and 'constantsAndInitialState.m'. The states and uncertainties of the two objects in conjunction and some

constant parameters need to be defined. The input parameters that are required to run the code and that can be changed without needing code updates include:

Main_Code.m	
runMonteCarlo:	When toggled to 1, this flag allows the Monte Carlo probability of collision calculation process to run, using a chosen number of points.
runGMMSTTMethod:	When toggled to 1, this flag allows the semi-analytical GMM-STT probability of collision calculation process to run, using a chosen number of points.
plotThings:	Flag to plot probability of collision results.
saveResultsToText:	Save results to an output file.

constantsAndInitialState.m	
[a e i O w M]:	[km and rad] Classical orbital elements (COEs) defining the epoch states of the two objects in conjunction.
P and P2:	[km and km/s] Cartesian covariance of both objects in conjunction.
constants.case_flag:	Pre-coded sample test cases can be accessed using this variables.
constants.points:	Number of Monte Carlo points currently being evaluated for each object.
constants.JMAX:	List of number of GMM components to split each object into. The only limitation is that this script cannot split the distribution into less than 15 components.
constants.testFig2:	When toggled to 1, this test flag plots the GMM mean spread for object 1 at the nominal TCA using 15 components. 'runMonteCarlo' and 'runGMMSTTMethod' must be toggled to 1 to run this.
constants.plot_GMM_ell:	When toggled to 1, this test flag plots the GMM covariances, in addition to their means. 'runMonteCarlo' and 'runGMMSTTMethod' must be toggled to 1 to run this.
constants.testFig4:	When toggled to 1, this test flag plots the weights against the means of the GMM distribution. 'runGMMSTTMethod' must be toggled to 1 to run this.
constants.par:	Allow parallel runs in MATLAB.
constants.nodes:	Number of nodes allowed for the parallel MATLAB runs.
usePredefinedCases:	When toggled to 1, this flag allows the predefined test cases to be accessed, using constants.case_flag.
constants.P_prop:	Define Nominal TCA.
ICState.obj2.COE:	Define the COE for object 2.
r1:	Hard body radius of object 1.
r2:	Hard body radius of object 2.
constants.rho:	Reflectivity of the objects.
constants.Aom:	Area over mass ratio of objects.

6.4 Test Case

A case for the short-term conjunction case is setup below and the code is initiated for a test run.

6.4.1 Example Setup

The inputs and constants to run this example test case are listed in the initialization table below. The initial states and epochs are introduced. The flags: 'runMonteCarlo' and 'runGMM-STTMethods' are toggled to 1 to run the probability of collision calculations using both methods. 'plotThings' is 1 to allow plotting of the results. 10^7 points are generated associated with object and tested for probability of collision calculations. No test figures are plotted and parallelization is turned off. Nominal TCA is set to 1.5 days. The hard body radii of the two objects and other parameters are also defined in the table.

Fig 6.5a shows the nominal trajectories of the two objects and their conjunction point. Fig. 6.5b shows the uncertainty distribution of the two objects at the nominal TCA.

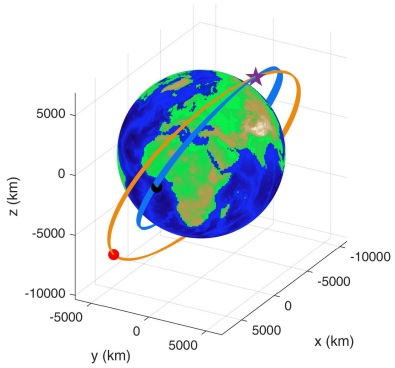

(a) Nominal trajectories. [50]

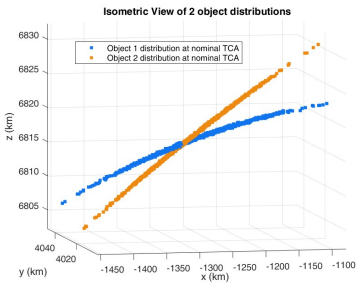

(b) Uncertainty distribution at the nominal TCA.

Figure 6.5: (a) Blue and yellow trajectories show the nominal trajectories of objects 1 and 2, respectively. The black dot and red dot denote the initial locations of objects 1 and 2, respectively. Purple star denotes the conjunction point. (b) The blue points and yellow points show the uncertainty distributions at the nominal TCA of objects 1 and 2, respectively.

The probability of collision for this test case is first computed with the Monte Carlo analysis, followed by the semi-analytical approach. This allows a comparison between the two results.

Main_Code.m

---

runMonteCarlo:	1
runGMMSTTMethod:	1
plotThings:	1
saveResultsToText:	0

---

constantsAndInitialState.m

[a e i O w M]:	[km and deg] [8000; 0.15; 60; 0; 0; 0]
P and P2:	[km and km/s] [0.0067664 -0.0029183 0.0027112 -9.9816E-7 -1.7636E-7 2.1797E-6;... -0.0029183 0.005348 -0.0011671 -1.5861E-6 -3.5203E-7 3.3414E-6;... 0.0027112 -0.0011671 0.001087 -3.9883E-7 -7.5945E-8 8.6148E-7;... -9.9816E-7 -1.5861E-6 -3.9883E-7 9.4587E-9 -1.1375E-10 1.1511E-9;... -1.7636E-7 -3.5203E-7 -7.5945E-8 -1.1375E-10 9.8844E-9 8.5671E-11;... 2.1797E-6 3.3414E-6 8.6148E-7 1.1511E-9 8.5671E-11 7.2859E-9]
constants.case_flag:	1
constants.points:	1E7
constants.JMAX:	[37;101;301;501]
constants.testFig2:	0
constants.plot_GMM_ell	0
constants.testFig4:	0
constants.par:	0
constants.nodes:	4
usePredefinedCases:	0
constants.P_prop:	1.5 days
ICState.obj2.COE:	[km and deg] [9843.3; 0.241038; 61.8685; -10.9875; 55.5795; -87.5619]
r1:	20 m
r2:	20 m
constants.rho:	0.2
constants.Aom:	2E-6

6.4.2 Results

The Monte Carlo scripts outputs a probability of collision of 4.67×10^{-5} in 5.3 hours [50] (when run with 24 parallel nodes on the CU Boulder supercomputer), when using the SDS dynamics. The semi-analytical GMM-STT script outputs a probability of collision of: 3.8894×10^{-5}, 4.8952×10^{-5}, 4.8659×10^{-5}, 4.8560×10^{-5} with 37, 101, 301, and 501 components, respectively. The semi-analytical computation with 101 components takes 4.43 minutes [50] (when run with 24 parallel nodes on the CU Boulder supercomputer).

Fig 6.6a shows the comparison between the Monte Carlo results and those from the semi-analytical method. Fig. 6.6b shows the relative error between these two results. It is clear that above 101 components, the results have converged with the Monte Carlo probability of collision. This confirms the validity of the method and provides a demonstration of the toolkit.

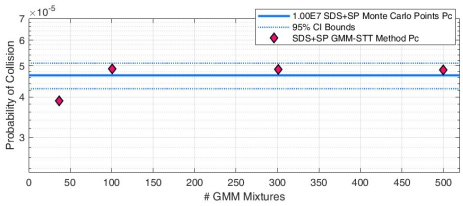

(a) Probability of collision results. [50]

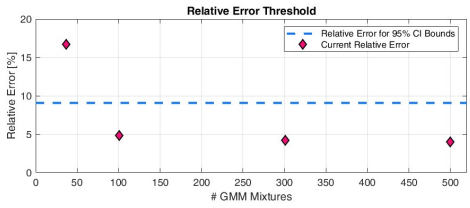

(b) Relative error in results.

Figure 6.6: (a) The solid blue line refers to the Monte Carlo probability of collision and the dashed blue lines are the confidence intervals around this result. The pink diamonds show the semi-analytical approach probability of collision at different number of GMM components. (b) The dashed line shows the binomial normal approximation 95% confidence interval line. The pink diamonds show the semi-analytical approach results for the probability of collision.

6.5 Conclusion

This chapter provides a semi-analytical uncertainty propagation conjunction analysis (SAUPCA) toolkit that can propagate the uncertainty and evaluate the probability of collision results in an accurate and efficient manner. The chapter describes the implementation of different components of the coded toolkit and the parameters that need to be defined to initiate the code. A test case is presented that is set up using defined constants and initial states and covariances of the two objects

in conjunction. The probability of collision is calculated using the Monte Carlo analysis and the SAUPCA toolkit to test the output and compare the final results. The plotted results show a convergence of the SAUPCA probability of collision with those from the Monte Carlo analysis, hence demonstrating a successful run. The toolkit can be accessed through GitHub repositories [48, 47] online.

Chapter 7

Conclusions and Future Work

7.1 Conclusions

An increasing need for Space Situational Awareness (SSA) tools in near-Earth and cislunar space has motivated research in analytical and semi-analytical methods of uncertainty propagation and conjunction analysis. This work presents a new method of semi-analytical uncertainty propagation that accurately captures nonlinear evolution of the distribution with high fidelity dynamics and captures the collision probability with high levels of accuracy. Several mathematical tools used in this methodology are presented with their backgrounds, along with evidence of their functionality and applicability. Additionally, a variety of test cases are used to demonstrate the statistical accuracy and speed of this method.

Chapter 2 begins with a mathematical background on low and high fidelity dynamics that can be used for propagation. A high fidelity model is presented that can incorporate perturbations without compromising on computation speed. This Simplified Dynamical System (SDS) adds J_2 and Solar Radiation Pressure perturbations to allow realistic propagation. In addition to this, the Circular Restricted Three-Body Problem (CR3BP) is described for use in cislunar applications. State Transition Tensors (STTs) are defined and applied for direct moment mapping of the system probability density function (PDF). These STTs are computed analytically for the Two-Body Problem (2BP) and for J_2 secular perturbed dynamics, and semi-analytically for the SDS and the CR3BP. Once computed, the STTs can be used to map the mean and covariance of a distribution to desired times with speed and accuracy.

Chapter 3 provides a mathematical introduction to Gaussian Mixture Models (GMMs) which allow the system PDF to be represented as a Gaussian sum. Propagating each component from this sum maintains individual component linearity over long propagation times. Splitting methods are presented for the near-Earth and cislunar applications. STT propagation is introduced to accurately map individual components means and covariances with chosen dynamical models. A weighted sum of these mapped GMM components gives the total distribution. Test cases are presented demonstrating a capture of the final nonlinear distribution using GMM-STT propagation in both near-Earth and cislunar cases.

Chapter 4 introduces probability of collision methods. A Monte Carlo method is first presented that can be used to establish baseline truth to compare analytical and semi-analytical methods against. A general probability of collision equation is combined with a weighted GMM sum to allow the calculation of a cumulative probability by using individual interactions between GMM components mapped with STTs. Then, starting from the general probability of collision equation, a reduced probability formula is achieved through simplifications that arise from propagation with the GMM-STT method. This reduced formula of probability of collision is applicable to short and long duration conjunctions, with implementations in near-Earth and cislunar domains.

In chapter 5, a series of test cases are presented to evaluate the collision probability techniques developed throughout the previous chapters. Examples are developed for 2BP dynamics, J_2 secular dynamics, the SDS, and the CR3BP to test the validity of these methods. Performance analysis is run to test the statistical accuracy of the collision probability calculated using the analytical and semi-analytical methods against the Monte Carlo results, along with a time comparison between the different methods.

Chapter 6 shares two Github-accessible toolkits for near-Earth short and long duration conjunctions. It discusses the implementation of the previously defined uncertainty propagation and conjunction analysis methods, along with code initialization parameters and a test case to evaluate a run. These online toolkits are available for public use.

This dissertation presents and tests new methods of conjunction analysis in near-Earth and

cislunar realms. The analysis verifies that the techniques developed are accurate, efficient, and realistic in their application in short and long duration conjunctions.

7.2 Future Work

There are many possible extensions and applications of the techniques and methods developed in this dissertation. In this section, we briefly list future research avenues that can be explored.

- Additional dynamical perturbations can be incorporated in near-Earth applications by simply adding perturbations to the SDS [64], and in cislunar applications by combining more advanced dynamical models in the GMM-STT uncertainty propagation method. Forces to be considered for near-Earth applications include: higher accuracy spherical harmonics models, third-body effects, and non-conservative forces such as drag.

- Adaptive/automated GMM component selection: The method can be improved by implementing additional automation, such that the number of components needed to accurately capture the nonlinear evolution of a distributions are precomputed. This avoids the additional computations with a different number of GMM components until convergence with the Monte Carlo method is observed. Several previously developed methods that use GMMs have proposed ways of detecting nonlinearity in the system, such as work by DeMars et al. [24].

- In this work, the cislunar Gaussian mixture sum is gathered using a split in the largest nonlinearity direction. This GMM split can be performed repeatedly and recursively [79] in case of multiple directions with high nonlinearity to capture the uncertainty evolution with more accuracy. This could reduce the relative error between the GMM-STT collision probability and the Monte Carlo results.

- Another addition to the future work is using this nonlinear semi-analytical GMM-STT uncertainty propagation method to develop semi-analytical filtering techniques. Our method

of uncertainty propagation would allow the evolution of the probability function to be tracked, hence allowing us to associate measurements with the respective distributions. This work will be a continuation of work by Fujimoto [36], where similar object association is performed using analytical uncertainty propagation methods.

- Cislunar controls techniques have been developed using STTs [9]. It is possible to combine Gaussian sums in similar applications for accuracy.

Bibliography

[1] Optimal collision avoidance of operational spacecraft in near-real time, 2011. Available at `https://clas.ucdenver.edu/mathematical-and-statistical-sciences/sites/default/files/attached-files/spring_2011_-_spacenav-_engau.pdf`.

[2] Salvatore Alfano. Satellite collision probability enhancements. Journal of Guidance Control and Dynamics - J GUID CONTROL DYNAM, 29:588–592, 05 2006.

[3] Salvatore Alfano. Review of conjunction probability methods for short-term encounters. Advances in the Astronautical Sciences, 127:719–746, 01 2007.

[4] Salvatore Alfano. Satellite conjunction monte carlo analysis. Advances in the Astronautical Sciences, 134:2007–2024, 01 2009.

[5] Kyle T. Alfriend, Maruthi R. Akella, Joseph Frisbee, James L. Foster, Deokjin Lee, and Matthew Wilkins. Probability of Collision Error Analysis. Space Debris, 1:21–35, 1999.

[6] Daniel L. Alspach and Harold W. Sorenson. Nonlinear Bayesian estimation using Gaussian sum approximations. IEEE Transactions on Automatic Control, 17(4):439–448, 1972.

[7] Jeffrey Aristoff, Joshua Horwood, and Kyle Alfriend. On a set of j2 equinoctial orbital elements and their use for uncertainty propagation. Celestial Mechanics and Dynamical Astronomy, 133, 03 2021.

[8] Ahmad Bani Younes. Exact computation of high-order state transition tensors for perturbed orbital motion. Journal of Guidance, Control, and Dynamics, 42:1–7, 03 2019.

[9] Spencer Boone and Jay Mcmahon. High-order orbital guidance using state-transition tensors. 01 2018.

[10] Joël Bordeneuve-Guibé, Antoine Drouin, and Clément Roos. Advances in Aerospace Guidance, Navigation, and Control. Springer, 2015.

[11] R. A. Broucke. On the Matrizant of the Two-Body Problem. Astronomy and Astrophysics, 6:173–182, 1970.

[12] R. A. Broucke and P. J. Cefola. On the equinoctial orbit elements. Celestial Mechanics, 5(3):303–310, 1972.

[13] D. Brouwer and G.M. Clemence. Methods of Celestial Mechanics. Academic Press, 1961.

[14] Dirk Brouwer. Solution of the problem of artificial satellite theory without drag. The Astronomical Journal, 64(1274):378–396, 1959.

[15] Chase Patrick Brown. Improved Multidirectional Gaussian Mixture Models Applied to Probability of Collision of Resident Space Objects. PhD thesis, The University of Texas at Austin, 2020.

[16] P. Cefola, A. Long, and JR. G. Holloway. The long-term prediction of artificial satellite orbits.

[17] Ken Chan. Spacecraft Collision Probability. The Aerospace Press. Aerospace Press, 2008.

[18] Ken Chan. Spacecraft collision probability for long-term encounters. 04 2020.

[19] Ken Chan. Elliptical hovering collision probability for long- term encounters. 09 2021.

[20] C Channing Chow, Charles J Wetterer, Jason Baldwin, Micah Dilley, Keric Hill, Paul Billings, and James Frith. Cislunar orbit determination behavior: Processing observations of periodic orbits with gaussian mixture model estimation filters. The Journal of the Astronautical Sciences, 69(5):1477–1492, 2022.

[21] Vincent Coppola. Aas 12-247 including velocity uncertainty in the probability of collision between space objects. 02 2012.

[22] Vincent Coppola. Evaluating the short encounter assumption of the probability of collision formula. 02 2012.

[23] Donald A Danielson, B Neta, and LW Early. Semianalytic satellite theory (SST): Mathematical algorithms. Naval Postgraduate School, 1994.

[24] Kyle DeMars, Robert Bishop, and Moriba Jah. A splitting gaussian mixture method for the propagation of uncertainty in orbital mechanics. volume 140, pages 1419–1438, 02 2011.

[25] Kyle DeMars, Robert Bishop, and Moriba Jah. Entropy-based approach for uncertainty propagation of nonlinear dynamical systems. Journal of Guidance, Control, and Dynamics, 36, 07 2013.

[26] Kyle DeMars, Yang Cheng, and Moriba Jah. Collision probability with gaussian mixture orbit uncertainty. Journal of Guidance, Control, and Dynamics, 37, 05 2014.

[27] Kyle DeMars, Carolin Frueh, Moriba Jah, and Richard Erwin. An aegis-fisst algorithm for multiple object tracking in space situational awareness. 08 2012.

[28] Kyle Jordan DeMars. Nonlinear Orbit Uncertainty Prediction and Rectification for Space Situational Awareness. PhD thesis, The University of Texas at Austin, 12 2010.

[29] André Deprit. Canonical transformations depending on a small parameter. Celestial Mechanics, 1(1):12–30, March 1969.

[30] Tarek Elgohary and James Turner. State transition tensor models for the uncertainty propagation of the two-body problem. volume 150, 08 2013.

[31] P Exertier, G Métris, Y Boudon, and F Barlier. Long term evolution of mean orbital elements of artificial satellites. Gravimetry and Space Techniques Applied to Geodynamics and Ocean Dynamics, 82:103–108, 1994.

[32] James Lee Foster. A parametric analysis of orbital debris collision probability and maneuver rate for space vehicles. NASA JSC-25898, 1992.

[33] Carolin Frueh, Kathleen Howell, Kyle J. DeMars, and Surabhi Bhadauria. CISLUNAR SPACE SITUATIONAL AWARENESS. In 31st AAS/AIAA Space Flight Mechanics Meeting, Virtual. AAS 21-290, 2021.

[34] K. Fujimoto and D. J. Scheeres. Tractable Expressions for Nonlinearly Propagated Uncertainties. Journal of Guidance, Control, and Dynamics, 38(6):1146–1151, 2015.

[35] K. Fujimoto, D. J. Scheeres, and K. T. Alfriend. Analytical nonlinear propagation of uncertainty in the two-body problem. Journal of Guidance, Control, and Dynamics, 35(2):497–509, 2012.

[36] Kohei Fujimoto. New Methods in Optical Track Association and Uncertainty Mapping of Earth-Orbiting Objects. PhD thesis, University of Colorado Boulder, 2013.

[37] D.T. Greenwood. Principles of Dynamics. Prentice-Hall international series in dynamics. Prentice-Hall, 1988.

[38] Liam M Healy. Orbit propagation with lie transfer maps in the perturbed kepler problem. Celestial Mechanics and Dynamical Astronomy, 85:175–207, 2003.

[39] Joshua T. Horwood, Nathan D. Aragon, and Aubrey B. Poore. Gaussian Sum Filters for Space Surveillance: Theory and Simulations. Journal of Guidance, Control, and Dynamics, 34(6):1839–1851, 2011.

[40] Marco F. Huber, Tim Bailey, Hugh Durrant-Whyte, and Uwe D. Hanebeck. On entropy approximation for gaussian mixture random vectors. In 2008 IEEE International Conference on Multisensor Fusion and Integration for Intelligent Systems, pages 181–188, 2008.

[41] Erica Jenson and Daniel J. Scheeres. Semianalytical measures of nonlinearity based on tensor eigenpairs. In AAS/AIAA Astrodynamics Specialist Conference, 08 2021.

[42] B. A. Jones and Alireza Doostan. Satellite collision probability estimation using polynomial chaos expansions. Advances in Space Research, 52(11):1860–1875, 2013.

[43] Brandon A Jones, Alireza Doostan, and George H Born. Nonlinear propagation of orbit uncertainty using non-intrusive polynomial chaos. Journal of Guidance, Control, and Dynamics, 36(2):430–444, 2013.

[44] John Junkins and Puneet Singla. How nonlinear is it? a tutorial on nonlinearity of orbit and attitude dynamics. Advances in the Astronautical Sciences, 115:1–45, 01 2003.

[45] Ahmed Aly Kamel. Expansion Formulae in Canonical Transformations Depending on a Small Parameter. Celestial Mechanics, 1(2):190–199, June 1969.

[46] Ahmed Aly Kamel. Perturbation Method in the Theory of Nonlinear Oscillations. Celestial Mechanics, 3:90, March 1970.

[47] Yashica Khatri. Long-term-saupca-toolkit. Available at `https://github.com/yashicakhatri2/Long-Term-SAUPCA-Toolkit.git`.

[48] Yashica Khatri. Short-term-saupca-toolkit. Available at `https://github.com/yashicakhatri2/Short-Term-SAUPCA-Toolkit.git`.

[49] Yashica Khatri and Daniel J Scheeres. Nonlinear semi-analytical uncertainty propagation for conjunction analysis. In Proceedings of 72nd International Astronautical Congress 2021 IAC-21,C1,3,12,x64896, Dubai, United Arab Emirates, 09 2021.

[50] Yashica Khatri and Daniel J Scheeres. Hybrid nonlinear semi-analytical uncertainty propagation for conjunction analysis. In Proceedings of 73rd International Astronautical Congress 2022 IAC-22,C1,3,1,x68776, Paris, France, 2022.

[51] Yashica Khatri and Daniel J Scheeres. HYBRID METHOD OF UNCERTAINTY PROPAGATION FOR LONG-TERM CONJUNCTION ANALYSIS. In 33rd AAS/AIAA Space Flight Mechanics Meeting, Austin, Texas. AAS 23-376, 2023.

[52] Yashica Khatri and Daniel J Scheeres. Nonlinear Semi-Analytical Uncertainty Propagation for Conjunction Analysis. Acta Astronautica, 203:568–576, 2023.

[53] Hiroshi Kinoshita. Third-Order Solution of an Artificial-Satellite Theory. SAO Special Report, 379, July 1977.

[54] P.S. Laplace. Théorie analytique des probabilités, 1812.

[55] Martín Lara. Hamiltonian Perturbation Solutions for Spacecraft Orbit Prediction: The Method of Lie Transforms. De Gruyter, 2021.

[56] V.I. Lebedev and D. N. Laikov. Quadrature Formula for the Sphere of the 131st Algebraic Order of Accuracy. Doklady Mathematics, 59(3):477–481, 1999.

[57] Francesca Letizia, Camilla Colombo, and Hugh Lewis. Collision probability due to space debris clouds through a continuum approach. Journal of Guidance, Control, and Dynamics, 09 2015.

[58] Jiasheng Li, Zhen Yang, and Ya-Zhong Luo. A review of space-object collision probability computation methods. Astrodynamics, 04 2022.

[59] J.-C Liou, Anilkumar A K, Benjamin Virgili, Toshiya Hanada, Holger Krag, Hugh Lewis, M. Raj, M Rao, A Rossi, and Ram Sharma. Stability of the future leo environment – an iadc comparison study. 04 2013.

[60] RH Lyddane. Small eccentricities or inclinations in the brouwer theory of the artificial satellite. Astronomical Journal, Vol. 68, p. 555 (1963), 68:555, 1963.

[61] VLADIMIR MAZ'YA and GUNTHER SCHMIDT. On approximate approximations using Gaussian kernels. IMA Journal of Numerical Analysis, 16(1):13–29, 01 1996.

[62] G Métris and Pierre Exertier. Semi-analytical theory of the mean orbital motion. Astronomy and Astrophysics, Vol. 294, p. 278-286 (1995), 294:278–286, 1995.

[63] P. Misra and P. Enge. Global Positioning System: Signals, Measurements, and Performance. Ganga-Jamuna Press, 2011.

[64] Inkwan Park. Dynamical Realism and Uncertainty Propagation. PhD thesis, University of Colorado Boulder, 2015.

[65] Inkwan Park and D. J. Scheeres. Hybrid Method for Uncertainty Propagation of Orbital Motion. Journal of Guidance, Control, and Dynamics, 41(1):240–254, 2018.

[66] Ryan Park and D. J. Scheeres. Nonlinear Mapping of Gaussian Statistics: Theory and Applications to Spacecraft Trajectory Design. Journal of Guidance, Control, and Dynamics, 29(6):1367–1375, 2006.

[67] Ryan S. Park and Daniel J. Scheeres. Nonlinear Mapping of Gaussian Statistics: Theory and Applications to Spacecraft Trajectory Design. Journal of Guidance, Control, and Dynamics, 29(6), 2006.

[68] W H Press, S A Teukolsky, W T Vetterling, and B P Flannery. Numerical Recipes: The Art of Scientific Computing, pages 156–162. International series of monographs on physics. Cambridge University Press, 3 edition, 2007.

[69] William J. Riley. Handbook of Frequency Stability Analysis. U.S. Dept. of Commerce, National Institute of Standards and Technology, 2008.

[70] B. Schutz, B. Tapley, and G.H. Born. Statistical Orbit Determination. Elsevier Science, 2004.

[71] Harold W Sorenson and Daniel L Alspach. Recursive bayesian estimation using gaussian sums. Automatica, 7(4):465–479, 1971.

[72] Eileen K. Stansbery. Orbital debris program office. `https://orbitaldebris.jsc.nasa.gov`, 2021.

[73] Yifei Sun and Mrinal Kumar. Uncertainty propagation in orbital mechanics via tensor decomposition. Celestial Mechanics and Dynamical Astronomy, 124(3):269–294, March 2016.

[74] Gabriel Terejanu, Puneet Singla, Tarunraj Singh, and Peter Scott. Uncertainty propagation for nonlinear dynamic systems using gaussian mixture models. AIAA Journal of Guidance, Control and Dynamics, 31:1623–1633, 08 2008.

[75] Chelsea Thangavelu. Transfers Between Near Rectilinear Halo Orbits and Low Lunar Orbits. PhD thesis, University of Colorado Boulder, 2018.

[76] Catherine L. Thornton and James S. Border. Range and Doppler Tracking Observables, page 9–12. Jet Propulsion Laboratory, California Institute of Technology, 2000.

[77] David A. Vallado. Fundamentals of Astrodynamics and Applications. Microcosm Press, 4 edition, 2013.

[78] Kumar Vishwajeet, Puneet Singla, and Moriba Jah. Nonlinear uncertainty propagation for perturbed two-body orbits. Journal of Guidance, Control, and Dynamics, 37:1415–1425, 09 2014.

[79] Vivek Vittaldev and Ryan Russell. Multidirectional gaussian mixture models for nonlinear uncertainty propagation. Computer Modeling in Engineering & Sciences, 111(1):83–117, 2016.

[80] Vivek Vittaldev and Ryan Russell. Space object collision probability using multidirectional gaussian mixture models. Journal of Guidance, Control, and Dynamics, 39:1–7, 07 2016.

[81] Vivek Vittaldev, Ryan Russell, and Richard Linares. Spacecraft uncertainty propagation using gaussian mixture models and polynomial chaos expansions. Journal of Guidance, Control, and Dynamics, 39, 09 2016.

Appendix A

Transformations of State and Uncertainty Coordinates

This Appendix details some of the conversions between the Cartesian, equinoctial, and Delaunay coordinates for the state and uncertainty of an object. These transformations are essential for the full implementation of this method since the initial distribution is in the Cartesian coordinates and the near-Earth GMM split is applied in the Equinoctial coordinates, whereas, the Simplified Dynamical System is defined in the Delaunay coordinates.

Some conversions are achieved using Jacobians (J) that include the partials of the state representation in one coordinate frame vs the second, whereas, others are defined using a sequence of rotations about chosen axes. Generally, simple transformations are defined and modified as needed for the application. For instance, the conversion between IJK and PQW [77] frames is defined, along with a Jacobian for PQW relative to classical orbital elements (COE) [11], and combined to achieve a transformation between the original Cartesian state and covariance to COE.

A state conversion is a simple multiplication of the transformation matrix and the state vector. Whereas, the covariance transformation is achieved by multiplying the conversion matrix before and after, as shown below:

$$Q_{COE} = J_{PQWtoCOE} * J_{IJKtoPQW} * Q_{IJK} * J_{IJKtoPQW} * J_{PQWtoCOE} \tag{A.1}$$

The conversion between IJK and PQW frames can be defined as follow using the classical orbital elements (a,e,i,Ω,ω,M):

$$J_{IJKtoPQW} = [\mathrm{ROT}_3(-\Omega)][\mathrm{ROT}_1(-i)][\mathrm{ROT}_3(-\omega)] \tag{A.2}$$

where ROT stands for 3×3 rotation matrix, the subscript for the rotation matrix is the axis about which to rotate: $\hat{x}$, $\hat{y}$, and $\hat{z}$, and the angle of rotation is listed in the parenthesis.

The Jacobian between the PQW frame and COE is defined by Broucke [11]:

Partials	$/\partial a$	$/\partial e$	$/\partial M$
∂X /	$\frac{1}{a}(X - \frac{3t}{2}\dot{X})$	L	$\frac{\dot{X}}{n}$
∂Y /	$\frac{1}{a}(Y - \frac{3t}{2}\dot{Y})$	M	$\frac{\dot{Y}}{n}$
$\partial \dot{X}$ /	$-\frac{1}{2a}(\dot{X} - 3\mu\frac{Xt}{r^3})$	$\dot{L}$	$-n(\frac{a}{r})^3 X$
$\partial \dot{Y}$ /	$-\frac{1}{2a}(\dot{Y} - 3\mu\frac{Yt}{r^3})$	$\dot{M}$	$-n(\frac{a}{r})^3 Y$

Table A.1: Caption

$$L = \frac{a^2}{r}(e\cos E - 1 - \sin^2 E) \tag{A.3a}$$

$$M = \frac{a^2 \sin E}{r\sqrt{1-e^2}}(\cos E - e) \tag{A.3b}$$

$$\dot{L} = \frac{na^4}{r^3}(e - 2\cos E + e\cos^2 E)\sin E \tag{A.3c}$$

$$\dot{M} = \frac{na^4}{r^3\sqrt{1-e^2}}(e^2 - 1 - e\cos E + 2\cos^2 E - e\cos^3 E) \tag{A.3d}$$

$$\tag{A.3e}$$

Similarly, the inverse partials are also defined by Broucke [11].

The Jacobian between the PQW frame and equinoctial elements was defined by Broucke [12] using a group of intermediate variables.

The conversion to Delaunay element sets is achieved by taking partials between Equinoctial and Delaunay sets using the MATLAB symbolic computer:

$$\frac{\partial \text{COE}}{\partial \text{Delaunay}} = \begin{bmatrix} 0 & 0 & 0 & 5.017556E-06*L & 0 & 0 \\ 0 & 0 & 0 & G^2/(L^3*(1-G^2/L^2)^(1/2)) & -G/(L^2*(1-G^2/L^2)^(1/2)) & 0 \\ 0 & 0 & 0 & 0 & H/(G^2*(1-H^2/G^2)^(1/2)) & -1/(G*(1-H^2/G^2)^(1/2)) \\ 0 & 0 & 1 & 0 & 0 & 0 \\ 0 & 1 & 0 & 0 & 0 & 0 \\ 1 & 0 & 0 & 0 & 0 & 0 \end{bmatrix} \tag{A.4}$$

and using the chain rule:

$$\frac{\partial \text{Equinoctial}}{\partial \text{Delaunay}} = \frac{\partial \text{Equinoctial}}{\partial \text{COE}} * \frac{\partial \text{COE}}{\partial \text{Delaunay}} \tag{A.5}$$

Similarly, $\frac{\partial \text{Delaunay}}{\partial \text{COE}}$ can be calculated using the symbolic computer and using chain rule:

$$\frac{\partial \text{Delaunay}}{\partial \text{Equinoctial}} = \frac{\partial \text{Delaunay}}{\partial \text{COE}} * \frac{\partial \text{COE}}{\partial \text{Equinoctial}} \tag{A.6}$$

Appendix B

Simplified Dynamical System: Mean Dynamics Equations

This chapter lists the dynamical equations of motion calculated for the mean dynamics from the Simplified Dynamical System (SDS) defined in chapter 2. These are computed using the MATLAB symbolic computer using Eq. (2.27).

$$\dot{l} = \mu^2/L^3 - (3*L*\beta*(1-G^2/L^2)^{(1/2)}*((cos(g+h-h_\odot-k_\odot)*(H/G+1)*(c_\odot+1))/4-$$
$$(cos(g-h+h_\odot+k_\odot)*(H/G-1)*(c_\odot+1))/4-(cos(g+h-h_\odot+k_\odot)*(H/G+1)*(c_\odot-1))$$
$$/4+(cos(g-h+h_\odot-k_\odot)*(H/G-1)*(c_\odot-1))/4+s_\odot*sin(g)*sin(k_\odot)*(1-H^2/G^2)^{1/2}))/\mu$$
$$+(3*J2*R_E^2*\mu^4*((3*H^2)/G^2-1))/(4*G^3*L^4)-(3*G^2*\beta*((cos(g+h-h_\odot$$
$$-k_\odot)*(H/G+1)*(c_\odot+1))/4-(cos(g-h+h_\odot+k_\odot)*(H/G-1)*(c_\odot+1))/4-(cos(g+h$$
$$-h_\odot+k_\odot)*(H/G+1)*(c_\odot-1))/4+(cos(g-h+h_\odot-k_\odot)*(H/G-1)*(c_\odot-1))/4+$$
$$s_\odot*sin(g)*sin(k_\odot)*(1-H^2/G^2)^{(1/2)}))/(2*L*\mu*(1-G^2/L^2)^{(1/2)})+$$
$$(J2^2*R_E^4*\mu^6*((G^2/L^2-1)*(4*((3*H^2)/G^2-1)^2+(3*G^2*(5*(H^2/G^2-1)^2-$$
$$(8*H^2)/G^2))/L^2)+4*((3*H^2)/G^2-1)^2+(12*G^3*((3*H^2)/G^2-1)^2)/L^3+(4*G^2*$$
$$(21*(H^2/G^2-1)^2+(42*H^2)/G^2-22))/L^2-(G^2*cos(2*g)*(H^2/G^2-1)*((15*H^2)$$
$$/G^2-1)*((6*G^2)/L^2-6))/L^2))/(128*G^9*L^2)+(J2^2*R_E^4*\mu^6*((36*G^3*((3*H^2)$$
$$/G^2-1)^2)/L^4+(2*G^2*(4*((3*H^2)/G^2-1)^2+(3*G^2*(5*(H^2/G^2-1)^2-(8*H^2)$$
$$/G^2))/L^2))/L^3+(8*G^2*(21*(H^2/G^2-1)^2+(42*H^2)/G^2-22))/L^3+(6*G^2*$$
$$(G^2/L^2-1)*(5*(H^2/G^2-1)^2-(8*H^2)/G^2))/L^3-(12*G^4*cos(2*g)*(H^2/G^2-1)*$$
$$((15*H^2)/G^2-1))/L^5-(2*G^2*cos(2*g)*(H^2/G^2-1)*((15*H^2)/G^2-1)*((6*G^2)/L^2$$
$$-6))/L^3))/(128*G^9*L) \qquad \text{(B.1)}$$

$$\dot{g} = (3 * G * \beta * ((cos(g + h - h_{\odot} - k_{\odot}) * (H/G + 1) * (c_{\odot} + 1))/4 - (cos(g - h + h_{\odot} + k_{\odot}) * (H/G - 1) *$$
$$(c_{\odot} + 1))/4 - (cos(g + h - h_{\odot} + k_{\odot}) * (H/G + 1) * (c_{\odot} - 1))/4 + (cos(g - h + h_{\odot} - k_{\odot}) * (H/G$$
$$- 1) * (c_{\odot} - 1))/4 + s_{\odot} * sin(g) * sin(k_{\odot}) * (1 - H^2/G^2)^{(1/2)}))/(2 * \mu * (1 - G^2/L^2)^{(1/2)})$$
$$- (3 * L^2 * \beta * (1 - G^2/L^2)^{(1/2)} * ((H * cos(g + h - h_{\odot} + k_{\odot}) * (c_{\odot} - 1))/(4 * G^2) - (H * cos(g -$$
$$h + h_{\odot} - k_{\odot}) * (c_{\odot} - 1))/(4 * G^2) - (H * cos(g + h - h_{\odot} - k_{\odot}) * (c_{\odot} + 1))/(4 * G^2) + (H * cos(g -$$
$$h + h_{\odot} + k_{\odot}) * (c_{\odot} + 1))/(4 * G^2) + (H^2 * s_{\odot} * sin(g) * sin(k_{\odot}))/(G^3 * (1 - H^2/G^2)^{(1/2)})))/$$
$$(2 * \mu) + (3 * H^2 * J2 * RE^2 * \mu^4)/(2 * G^6 * L^3) - (J2^2 * RE^4 * \mu^6 * ((G^2/L^2 - 1) * ((6 * G * (5 *$$
$$(H^2/G^2 - 1)^2 - (8 * H^2)/G^2))/L^2 + (3 * G^2 * ((16 * H^2)/G^3 - (20 * H^2 * (H^2/G^2 - 1))$$
$$/G^3))/L^2 - (48 * H^2 * ((3 * H^2)/G^2 - 1))/G^3) + (2 * G * (4 * ((3 * H^2)/G^2 - 1)^2 + (3 * G^2 * (5 *$$
$$(H^2/G^2 - 1)^2 - (8 * H^2)/G^2))/L^2))/L^2 + (36 * G^2 * ((3 * H^2)/G^2 - 1)^2)/L^3 + (8 * G *$$
$$(21 * (H^2/G^2 - 1)^2 + (42 * H^2)/G^2 - 22))/L^2 - (4 * G^2 * ((84 * H^2)/G^3 + (84 * H^2 * (H^2/G^2$$
$$- 1))/G^3))/L^2 - (48 * H^2 * ((3 * H^2)/G^2 - 1))/G^3 - (144 * H^2 * ((3 * H^2)/G^2 - 1))/L^3 -$$
$$(12 * G^3 * cos(2 * g) * (H^2/G^2 - 1) * ((15 * H^2)/G^2 - 1))/L^4 + (30 * H^2 * cos(2 * g) * (H^2/G^2 - 1)$$
$$* ((6 * G^2)/L^2 - 6))/(G * L^2) + (2 * H^2 * cos(2 * g) * ((15 * H^2)/G^2 - 1) * ((6 * G^2)/L^2 - 6))/$$
$$(G * L^2) - (2 * G * cos(2 * g) * (H^2/G^2 - 1) * ((15 * H^2)/G^2 - 1) * ((6 * G^2)/L^2 - 6))/L^2))/$$
$$(128 * G^9 * L) + (3 * J2 * RE^2 * \mu^4 * ((3 * H^2)/G^2 - 1))/(4 * G^4 * L^3) + (9 * J2^2 * RE^4 * \mu^6 *$$
$$((G^2/L^2 - 1) * (4 * ((3 * H^2)/G^2 - 1)^2 + (3 * G^2 * (5 * (H^2/G^2 - 1)^2 - (8 * H^2)/G^2))/L^2)$$
$$+ 4 * ((3 * H^2)/G^2 - 1)^2 + (12 * G^3 * ((3 * H^2)/G^2 - 1)^2)/L^3 + (4 * G^2 * (21 * (H^2/G^2 - 1)^2$$
$$+ (42 * H^2)/G^2 - 22))/L^2 - (G^2 * cos(2 * g) * (H^2/G^2 - 1) * ((15 * H^2)/G^2 - 1) * ((6 * G^2)/L^2$$
$$- 6))/L^2))/(128 * G^{10} * L) \tag{B.2}$$

$$\dot{h} = (3 * L^2 * \beta * (1 - G^2/L^2)^{(1/2)} * ((cos(g + h - h_\odot + k_\odot) * (c_\odot - 1))/(4 * G) + (cos(g - h + h_\odot + k_\odot) * (c_\odot + 1))/(4 * G) - (cos(g + h - h_\odot - k_\odot) * (c_\odot + 1))/(4 * G) - (cos(g - h + h_\odot - k_\odot) * (c_\odot - 1))/(4 * G) + (H * s_\odot * sin(g) * sin(k_\odot))/(G^2 * (1 - H^2/G^2)^{(1/2)})))/(2 * \mu) - (J2^2 * RE^4 * \mu^6 * ((G^2/L^2 - 1) * ((48 * H * ((3 * H^2)/G^2 - 1))/G^2 - (3 * G^2 * ((16 * H)/G^2 - (20 * H * (H^2/G^2 - 1))/G^2))/L^2) + (48 * H * ((3 * H^2)/G^2 - 1))/G^2 + (4 * G^2 * ((84 * H)/G^2 + (84 * H * (H^2/G^2 - 1))/G^2))/L^2 + (144 * G * H * ((3 * H^2)/G^2 - 1))/L^3 - (30 * H * cos(2 * g) * (H^2/G^2 - 1) * ((6 * G^2)/L^2 - 6))/L^2 - (2 * H * cos(2 * g) * ((15 * H^2)/G^2 - 1) * ((6 * G^2)/L^2 - 6))/L^2))/(128 * G^9 * L) - (3 * H * J2 * RE^2 * \mu^4)/(2 * G^5 * L^3) \tag{B.3}$$

$$\dot{L} = 0 \tag{B.4}$$

$$\dot{G} = (3 * L^2 * \beta * (1 - G^2/L^2)^{(1/2)} * ((sin(g + h - h_\odot + k_\odot) * (H/G + 1) * (c_\odot - 1))/4 - (sin(g - h + h_\odot - k_\odot) * (H/G - 1) * (c_\odot - 1))/4 - (sin(g + h - h_\odot - k_\odot) * (H/G + 1) * (c_\odot + 1))/4 + (sin(g - h + h_\odot + k_\odot) * (H/G - 1) * (c_\odot + 1))/4 + s_\odot * cos(g) * sin(k_\odot) * (1 - H^2/G^2)^{(1/2)}))/(2 * \mu) + (J2^2 * RE^4 * \mu^6 * sin(2 * g) * (H^2/G^2 - 1) * ((15 * H^2)/G^2 - 1) * ((6 * G^2)/L^2 - 6))/(64 * G^7 * L^3) \tag{B.5}$$

$$\dot{H} = -(3 * L^2 * \beta * (1 - G^2/L^2)^{(1/2)} * ((sin(g + h - h_\odot - k_\odot) * (H/G + 1) * (c_\odot + 1))/4 - (sin(g - h + h_\odot - k_\odot) * (H/G - 1) * (c_\odot - 1))/4 - (sin(g + h - h_\odot + k_\odot) * (H/G + 1) * (c_\odot - 1))/4 + (sin(g - h + h_\odot + k_\odot) * (H/G - 1) * (c_\odot + 1))/4))/(2 * \mu) \tag{B.6}$$

$$\dot{k}_\odot = \nu \tag{B.7}$$

$$\dot{K}_{\odot} = (3 * L^2 * \beta * (1 - G^2/L^2)^{(1/2)} * ((sin(g + h - h_{\odot} - k_{\odot}) * (H/G + 1) * (c_{\odot} + 1))/4 + (sin(g - h + h_{\odot} - k_{\odot}) * (H/G - 1) * (c_{\odot} - 1))/4 + (sin(g + h - h_{\odot} + k_{\odot}) * (H/G + 1) * (c_{\odot} - 1))/4 + (sin(g - h + h_{\odot} + k_{\odot}) * (H/G - 1) * (c_{\odot} + 1))/4 + s_{\odot} * cos(k_{\odot}) * sin(g) * (1 - H^2/G^2)^{(1/2)}))/(2 * \mu) \tag{B.8}$$